SCUOLA DI DOTTORATO
UNIVERSITÀ DEGLI STUDI DI MILANO-BICOCCA

Department of Envirionmental and Earth Sciences

Ph.D. program: **Chemical, Geological and Environmental Sciences** Cycle: **XXXII**

Curriculum in: **Environmental Sciences**

INVESTIGATION OF TERRAIN CONTROL ON DRYLAND STRUCTURE AND COMPOSITION USING MULTIPLE REMOTE SENSING SENSORS AND PLATFORMS

Surname: **Blanco Sacristán**

Name: **Javier**

Registration number: **824406**

Tutor: **Dr. Micol Rossini**

Co-tutor: **Dr. Cinzia Panigada**

Coordinator: **Prof. Maria Luce Frezzotti**

ACADEMIC YEAR: 2018/2019

Contents

List of figures

List of tables

Acronyms

AMD	Average minimum distance
ARD	Average random distance
ATI	Apparent thermal inertia
AUC	Area under the curve
CR	Continuum removal
CV	Coefficient of variation
DEM	Digital elevation model
DSM	Digital surface model
DTM	Digital terrain model
ED2	Euclidian distance v.2
KIA	Kappa index of accuracy
LiDAR	Light detection and ranging
MBE	Mean bias error
NIR	Near-infrared
NSR	Number-of-segments ratio
OA	Overall accuracy
OBIA	Object-based image analysis
PET	Potential evapotranspiration
PSE	Potential segmentation error
REDIAM	Andalusian Environmental Information Network
RMSE	Root-mean-square error
ROC	Receiver operating characteristics
SEaTH	Separability and threshold
SfM	Structure-from-motion
SVH	Spectral variation hypothesis
SVM	Support vector machine
UAV	Unmanned aerial vehicle
TIR	Thermal infrared
VIS	Visible
WFD	Water framework directive

Abstract

Drylands are among the most sensitive areas to current climate change and their cover is expected to increase in the next decades. Terrain has a key role in the distribution of water and nutrients in drylands and in shaping their composition. These environments are generally composed by a two-phases mosaic of vegetation and bare soil, many times colonized by biocrusts (i.e. topsoil communities formed by mosses, lichens, liverworts, algae, and cyanobacteria), which are expected to suffer compositional changes that will reduce their richness and functioning. In this context, remote sensing has been highlighted several times as an important tool for dryland monitoring. It is one of the most cost-effective approaches to identify biodiversity hotspots and to monitor changes in their composition, and to evaluate the relationships these changes have with the surrounding terrain.

Two main image analyses can be used for monitoring of dryland environments. While object-based image analysis (OBIA) works well in landscapes with heterogeneous compositions (e.g. scattered communities of vegetation in drylands), pixel-based image analysis excels in environments where the differentiation between components is not that obvious (e.g. drylands where developed communities of biocrust appear in plant interspaces). However, until recently, most of the methodologies to map well differentiated two-phased drylands have not been so successful when all these components appear together and mixed. Nevertheless, the raise of new hardware and software platforms promise to solve this, while improving our knowledge of drylands. The miniaturization of sensors, the ease of use of Unmanned Aerial Vehicles (UAVs) and the new methodologies developed in the last years (e.g., Structure-from-Motion (SfM), which allows to reconstruct the terrain by using digital photogrammetry) permit to study relationships in the ecosystems that not so long ago were only possible to be studied by expensive field work campaigns. Furthermore developments in hyper- and multispectral imaging sensors have increased the potentially retrieved spectral information, which has been proved to contain functional and phylogenetic components of biodiversity. In addition, thermal infrared imagery (TIR) has been successfully used to estimate soil moisture content in drylands with homogeneous surfaces. However, most studies using these tools have been focused on superior plants in environments different to drylands or in drylands where biocrusts do not appear. For this reason, applying these techniques in drylands and not only in vegetation but also in biocrusts is key to understanding their applicability in these environments. This would greatly improve existing dryland restoration and monitoring programs.

The main aim of this dissertation was to study how dryland composition and functioning are affected by the terrain using remote sensing at close range and mid range in combination with complementary methods. For this purpose, data from very high spatial resolution RGB, thermal infrared (TIR), multi- and hyperspectral imagery, retrieved in the laboratory and in the field using airborne, UAV and stationary platforms were used, and the following specific objectives were addressed: i) evaluating whether SfM techniques can be used in drylands with complex and heterogeneous surfaces to derive their terrain from UAV imagery; ii) developing a reproducible technique to relate human actions to changes in the health of dryland scarce vegetation communities by using object-based image analysis; iii) testing whether the spectral heterogeneity of lichens can be used to estimate their α-diversity

using hyperspectral imagery; iv) developing a methodology to evaluate the control that terrain has on dryland biocrusts' distribution using information solely retrieved from UAV; v) testing if TIR imagery can be used to estimate soil moisture content in drylands.

Results provided evidence of the effectiveness of multi-source remotely sensed data to map dryland constituents. However, these results also pointed out the complexity of the link between dryland diversity and its terrain and the growing need to integrate different remotely sensed products to obtain an unambiguous interpretation of remote sensing data in drylands. In particular, results showed that:

i) SfM-based workflows should apply product validation by check points and considerations regarding camera calibration should be carefully accounted for in drylands, where vegetation and bare soils appear mixed and their identification is hampered by similar optical properties;

ii) OBIA is a successful methodology to monitor scattered vegetation patches in drylands and its use allows to relate human activities to health changes of this vegetation;

iii) spectral diversity can be used to retrieve α-diversity of biocrust-forming lichens in the laboratory, under controlled conditions and using hyperspectral imagery;

iv) biocrusts respond differently to specific microhabitats created by terrain attributes depending on their composition, and typical biocrust development models should be revisited since they can not be generalized to all drylands;

v) TIR can successfully be used to estimate soil moisture content in dryland heterogeneous surfaces, even when covered by biocrusts.

The innovation of this study comprises an evaluation of the SfM techniques at different scales and its applicability to study the effect of the terrain on water redistribution in drylands. It also comprises a novel methodology to monitor scattered vegetation in a ground-water dependent ecosystem, where the health of these individuals is key for a correct maintenance of the ecosystem's functioning. Moreover, the application of close-range hyperspectral imagery allowed to estimate the α-diversity of biocrust-forming lichens using their spectral diversity. This led to a better understanding of the spectral behaviour of biocrusts depending on their composition and allowed to develop a methodology to produce accurate maps of land cover in a dryland ecosystem of heterogeneous composition.

Throughout this dissertation, remote sensing demonstrates to be an effective tool to monitor dryland biodiversity and to better understand its functioning. Further research in this direction constitutes a high priority for improving understanding of the functioning of dryland components and their response to global change.

Acknowledgements

For I reckon that the sufferings of this present
time are not worthy to be compared
with the glory which shall be revealed in us.
- Romans 8:18 -

And here we are. After three and a half years, here we are. Time to reflect on who to be grateful to. Seems easy. It is not.

First of all, Cinzia and Micol. Without your initial thrust I would not be here, so thank you. Thank you for keeping my feet on the ground, even when I was losing my head. Thank you for this and for all the time you have invested on this thesis and on me. Thank you for teaching me how to keep attention to the details, which are all. Thank you for teaching me how to be patient, even when I did not want to hear about it. Thank you.

Thank you to all the members of the LTDA: Roberto Colombo, Sergio Cogliati, Marco Celesti, Biagio di Mauro, Roberto Garzonio, Francesca Bearzot and Ilaria Cesana. Thank you. I could spend pages and pages writing how you made my days working in the office incredible, even when I was feeling low. Thank you for always having a smile in your faces and always having time for a little break away from work. Thank you.

Rodolfo Gentili is almost another member of the LTDA, but he deserves a paragraph on his own. Thank you, Rudy, for all the time discussing about biocrusts. Thank you for your patience, even when discussions seemed to have no end. Thank you.

Thank you to all the members of the TRUSTEE (do we already know how to write this?) network: David Martini, Daniel Pabón, Vicente Burchard, Juan Quirós, Egor (Egór!) Prikaziuk, Hafiz Ali Imran, Georgios Ntakos, María Culam. You all have been part of a very important part of my life and I will always be grateful for the time we have spent together. In front of the computers and, more importantly, out of the office. Thank you.

Thank you to Karen Anderson for always having the door of your office open for me. You are what any scientist should aspire to be. Thank you.

Thank you to Ian Ashton for being so supportive and understanding. I owe you a big one. Thank you.

Thank you to all the members of the Spanish *mafia* in Cornwall. David, Eva, Cristina, Jessica, Giovanni, I owe you a lot. Thank you.

A special place in my heart and memories will always be for the formidable Giulia Tagliabue, Khelvi Biryukova, Anthon Evdokimov and Dominic Fawcett. You have been family for me during these three last years and family is what life is all about. Thank you for being close to me at any time. Thank you for always having time to talk about nothing and all at the same time. Thank you, thank you, thank you. You have no idea how important you have been and are for me. Thank you.

I obviously must mention Emilio Guirado. You have been at the other side of the screen at any time and always that I have been able to visit Spain. You have taught me a lot in our never-ending conversations about science, remote sensing, biology and, more importantly, life. I hope we always keep our friendship strong as it is now. Thank you.

My parents, Carmen Sacristán and Gonzalo Blanco have been key pieces of this thesis. Since the moment I was born they have invested all they have in me and my education. This thesis is both equal mine and theirs. Thank you for everything you have done and still do for me. Thank you.

And, well, I am obviously grateful to my wife, the most encouraging person I have ever met. Thank you, Paqui. Thank you for being there, even when I was about to ring the bell. Thank you for trusting me and always telling me "you can do this", even when I did not believe that myself. Thank you for building up a life in the distance. Thank you for being the family I have always wanted. Gracias, mi amor. Gracias.

Lastly, I am grateful to Andrés Reyes who, for the wrong reasons, has been present every day during these last years. Thank you for being the sunshine you were and the smile you gifted to anyone willing to spend some time with you. Thank you for all you taught us, maybe even not being conscious of your lessons. Thank you. We will always miss you. *¡Nos vemos, saecio!*

Javier Blanco Sacristán
11/09/2020
Falmouth, United Kingdom

Introduction

1.1. Drylands and their importance worldwide

Drylands include arid, semi-arid and dry subhumid regions and are by definition areas where precipitation is scarce and typically unpredictable, with high rates of evapotranspiration (Middleton and Thomas, 1997). These environments constitute the largest biome on Earth, cover more than 47% of land surface (Koutroulis, 2018) and host over 40% of the global human population (Reynolds et al, 2007). However, drylands are among the most sensitive areas to current climate change and some form of land degradation takes place in 10-20% of these lands (Reynolds et al., 2007). Furthermore, due to reduced carbon sequestration and enhanced regional warming, drylands are expected to increase their extension over 23% by the end of the century under the worst global change models (Huang et al., 2015). These changes are estimated to affect in the next decades more than 250 million people, and climate projections expect that warmer and drier conditions will increase in drylands worldwide (Cayan et al., 2010; Cook et al., 2015), resulting in further degradation of these environments (Huang et al., 2017, 2016). This will not only have strong implications in the economies of drylands (Adhikari and Nadella, 2011), but will also affect dryland biodiversity (e.g., Ladrón de Guevara, 2018; Berdugo et al., 2020). For this reason, understanding the components that affect the most dryland composition is key for a right understanding of these environments' functioning.

1.2. Importance of terrain attributes in drylands' composition

Climate patterns control drylands' composition worldwide (Bowker et al., 2016; Berdugo et al., 2020), but soil and terrain attributes can generate deviations from these patterns at ecosystem scale (e.g., Williams et al., 2013; Bowker et al., 2016; Durham et al., 2018; Rodríguez-Caballero et al., 2019). This can create specific microclimatic conditions, different from the ones observed at wider scales, and offer refugia for species (Suggit et al., 2018). Terrain attributes in drylands condition redistribution of rainfall water (Puigdefábregas et al., 1999) by modifying moisture (Epstein et al., 2006) and characteristics of bare soil surfaces (Eldridge et al., 2000; Maestre et al., 2002). However, rainfall precipitations in drylands are scarce, and spatial heterogeneities of soil nutrients and organic matter are ultimately affected by the terrain, which modifies soil water content and fluxes of nutrients (Puigdefábregas and Sánchez, 1996; Manzoni et al., 2006). Thus, availability of nutrients and resources in drylands is driven by water availability, subsurface flows, runoff and infiltration (e.g., Aguiar and Sala 1999; Puigdefábregas et al. 1999; Puigdefábregas, 2005). All this affects not only vegetation distribution but also other components that might appear in plant interspaces in drylands (Rodríguez-Caballero et al., 2019). Therefore, developing reproducible methods that allow to understand the effect that terrain has on dryland constituents is key to improving actual and current conservation programs in these environments.

1.3. Biocrusts and their importance in drylands

Most drylands worldwide present a two-phase mosaic structure composed by vegetation patches with different sizes and shapes among ecosystems (Aguiar and Sala, 1999) and, in plant interspaces, away from the competition of grasses and bushes, mycrophitic crusts

(Belnap et al., 2001). These crusts are also called biological soil crusts or, more commonly, biocrusts (Weber and Hill, 2016). Biocrusts are communities formed by photoautotrophic (algae, lichens, cyanobacteria, liverworts, and bryophytes) and heterotrophic (bacteria, fungi, protozoa, and nematodes) organisms that live on the soil surface and cover a large part of the non-vegetated surface in drylands worldwide (Belnap and Lange, 2003). These communities are critical for maintaining the multiplicity of dryland ecosystem services they provide (Rodríguez-Caballero et al., 2018) by influencing fundamental ecosystem processes including—but not limited to—nutrient cycling, soil respiration, and runon-runoff dynamics (Weber et al., 2016). Attributes of biocrust communities, such as their cover, composition, and diversity largely modulate their impacts on multiple ecosystem functions simultaneously (Bowker et al., 2011; Bowker et al., 2013), and thus have been suggested as indicators of ecosystem functioning in drylands (Tongway and Hindley, 2004; Bowker et al., 2010). As biocrusts contribute to ecosystem multifunctionality (e.g. Weber et al., 2016; Maestre et al., 2015; Bowker et al., 2016; Delgado-Baquerizo et al., 2016), changes in their composition, cover and diversity could lead to a reduction of the capacity of drylands to provide essential ecosystem services such as atmospheric gases sequestration (Weber et al., 2015) and soil fertility maintenance. Multiple lines of evidence suggest that ongoing climate change can dramatically affect biocrust communities (Rodríguez-Caballero et al., 2018) by reducing their cover and diversity (e.g., Reed et al., 2016; Ladrón de Guevara et al., 2018). Rodríguez-Caballero et al. (2018) estimated a global reduction of biocrust cover by 40% within the next 65 years, and quick reductions in their cover have already been observed in experiments simulating climate change (Ferrenber et al., 2015; Maestre et al., 2015; Ladrón de Guevara et al., 2018). For these reasons, developing methodologies to monitor biocrust compositional changes in space and time in drylands is key for the maintenance of these environments.

1.4. Remote sensing of drylands

In the last decades, remote sensing has been highlighted as an important tool for biodiversity monitoring and conservation (e.g., Nagendra, 2001; Turner et al., 2003; Pettorelli et al., 2014; Rose et al., 2015). It offers the possibility of spatializing studies from field data, avoiding many drawbacks and difficulties related to time and costs to develop standardized procedures for reproducible data gathering (Palmer et al., 2002). Remote sensing is one of the most cost-effective approaches to identify biodiversity hotspots and to predict changes in species composition, potentially providing repeated measurements and making it possible to study temporal changes in biodiversity (Gillespie et al., 2008). However, dryland remote sensing presents challenges not typically encountered in other regions, mainly related with sparse vegetation and the observed spectral signal, which can be a mixture of bare soil, biocrusts and vascular plants (Smith et al., 2019). Dryland vegetation has portions of green and dry material depending on the phenology of each species, which hampers its differentiation when based solely in spectral information (Escribano et al., 2010). Furthermore, biocrusts that might appear in plant interspaces can present similar spectral properties to soil or vegetation depending on water content (Weber and Hill, 2016; Smith et al., 2019). Thereby, there is a growing need to develop dryland-specific remote sensing methodologies able to monitor and

to distinguish between vegetation and non-vegetated surfaces, particularly when covered by biocrusts.

RGB imagery allows to distinguish between vegetation and surrounding soil when their spectral signatures are substantially different, as in drylands with sparse vegetation (e.g. Guirado et al., 2018; Laliberte et al., 2004, 2012). However, spectral differences between biocrusts and bare soil or dry vegetation are subtle (Escribano et al., 2010) and variations in soil characteristics and biocrust dominance hamper using RGB imagery for their differentiation. Nevertheless, multispectral and hyperspectral imagery allow to exploit the subtle differences in the spectral signatures between biocrusts and vegetation or soil (Weber and Hill, 2016). This kind of imagery has allowed biocrusts to be mapped in several drylands worldwide (e.g., Weber et al., 2008; Rodríguez-Caballero et al., 2014; Panigada et al., 2019).

1.4.1. Image analysis for dryland mapping

Vegetation in drylands is relatively simple to identify using medium and high spatial resolution imaging sensors (e.g., Guirado et al., 2017; Silver et al., 2019), particularly when plant interspaces are not dominated by biocrusts and plants have rounded shapes (e.g., Laliberte and Rango, 2009; Laliberte et al., 2012; Hellesen and Matikainen, 2013; Guirado et al., 2019). Pixel-based image analysis techniques work well when objects are not used as the underlying unit of the classification or the pixels are smaller than the objects (Blaschke, 2010), like in surfaces dominated by scattered patches of bare soil and biocrusts. A commonly used algorithm for pixel-based image analysis are support vector machines (SVMs; Vapnik, 2005). This methodology has been used to identify main ecosystem units in a dryland landscape including biocrusts (Rodríguez-Caballero et al., 2014), proving its success when used to differentiate similar spectral classes (Plaza et al., 2009). Nevertheless, dryland vegetation is composed of different proportions of green and dry material depending on the phenological moment (Escribano et al., 2010), and very high spatial resolutions increase the detail of vegetation characterization in these images. This increased spectral resolution increases the retrieved spectral traits and makes it difficult to establish spectral margins between not only dry and green vegetation (Escribano et al., 2010), but also between bare soil and biocrusts. Spatial information together with spectral information can increase the accuracy of discrimination between objects with similar spectral traits (Blaschke, 2010), and object-based image analysis (OBIA) uses this spatial information together with spectral information. OBIA consists of two phases: first, the segmentation of the image in homogeneous objects and, second, their classification based on similarities of spectral information, contextual information and their shape (Blaschke, 2010). Using the combined spectral information of each pixel with its spatial context (Deblauwe et al., 2008; Kéfi et al., 2007), OBIA has been used in drylands for the detection of scattered vegetation, yielding accurate results on its monitoring to evaluate its structure and functioning (e.g., Burnett and Blaschke, 2003; Hellesen and Matikainen, 2013; Guirado et al., 2017; Silver et al., 2019). Nevertheless, applying the correct image analysis technique depending on the study case and the available imagery is key for a successful characterization of the evaluated environment and potential ecosystem functioning information derived from this identification.

1.4.2. Spectral diversity to estimate α-diversity

In addition to categorical maps, which are static representations of the environment, the retrieval of continuous variables allow to gain more insights about the functional composition of ecosystems (Coops and Wulder, 2019). As biochemical and structural vegetation traits modify the spectral response of vegetation (Ollinger, 2011), variations in the optical spectrum retrieved by using spectroscopic or imaging sensors can be used to estimate variations in vegetation traits (e.g. Carlson et al., 2007; Schweiger et al., 2017; Van Cleemput et al., 2019). Thus, evaluation of spectral variations has allowed to study not only variations in vegetation traits but also in ecosystem composition (Schweiger et al., 2020). One of the most tested hypotheses exploiting spectral information to estimate the biodiversity of an environment is the spectral variation hypothesis (SVH). The SVH proposes that the larger the spectral heterogeneity of an environment is, the higher the number of species found here will be (Palmer et al., 2002). This hypothesis has been validated several times using α-diversity metrics with vascular vegetation (Schäfer et al., 2016; Wang et al., 2016; Aneece et al., 2017; Wang et al., 2018a, b). Even though measures of spectral diversity based on spectral dispersion have shown good correlations with the richness, diversity, evenness, and composition of vascular plants (e.g. Wang et al., 2018b; Rocchini et al., 2010; Gholizadeh et al., 2018), its application over biocrust surfaces remains unstudied. Producing estimations of the α-diversity of biocrusts would advance and improve actual conservation programs in drylands, helping to assess the impacts of ongoing climate change in these environments.

1.4.3. Thermal infrared imagery to estimate soil moisture in drylands

In addition to dryland composition, other variables, such as soil moisture content, can be studied using remote sensing imagery. Soil thermal conductivity changes with fluctuations on moisture level (Minacapilli et al., 2009), and thermal inertia can be used as a soil moisture estimation. Thus, materials with high thermal inertia have more uniform surface temperatures throughout the day and night than materials with low thermal inertia. But thermal inertia cannot be estimated using remote sensing, and apparent thermal inertia (ATI) is used instead as an approximation to be related with soil moisture (e.g. Tramutoli et al., 2000; Clapas and Laguardia, 2004; Van doninck et al., 2011). Maps of ATI can be obtained using estimates of the diurnal temperature cycle and estimates of co-albedo. While the surface temperature difference between the maximum and the minimum needed to obtain the diurnal temperature cycle can be obtained using multitemporal thermal infrared (TIR; the optical region of the spectrum ranging from 300-1400 nm) imagery, the co-albedo can be derived from multispectral visible-near infrared (VIS-NIR) imagery. In drylands, ATI has been found to be related with soil moisture (Van doninck et al., 2011). However, the coupling between ATI and soil moisture is not straight forward and ATI might be only directly related to soil moisture in areas with limited extent, where only a single soil or land cover type is present (van Doninck et al., 2011). Therefore, using ATI as an indicator of soil moisture is difficult in heterogeneous surfaces, such as bare soils mixed with biocrusts in drylands, and still remains a challenge to understand if this relationship can be used to estimate soil moisture in dryland soils covered by biocrusts.

1.4.4. UAVs for dryland mapping and terrain characterization

While satellite imagery (e.g., Karnieli and Soar, 1995; Qin et al., 2006; Panigada et al., 2019) has been used to monitor drylands in the last decades, the spatial resolution that can be achieved with these platforms is not enough to distinguish between sparse vegetation, bare soil and biocrusts when they appear mixed. An increased spatial resolution can be achieved using airborne imagery (e.g., Weber et al., 2008; Rodríguez-Caballero et al., 2014), but the cost of using these products is very high in most drylands' conservation and monitoring programs, and the spatial resolution is still not enough in many cases. In the last years, unmanned aerial vehicles (UAVs) have been demonstrated to be an ideal candidate to overcome these problems (Anderson and Gaston, 2013) and have facilitated the acquisition of data in drylands worldwide (e.g., Cunliffe et al., 2016, 2020; Sankey et al., 2017; Milling et al., 2018). The relative ease of use of UAVs and the miniaturization of imaging sensors has increased the range of information available, providing exciting new opportunities not only for dryland mapping, but also for digital reconstruction of the terrain (e.g., Niethammer et al., 2012; James and Robson, 2014). In this context, SfM-based techniques allow to create digital terrain models (DTMs) and orthophotos from matching features in images taken from different viewpoints (Westoby et al., 2012). SfM computer vision techniques have experienced a great upsurge recently (Micheletti et al., 2015; Smith et al., 2015; Westoby et al., 2012) and have been successfully applied in a wide range of applications in ecology and physical geography (Anderson and Gaston, 2013). Developments of this technique in the last decades (Chandler, 1999), the introduction of commercial software packages (such as Agisoft Photoscan (http://www.agisoft.ru) and Pix4UAV (http://pix4d.com; Vallet et al., 2012)) and the increase in computing power, have made SfM-based approaches available for UAV users. Doing this, representations of the terrain with subdecimetrical resolutions have allowed to evaluate the effect that terrain attributes have on vegetation (Lucier et al., 2014), spatialising studies that not so long ago were restricted to plot level.

1.4.5. Mapping biocrusts in drylands

Detailed maps of vegetation and biocrusts could help up-scaling the local effect of terrain and soil components on drylands' functioning when using coarser satellite imagery at higher spatial scales. So far, the use of optical remote sensing of biocrusts has mainly focused on mapping their distribution (Karnielli, 1997; Chen et al., 2005; Weber et al., 2008; Rodríguez-Caballero et al., 2014; Rozenstein and Karnieli, 2015; Panigada et al., 2019). However, biocrusts have proved to be difficult to monitor due to confounding factors such as water content and their tridimensional structure, which might hinder their spectral characterization in comparison to bare soil and vegetation (Weber and Hill, 2016). Due to the small size biocrusts present, works focused in biocrusts' identification have tried to exploit their hyperspectral properties (e.g., Karnieli et al., 1997; Chen et al., 2005; Hill et al., 2008; Ustin et al., 2009), but maps based on airborne platforms have not provided finer spatial resolutions than 1.5 m/pixel (Weber et al., 2008; Rodríguez-Caballero et al., 2014). However, due to the miniaturization of sensors onboard UAVs (Aasen et al., 2019) and the low altitudes they can fly at, the spatial resolution of these maps could be potentially increased to reach sub-decimetrical resolutions.

All chlorophytic biocrusts present an absorption feature at ~680 nm (Weber and Hill, 2016) related to chlorophyll-a and, to better exploit this feature, several authors (Rodríguez-Caballero et al., 2014; Weber and Hill, 2016; Rodríguez-Caballero et al., 2017; Lehnert et al., 2018; Panigada et al., 2019; Román et al., 2019) have proposed using the continuum removal (CR) algorithm (Clark and Roush, 1984). Since the CR quantifies absorption features at specific wavelengths by normalizing the reflectance spectra to a common baseline, comparability of biocrusts' absorption due to chlorophyll-*a* is ensured. Most multispectral sensors used onboard drones [e.g., MicaSense Parrot Sequoia and RedEdge(-) (MicaSense, USA) and MAIA (SAL. Engineering, Italy)] and satellites (e.g., Sentinel-2, Sentinel-3) present a band at this wavelength and this absorption feature has been detected in most studies characterizing biocrusts spectrally (e.g., Karnieli et al., 2003; Chamizo et al., 2012; Rodríguez-Caballero et al., 2014; Román et al., 2019). For this reason, using the CR at ~680 nm could help to identify biocrusts in drylands at ecosystem or landscape level and track spatio-temporal changes in their composition.

2. Research gaps and justification

Drylands cover over ~45% of emerging lands, are vulnerable to climate change and land degradation and their cover is expected to increase in the next decades. In these environments, soil and terrain properties can generate deviations from climate control on biocrusts and vegetation distribution. For these reasons, understanding these controls at ecosystem level is key for developing proper management and restoration programs in drylands. Given that remote sensing is one of the most cost-effective tools for ecosystem and biodiversity monitoring, developing reproducible methodologies for studying terrain control on dryland functioning is a key step forward for dryland conservation. In this context, several research gaps were found and addressed during this thesis.

I. Terrain attributes have a key role in nutrients and water redistribution in drylands, shaping its composition and functioning (e.g., Aguiar and Sala 1999; Puigdefábregas et al. 1999; Puigdefábregas, 2005). SfM techniques allow to digitally model the terrain and its properties when the surface to reconstruct is homogeneous (Westoby et al., 2012). However, it still remains a challenge to evaluate if this analysis can be successfully applied in drylands with complex terrains covered by dense vegetation, which hamper this reconstruction of the terrain. For this reason, evaluating whether complex drylands' terrain attributes can be extracted using SfM is a priority for dryland ecohydrology.

II. Drylands are among the most affected environments affected by anthropogenic actions (Koutroulis, 2018). However, due to their specific carbon and water fluxes (Haughton et al., 2018), methodologies used in other ecosystems can not be easily applied in these environments. For this reason, developing methodologies to evaluate changes in their vegetation communities and to relate them with human activities using remote sensing techniques are a top priority for dryland monitoring and conservation.

III. Lichen-dominated biocrusts are expected to greatly suffer changes in their composition from global change in the next decades (Ladrón de Guevara et al., 2018). Thus, it is needed to develop reproducible and feasible methodologies for their monitoring in

drylands. Spectral diversity as a tool of α-diversity monitoring has been used several times with vascular plants (e.g., Aneece et al., 2016; Schäfer et al., 2016; Wang et al., 2016), using it also to estimate vegetation functional traits (Schweiger et al., 2018). However, even though lichens are key for dryland multifunctioning (Delgado-Baquerizo et al., 2015), spectral diversity has never been used to estimate dryland lichens' α-diversity. Understanding whether spectral diversity can be used to estimate lichens' composition is key for evaluating how climate change may impact these communities and the myriad of ecosystem functions and services that rely on them.

IV. Biocrusts have a key implication in maintaining dryland functioning (e.g., Bowker et al., 2013; Maestre et al., 2015). For this reason, having accurate representations of their distribution in drylands is key to evaluate their role in dryland multifunctioning and to up-scale their local effects to regional levels. Even though methodologies to identify biocrusts have been developed in the last decades (e.g., O'Neill, 1994; Weber et al., 2008; Rodríguez-Caballero et al., 2014), a lack of spatial resolution is still missing. In this context, identification of biocrusts could be greatly benefitted by using multispectral sensors onboard UAVs. The enhanced identification offered by using multispectral imaging sensors together with the increased spatial resolution offered by low-flying UAVs could improve discrimination of dryland biocrusts when surrounded by surrounding vegetation and bare soil. Henceforth, developing methodologies to accurately represent all dryland elements is key to up-scaling local effects to larger scales.

V. TIR imagery has been already used to estimate soil moisture content in drylands, but only in homogeneous surfaces (e.g., Van doninck et al., 2011). Even though soil moisture in drylands is key for vegetation and biocrust development, its estimation through TIR imagery in surfaces covered by different land cover types, such as bare soils mixed with biocrusts, still remains a challenge and has never been evaluated. Using UAVs would allow higher frequency of TIR measurements together with increased spatial and temporal resolution (Aubrechet et al., 2016). This increased availability of TIR data could benefit studies monitoring soil moisture content, key to understanding the effects of the current global warming scenario in drylands, which expected to experience great changes (Reynolds et al., 2007). For this reason, testing if TIR imagery can be used to estimate soil moisture in drylands could greatly benefit studies in these environments.

3. Objectives

The main aim of this research thesis was to exploit optical and thermal remotely sensed imagery to determine the relationship of dryland components (i.e. vegetation and biocrusts) with the terrain where they appear. To achieve this main goal and to close the acknowledged research gaps, I focused on using multi-source imagery from airborne and UAV platforms and hyperspectral close-range imaging sensors by addressing the next specific research objectives:

- to investigate how digital photogrammetry can be used at different scales to capture characteristics of terrain and vegetation using SfM techniques (Research gap I, addressed in Chapter 1);
- to evaluate the potential of object-based image analysis to infer structural changes in communities of plants in drylands (Research gap II, addressed in Chapter 2);
- to explore whether spectral diversity can be used to capture biocrust-forming lichens' α-diversity (Research gap III, addressed in Chapter 3);
- to evaluate the effect that terrain attributes have on biocrusts' distribution using solely UAV-retrieved data (Research gap IV, addressed in Chapter 4);
- to investigate if soil moisture can be estimated in dryland heterogeneous surfaces using TIR imagery (Research gap V, addressed in Chapter 4).

4. Thesis outline

This PhD thesis is structured as a collection of scientific papers, where each chapter is an article with its own introduction, material and methods, results, discussion and conclusion. The scientific activity of this PhD project has been mainly based on two characteristic dryland environments: the Cabo de Gata-Níjar Natural Park (Spain) and the Aranjuez Experimental Station (Spain).

In Chapter 1, using Chandler et al. (1991) as a discussion point, the changes that digital photogrammetry has experienced in the last two decades and how, at the same time, many drawbacks are still present are discussed. Here I present how digital photogrammetry has evolved thanks to new software and workflows, in particular SfM photogrammetry, and the implications of using UAVs. Finally, three examples are exposed to support the discussion, showing the potential that SfM photogrammetry offers at different scales and systems: at micro-scales for monitoring micro-geomorphological changes, at meso-scales for hydrological modelling and for the reconstruction of vegetation canopies. My particular contribution to this work was the evaluation of SfM in the context of dryland hydrology, together with the discussion of other results and the general structure of the work. This chapter has been published as a scientific publication in *Progress in Physical Geography*.

In Chapter 2, I present a methodology to evaluate changes in the health of a groundwater-dependent dryland ecosystem in Spain during a 60-years long period. Using object-based image analysis and digital terrain models derived from LiDAR data, changes in the number and shape of plant individuals of this ecosystem are related with human actions. Specifically, the effect of groundwater uptake from the aquifer that feeds this ecosystem, causing seawater intrusion, and the sand extractions that took place decades ago are evaluated. The effects of these actions in relation with the number and changes in the shape of the plant individuals are discussed. My particular contribution to this work was the design of the experiments, collection of data, implementation of codes and models, analysis of the results and writing of the first and final versions of the manuscript. This chapter has been published as a scientific publication in *Remote Sensing*.

In Chapter 3, I present a methodology developed in the laboratory to capture the α-diversity of biocrust-forming lichens that could potentially be applied in the field. I took

hyperspectral images of samples of biocrust with different compositions collected in Aranjuez (Spain) and used a support vector machine algorithm to characterize their composition. I calculated several traditional α-diversity metrics (i.e. species richness, Shannon's, Simpson's, and Pielou's indices) using lichens' fractional cover data derived from their classifications. Spectral diversity was calculated as the coefficient of variation and as the standard deviation of the continuum removal algorithm at different wavelength ranges of the reflectance spectra of lichens. The relationship between α-diversity of lichens and their spectral diversity is evaluated. This chapter has been published as a scientific publication in *Remote Sensing*.

In Chapter 4, I present a methodology to use UAV-derived RGB, multispectral and TIR imagery to map dryland ecosystems and to study the effect of terrain attributes on biocrusts' distribution. RGB imagery was used to calculate terrain attributes using a SfM-based workflow and their variability is related to changes of soil properties in the study area. Multispectral imagery was used to map vegetation, bare soil and the main surface covers of biocrusts and to estimate the fractional cover of each. TIR imagery was used to evaluate the soil moisture content by creating maps of apparent thermal inertia. Using the fractional cover data and the terrain attributes, relationships between biocrusts and the terrain attributes were evaluated.

Chapter 5 concludes this thesis with the discussion and conclusions of the results of previous chapters. This chapter includes the main findings of this thesis and suggestions for future works.

Chapter 1

Two decades of digital photogrammetry: Revisiting Chandler's 1999 paper on "Effective application of automated digital photogrammetry for geomorphological research" – a synthesis

D. Fawcett, **J. Blanco-Sacristán**, P. Benaud

Published in *Progress in Physical Geography: Earth and Environment 43 (2), 299-312*

Abstract

Digital photogrammetry has experienced rapid development regarding the technology involved and its ease of use over the past two decades. We revisit the work of Jim Chandler who in 1999 published a technical communication seeking to familiarise novice users of photogrammetric methods with important theoretical concepts and practical considerations. In doing so, we assess considerations such as camera calibration and the need for photo-control and check points, as they apply to modern software and workflows, in particular for structure-from-motion (SfM) photogrammetry. We also highlight the implications of lightweight drones being the new platform of choice for many photogrammetry-based studies in geosciences. Finally, we present three examples based on our own work, showing the opportunities that SfM photogrammetry offers at different scales and systems: at the micro-scale for monitoring geomorphological change, and at the meso-scale for hydrological modelling and the reconstruction of vegetation canopies. Our examples showcase developments and applications of photogrammetry which go beyond what was considered feasible 20 years ago and indicate future directions that applications may take. Nevertheless, we demonstrate that, in-line with Chandler's recommendations, the pre-calibration of consumer-grade cameras, instead of relying entirely on self-calibration by software, can yield palpable benefits in micro-scale applications and that measurements of sufficient control points are still central to generating reproducible, high-accuracy products. With the unprecedented ease of use and wide areas of application, scientists applying photogrammetric methods would do well to remember basic considerations and seek methods for the validation of generated products.

1. Introduction

In his technical communication published in 1999, Jim Chandler (1999) identified and compiled key considerations for the application of digital photogrammetry in geomorphology. Indeed, his paper was written when automated techniques implemented in readily available software were enabling the application of digital photogrammetry by non-experts for the first time, at a relatively low financial cost, with great potential to deliver "primary data necessary for morphological representation at all scales, using the digital elevation model" (Chandler, 1999: 51). Observing this development, Chandler published recommendations to guide non-expert users towards successful application of the method, recognising that tie points identified from images had the potential to provide a much higher sampling rate than can be achieved realistically from conventional methods such as total stations or digital tacheometers.

Chandler's recommendations include a number of basic considerations that are applicable to photogrammetry at any scale, such as the importance of camera calibration and understanding its effect on the result, as well as the need for control points to constrain the results to a desired reference coordinate system, and the necessity for check points to evaluate accuracy. He also presented effective solutions for using oblique-view imagery captured from a proximal ground-based system.

Since Chandler's paper in 1999, there have been considerable developments in the discipline of digital photogrammetry, first among which is the operational implementation (and now the subsequent widespread application) of structure-from-motion with Multi-View Stereopsis photogrammetry (SfM–MVS, often abbreviated to just "SfM"). SfM photogrammetry represents a more flexible approach to photogrammetric scene reconstruction, as, unlike conventional stereo photogrammetry, the camera pose and position can be derived using image data alone, without the explicit need for reference points of known three-dimensional (3D) position in the imaged scene (Westoby et al., 2012).

Despite recent developments in photogrammetry, and as evidenced through this special issue, no less, there are still a great number of Chandler's (1999) original considerations and recommendations that remain highly relevant to scientists seeking to apply photogrammetric methods today. The purpose of this short paper is to "revisit" some of Chandler's key points and to demonstrate their relevance to the contemporary digital SfM photogrammetry workflow. There are certainly some difficulties highlighted by Chandler (1999), which have now been addressed effectively by advancements in software, computing capacity and algorithms; however, we argue that there are other challenges identified by Chandler (1999) that have been accentuated by the very same developments. Importantly, the short format of this "classics revisited" paper does not permit an in-depth analysis of the complexities of new developments in photogrammetry for the geosciences – for such matters, we redirect readers to the contents of this special issue, and to the excellent syntheses that already exist (see Micheletti et al., 2015; Smith et al., 2015; Westoby et al., 2012). Instead, we focus on a few specific aspects of Chandler's (1999) work to show, through the lens of recent application areas, the considerable recent advancements that have benefited physical geography. This includes the application to systems for which these methods may have originally seemed unsuited. Our discussion begins with Chandler (1999), but we chart progress beyond geomorphology, demonstrating how many of Chandler's points of consideration still hold relevance, across a broad suite of disciplines.

2. Photogrammetric considerations today

Advancement of photogrammetric workflows and especially the shift towards the usage of SfM photogrammetry for applications provides the motivation to reassess Chandler's (1999) recommendations for non-expert users. In the following, we seek to highlight a number of key recommendations from his original work in the context of contemporary applications from the peer-reviewed literature.

2.1. Automated camera calibration

The rise in popularity of photogrammetric methods in the recent past can, in part, be attributed to the low cost of equipment needed; with consumer-grade camera systems and affordable software able to generate satisfactory results. The cameras used for many photogrammetric applications today are far removed from the calibrated, "metric" camera systems regarded as a necessity for accurate measurements by Chandler (1999); in fact, Chandler himself later revealed the potential of using consumer-grade camera systems for close-range photogrammetry, given appropriate calibration (Chandler et al., 2005). This is simplified by automated camera calibration using self-calibrating bundle adjustment (SCBA) being refined and today handled internally by the software with minimal to no input required by the user. However, care must be taken to understand the influence of sub-optimal image networks on self-calibration and associated uncertainties (James and Robson, 2014). For weak image networks and limited camera positions, as is the case for stationary ground-based acquisitions, pre-calibration using targets may be necessary (Eltner et al., 2017). While the basic requirements for the types of sensors feasible for data acquisition for photogrammetric workflows are low, the accuracy of the acquired results can still be greatly influenced by this choice. Users should, therefore, be aware of considerations for the selection of suitable cameras and settings for their applications (discussed in detail by O'Connor et al., 2017). We point to the important issue that has arisen from the streamlining of photogrammetric workflows, which is that current systems are increasingly "black box" and so it is easy for users to overlook the need for fine-tuning available parameters to optimise results or reporting results without proper validation. As with all remote or proximal sensing workflows, validation should be considered a critical element of the practice.

2.2. The drone and software revolution in photogrammetry

Besides the development of software options and the use of low-cost sensors, what has driven a recent upsurge and essentially led to a democratisation of structural data acquisition is the emergence of lightweight drones with on-board computers as autopilots, enabled by the miniaturisation of critical sensor systems (e.g. inertial measurement unit). Chandler (1999) may not have foreseen the rise of drones as the platform of choice for photogrammetric surveys, however, his advice of "*start simple, start small*" is still highly pertinent in an age when drones facilitate the collection of terabytes of finely resolved image data, which can be processed without requiring much prior technical knowledge. Even with increased computational resources and storage, generating dense point clouds and gridded products (e.g. surface models) from image data requires considerable processing time and handling of large datasets. Inexperienced users should, therefore, acquire a prior understanding of the quality level options used by "black box" softwares and critically evaluate which one is adequate for their project – for example, by initially working on subsets and assessing intermediate products to avoid investing time into the generation of sub-optimal results. Indeed, it is important to highlight the great diversity of SfM photogrammetry software products now available. Table 1 shows a snapshot of the most widely used options, along with the number of results returned by scientific search engines. The choice of software is often motivated by availability, ease of use

and integration in larger processing pipelines, but users should be aware that many of these softwares implement subtly different methods for tie-point detection and bundle adjustment (mostly proprietary and confidential but usually based on scale invariant feature transform and Bundler) and product generation. While some cross-comparisons exist (Eltner and Schneider, 2015; Fraser and Congalton, 2018; Turner et al., 2014), they are case-specific and there remains an important need to clarify the advantages of each software – for example, for micro- and meso-scale geomorphology and vegetation-focused studies.

Table 1. Popular SfM photogrammetry software packages and the number of publications referring to them. The date of this search was 16 December 2018 and the keywords used were "[name of software] + photogrammetry" to avoid including names used in a different context. Table modified following Eltner and Schneider (2015).

	Agisoft Photoscan	Pix4D	MicMac	VisualSfM
License	Commercial	Commercial	Open source	Freeware
Scopus results	610	237	184	180
ScienceDirect results	392	76	42	59
Google Scholar results	2770	1800	816	1170

2.3. The importance of control-points

For traditional photogrammetric applications, Chandler (1999) discussed how the importance of photo-control (now, in the context of drone and airborne photogrammetry, this is usually termed ground-control point (GCP)) was a necessity for the determination of camera exterior orientation parameters, even in automated workflows, arguing for the need for high-quality control information for accurate result generation. In contrast, the SfM photogrammetry workflow can be completed without GCPs or camera-locations as input, yielding relative height information only. GCPs are required in order to register the output accurately to real-world coordinates, and it has been shown that few well-placed markers can be sufficient to achieve this (Tonkin and Midgley, 2016). GCPs also add constraints that can mitigate systematic errors in the derived point cloud, provided GCP locations are measured with sufficient accuracy (James et al., 2017a). Due to the scale, resolution and desired precision of most current photogrammetric applications, the utilisation of natural features as control points, recommended as an alternative to pre-marked points by Chandler (1999), is not advisable for drone-based surveys. Instead, current applications rely on the appropriate placement of sufficient GCP markers within the scene. By using available flight-planning software, desired GCP locations can be easily pre-determined and should favour the boundaries of the surveyed area (James et al., 2017a). Furthermore, the development of an on-board, real-time kinematic (RTK) Global Positioning System (GPS) for drones is leading towards precise direct georeferencing of aerial image data (Fazeli et al., 2016) and may at some point eliminate the need for GCPs entirely. This is a drone development that SfM photogrammetry users worldwide are no doubt watching with intent, and it will be interesting to see in the future the extent to which this streamlines or revolutionises the workflow.

A drawback of current SfM photogrammetry workflows is that metrics relating to the quality of results are limited (James and Robson, 2012), and Chandler's (1999) key concern

regarding the unquestioning application of the methodology by novice users may prove more current than ever, as SfM photogrammetry software packages become increasingly user-friendly (e.g. Pix4D), while their quality reports are either brief or difficult to interpret. As Chandler (1999) states, there may be a dangerous presumption that accurate data are being generated due to the application of sophisticated, automated techniques, today reinforced by appealing point cloud and textured mesh visualisations which can be of millimetre grain, and, thus, deceptive. Numerous influencing factors originating from flexible constraints can lead to SfM-based reconstructions being less accurate than conventional photogrammetric outputs (James and Robson, 2012), which means that while limited GCP or on-board RTK–GPS information may appear to generate plausible results, independent validation measurements or "check points" are highly recommended for validation (linking to our earlier point in Section II relating to the choice of software and its unknown influence on output data quality). Ideally, check points should be marked unambiguously within the scene, identical to GCPs in order to quantify error in all dimensions. As the deployment, collection and measurement of markers is time-intensive, a common method to provide supplemental product quality information for generated digital terrain models is the measurement of a large number of height validation points localised only using high-precision differential GPS information (Cunliffe et al., 2016). Control and validation measurements, therefore, remain an integral part of photogrammetric survey workflows today and researchers should dedicate adequate resources in order to guarantee high accuracy and reliability, even if direct georeferencing becomes commonplace.

3. Multi-scale applications in physical geography

Chandler (1999) highlighted the unique strength of the photogrammetric method as opposed to other survey techniques in its ability to deliver height information at multiple scales, ranging from micro- over meso- to macro-scale applications. While no explicit definition of these scales is provided in his original work, it becomes clear that micro-scale corresponds to extents typically covered by data from proximal sensors, meso-scale from airborne sensors and macro-scales from space-borne sensors. As foreseen by Chandler himself, at meso- and macro-scales the acquisition of robust elevation data has predominantly become the domain of airborne laser scanning (ALS) and synthetic-aperture radar (SAR) satellite missions (e.g. TerraSar-X/TanDEM-X, SAR interferometry), respectively (James and Robson, 2012; Zink et al., 2017). While photogrammetric methods are still used at these scales as low-cost alternatives enabling more frequent surveys (e.g. Bühler et al., 2015), the bulk of their application in the geosciences has increasingly shifted to smaller scales with the advent of drone-based photogrammetry, where accuracies have been shown to be comparable to ALS- and terrestrial laser scanning (TLS)-based studies (Kolzenburg et al., 2016; Wallace et al., 2016). Following Chandler's scale definition, common drone-based studies fall on the boundary between upper micro- and lower meso-scale, their spatial extent limited by maximum flying altitude, battery life and line-of-sight restrictions. Furthermore, proximal ground-based photogrammetry using consumer-grade digital cameras has also become common as a low-cost alternative to TLS or, at very small scales, where laser pulse density would prove insufficient and edge effects occur (Eltner et al., 2017; Hänsel et al., 2016; Rose et al., 2015).

In the following two sections, we shed a spotlight on three applications of photogrammetry from two scales (micro and meso) derived from our own experiments in the fields of (a) micro-scale soil erosion science, (b) landscape hydrology and (c) vegetation science. In doing so, we hope to provide some more detailed insights into the methodological developments and constraints associated with them, and reflect also on Chandler's (1999) recommendations.

3.1. Micro-scale digital photogrammetry for monitoring geomorphological change

Micro-scale soil erosion studies are essential for developing scientific understanding of soil erosion processes and potential magnitudes of soil loss. Traditionally, the quantification of soil erosion rates in laboratory and field environments has been resource intensive and heavily reliant on expert knowledge and/or specialist equipment (Armstrong et al., 2011; Berger et al., 2010; Jester and Klik, 2005). With the potential to capture fine-resolution temporal and spatial information, photogrammetry and its recent developments present an exciting platform for monitoring the evolution of soil surfaces during erosion events. Using a metric camera and rotating photo control, Chandler was able to produce a ca. 10 mm digital surface model (DSM) in a micro-scale application, as shown in Figure 1. In similar micro-scale applications (≤3 m from sensor to surface) modern non-metric digital SLR cameras, with image resolutions in excess of 18 megapixels, are capable of delivering data with sub-millimetre ground sampling distances. However, as discussed by Chandler (1999), camera calibration models and photo control influence the precision and accuracy of photogrammetry-derived surface models, ultimately limiting the final (DSM) resolution. Therefore, understanding their role in the context of modern methodologies is of particular importance when monitoring geomorphological change at the micro-scale, where reduced precision and accuracy has a negative impact on the magnitude of change that can be detected confidently.

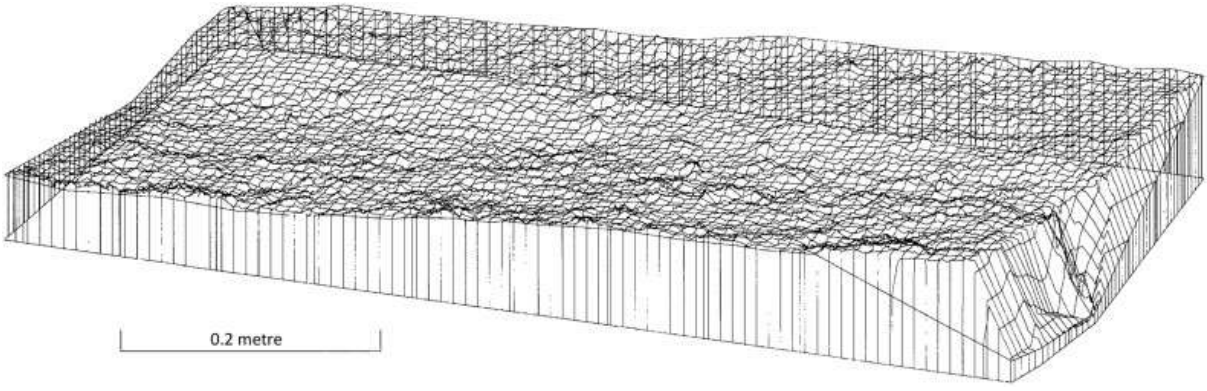

Figure 1. DSM produced by Chandler (1999, Figure 4, p.61, reprinted by permission from John Wiley & Sons, Inc.).

Adequate camera calibration models can be achieved through the standard SfM photogrammetry SCBA process for meso-scale and macro-scale applications, where the number of frames are typically in the hundreds and, thus, easily meet the criteria set out by Chandler (≥40 photo control in a minimum of four frames). However, in micro-scale applications, a single frame from two to three cameras can provide sufficient overlap and detail

within the area of interest, reducing the computational resources required for processing. To demonstrate how pre-calibration, employing a modern SCBA process, can improve model quality, we used a stereo camera setup fitted with three Canon 600D 18-55 mm III over a 0.5 × 0.3 m experimental soil plot, with 54 coded control markers around the periphery, as detailed in Benaud (2017). The tie-point precision, using the presented method by James et al. (2017b), was used to quantify the precision of the SfM model.

Figure 2 presents a wire-frame visualisation of a 2 mm DSM produced using only the experimental imagery, along with a raster of interpolated "z" axis tie-point precision estimates. By contrast, Figure 3 represents the same outputs produced using an identical workflow, but with camera calibration parameters derived for each camera from 30 frames of a control area and processed using the software's SCBA prior to the experiment, permitting a 0.5 mm DSM. Whilst both SfM photogrammetry approaches produced sub-millimetre models, without obvious distortions and similar checkpoint root-mean-squared error values, there was an order of magnitude difference in the precision of the tie points in each (relative precision of 1:720 vs. 1:3080, respectively) and, thus, the resolution of the DSM that could be confidently produced. The difference in tie-point precision also had an impact on the level of change in the "z" axis that could be detected; that is, surface changes between models must exceed the precision of the tie points. This example has illustrated that pre-calibrating cameras, in micro-scale applications, can increase the level of change that can be confidently detected using SfM photogrammetry-derived models. Accordingly, the guidelines provided by Chandler (1999) regarding the number of frames required for adequate camera calibration are still applicable for micro-scale applications today, although given the "black-box" nature of SfM photogrammetry software, it would be sensible to use far greater than four frames from each camera for pre-calibration. Pre-calibration of non-metric cameras is also an option for meso-scale applications with limited image network flexibility (James and Robson, 2014; Shahbazi et al., 2015).

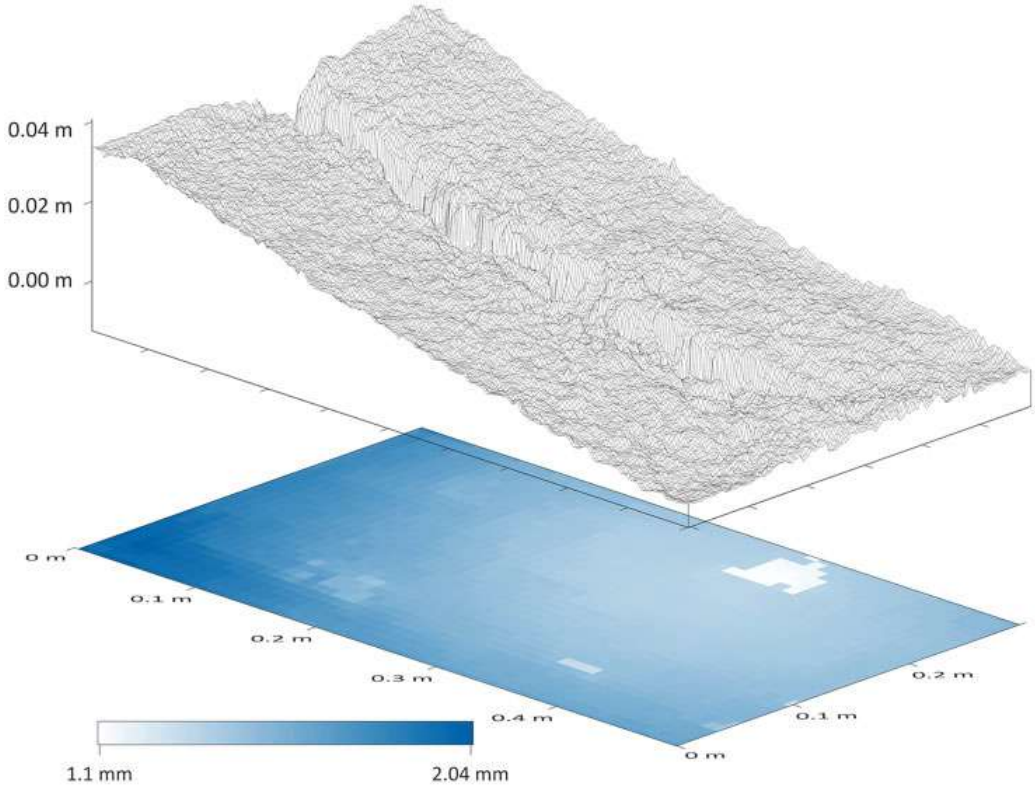

Figure 2. 2 mm wire-frame DSM produced without pre-calibration plotted above a 10 mm gridded interpolation of the median tie-point z-axis precision estimates.

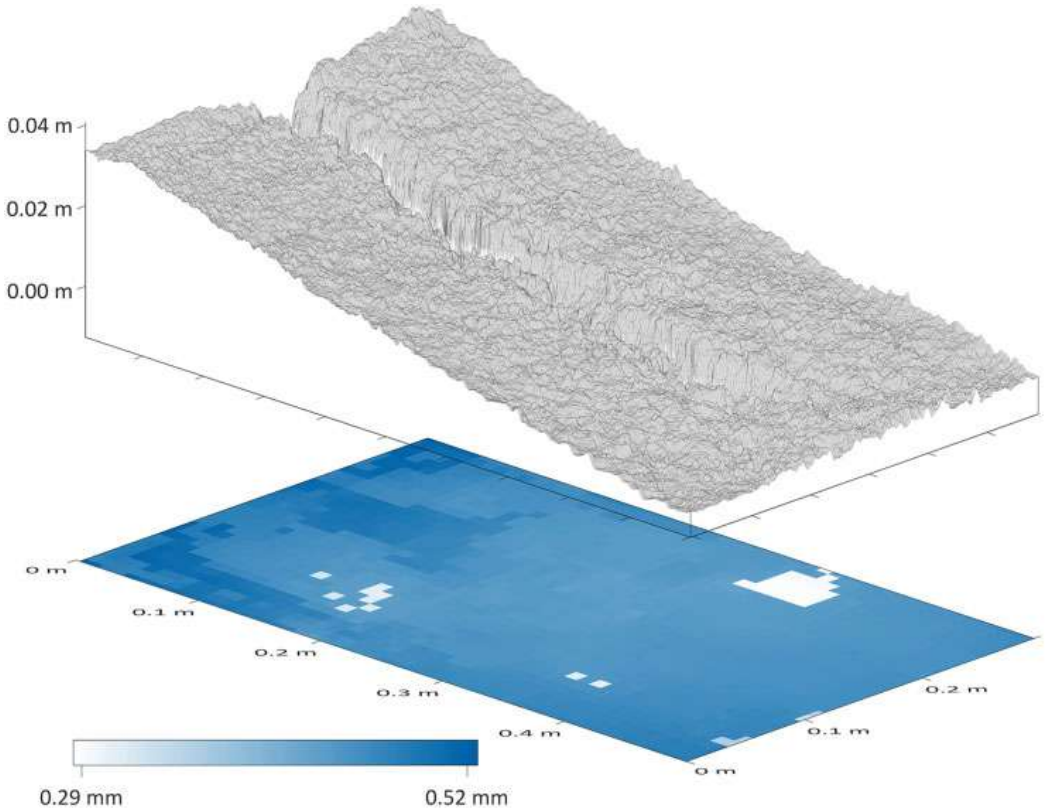

Figure 3. 0.5 mm wire-frame DSM produced with pre-calibration plotted above a 10 mm gridded interpolation of the median tie-point z-axis precision estimates.

3.2. Meso-scale digital photogrammetry for landscape characterisation

3.2.1. Hydrological applications

The application of digital photogrammetry can provide insights into the processes that modify terrain, not only at micro-scales but also at the landscape level, where it allows improved studies of geomorphological, hydrological and biological processes. By providing finely resolved Digital Terrain Models (DTM) for the derivation of topographic attributes (e.g. slope, aspect, flow length, watershed area), the previously discussed advances in photogrammetry enable the creation of landscape-scale hydrological models at low costs and high frequency, making it possible to study the effects of micro-topography (Lucieer et al., 2014), and the impact of changing terrain on the landscape's hydrology. This also allows the study of different components of hydrological systems, such as surface and subsurface flows, which are key to understanding nutrients and sediments transport in the landscape (Stieglitz et al., 2003).

However, a number of detrimental effects can limit the quality of photogrammetry-based DTMs. A common issue that arises are holes which require interpolation due to the terrain being obscured at particular camera view angles. It is, therefore, helpful if convergent images are acquired to ensure that these gaps are minimised (Nouwakpo et al., 2016). By doing so, surfaces that are occluded by the terrain or different objects (e.g. rocks or vegetation) at nadir may be visible from other angles and the derived DTM will be more complete. While Chandler (1999) listed considerations and the processing steps to be followed by the user working with oblique imagery, off-nadir views are much simpler to include in modern SfM photogrammetry workflows, especially when camera orientation per image is provided.

A further issue in the same vein for deriving terrain information by applying photogrammetric methods is vegetation cover. Unlike ALS, only limited information on the obscured ground below the vegetation canopy can be derived (Chandler, 1999). Depending on the required spatial resolution of the derived products, vegetation above a certain size threshold should, therefore, be removed from the previously generated point clouds or DSMs. To enable the filtering of vegetation, point cloud classification software such as CANUPO (Brodu and Lague, 2012) can be easily applied but such approaches require extensive fine tuning to achieve the best results. This filtering is key for ecohydrological studies, especially when the aim is to generate digital terrain/surface and hydrological models automatically.

We demonstrate the recreation of a stream network of a semi-arid landscape in central Spain (Aranjuez) using a DTM created by applying SfM photogrammetry to drone image data. This area of varying elevation and slope is covered predominantly by shrubs of different sizes and shapes. A Phantom 4 (DJI, China) quadcopter was used to acquire a total of 132 images with 75% overlap. These include two acquisitions with the camera pointing to nadir for the first and tilted by 45° for the repeat acquisition, as recommended by Cunliffe et al. (2016). The dense point cloud was created using Agisoft Photoscan (V. 1.4.0, Agisoft, St Petersburg, Russia) and the sparse vegetation was removed from the point cloud using the CANUPO plugin (Brodu and Lague, 2012), implemented in CloudCompare (V. 2.9.1, http://www.danielgm.net/cc/). This open-source software, originally designed to work with LiDAR data, allows the automatic classification of point clouds into desired classes, which, for this study, were vegetation and bare ground. Once the vegetation was removed from the point

cloud, the resulting gaps were interpolated in Agisoft Photoscan using inverse distance weighting during DTM creation (1.5 cm/pixel spatial resolution). The DTM was then used to calculate the stream network of the study area (Figure 4) using the D8 flow direction algorithm (O'Callaghan and Mark, 1989), implemented in the TauDEM toolbox (V. 5.3.7, http://hydrology.usu.edu/taudem/taudem5/index.html).

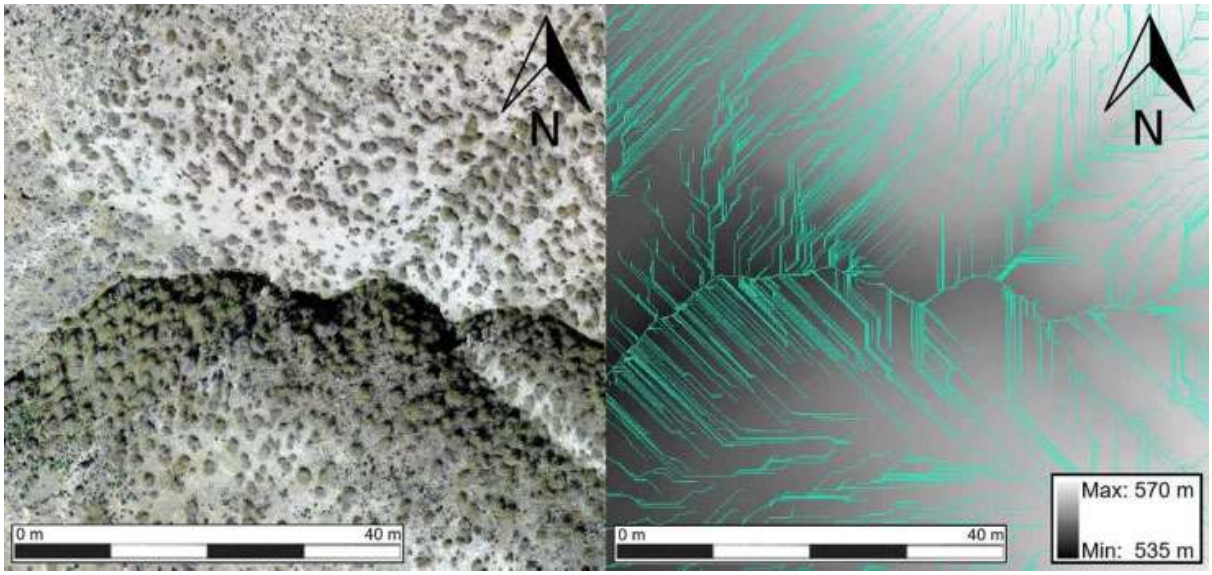

Figure 4. Detail of the orthomosaic of the study area (left) and the corresponding stream network (blue lines), created using the D8 flow direction algorithm (right).

It is evident that areas where vegetation is dense and subsequently removed from the point cloud will show a decreased level of topographic detail in the resulting interpolated DTM. This can lead to likely errors in the representation of the stream network and subsequent calculations (e.g. long segments of identical flow directions, as visible in Figure 4).

Therefore, like Chandler (1999), we argue that although digital photogrammetry-generated DTMs show potential for hydrological products, care must be taken when working with very high-resolution terrain models and interpreting their results, since slight errors can propagate within the hydrological model and yield results that do not align with reality (see Fisher and Tate (2006) for the possible consequences of DTM uncertainties), especially considering parameters such as flow-path length, which are central to sediment transport (Goulden et al., 2016). For this reason, creating adequate methodologies for removing vegetation and other objects that might influence generated digital models are a priority in order to create reliable products. While the reconstruction of the surface beneath these objects can be facilitated by acquiring images at different angles, it should be carefully assessed at which level of vegetation cover and desired spatial resolution canopy-penetrating methods such as laser scanning become a necessity.

3.2.2 Study of vegetation

While for geomorphology- and hydrology-focused applications vegetation has always presented an issue, as identified by Chandler (1999), pioneering work by Dandois and Ellis

(2010) has given rise to photogrammetry being increasingly used for studies on vegetation structure. The motivation for this is the same as in the previously presented fields and is related to financial cost and increased flexibility, which drone-based acquisitions offer. While missing ground information (e.g. from ALS) limits the applicability of photogrammetry-derived information for vegetation surveys, it has been shown that simple metrics derived from SfM photogrammetry point clouds can be successfully related to key parameters of interest such as canopy height, leaf-area index and biomass (Cunliffe et al., 2016; Dandois and Ellis, 2010, 2013; Mathews and Jensen, 2013). The ability to include arbitrary oblique-angle views of vegetation canopies in the image network has greatly improved the possibilities both for the description of canopies, moving from 2.5D closer to true 3D representations of the scene. This has been exploited by Cunliffe et al. (2016) to derive shrub canopy volumes and improve the SfM photogrammetry-derived DTM information.

Going further, the agility of drone platforms could be fully exploited to retrieve increasingly complete descriptions of single vegetation canopies. Figure 5 presents a study of a single oak tree canopy imaged by a consumer-grade, gimballed camera on a drone (DJI Inspire with Zenmuse X3, DJI, China) from many angles and high overlap using a hemispherical flight pattern. The waypoints and camera orientations were generated based on freely available code by Burkart et al. (2015) by specifying the radius and focus height above ground and imported into flight-planning software for a fully automated acquisition with a duration of approximately 10 min. The point cloud of the canopy was generated from 672 images using Agisoft Photoscan (V. 1.3.4, Agisoft, Russia) and was co-registered to a TLS point cloud of the same canopy, acquired from four positions around the tree using a Leica ScanStation P16 (Leica, Germany), for comparison. The average cloud-to-cloud distance of the SfM photogrammetry-based point cloud to the closest TLS points was 6.5 cm as computed in CloudCompare (V. 2.9.1, http://www.danielgm.net/cc/). Providing control points for an internal coordinate system as well as very small angular differences between acquisitions are crucial for a coherent and geometrically accurate reconstruction. Due to dealing with a non-metric camera with considerable lens distortion, this is also needed for reliable SCBA.

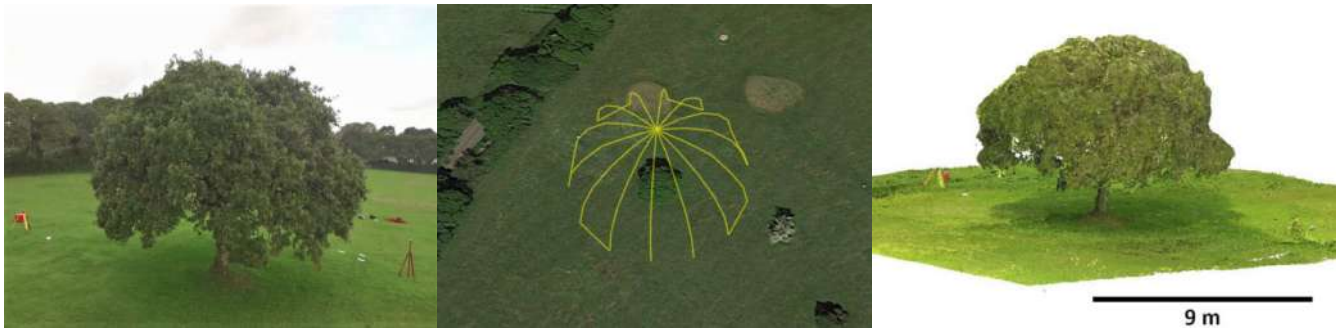

Figure 5. Left: RGB image of lone standing oak tree (*Quercus robur*); middle: hemispherical flight plan to be executed by drone displayed over high-resolution satellite imagery (Google Earth); right: RGB dense point cloud derived from the multi-angle drone-based images.

While the internal structure of this tree could only ever be captured by active laser scanning methods, the acquisition of image data from a drone platform is, by contrast, rapid and the reconstruction demonstrates the techniques' capability to deliver information on canopy shape, volume and stem information. The opportunities opened up by the agility of small aerial drone platforms coupled with the SfM photogrammetry methodology are only starting to be explored, and while the angular coverage as presented in this example can be difficult to achieve in a natural environment, it may be a viable alternative where the use of TLS is limited due to the inaccessibility of the study area.

One of the reasons that photogrammetry has previously only found fringe application for vegetation is due to the 3D complexity and instability of identified features as caused by wind conditions for many types of vegetation canopies (Duffy et al., 2017). The errors and noise within the resulting point clouds can be expected to greatly exceed those of rigid surfaces. Quantifying uncertainties is, therefore, highly important before drawing conclusions from derived information. Similar to the above example, this can be achieved by comparing results to those derived from laser scanning (ALS or TLS) point clouds (Ota et al., 2015; Wallace et al., 2016). Where such data are unavailable, uncertainty can be assessed by acquiring replicate acquisitions (Dandois et al., 2015). Complete replicate surveys are not addressed by Chandler (1999) (instead encouraging analysis of differences between single stereo pairs), presumably in part due to the cost and data volume required. The acquisition of sufficient replicates remains a limitation to resource allocation for photogrammetry-based studies, and efforts should be made seeking to employ the same methodology for deriving precision estimates developed for geomorphological applications, as presented in the previous section (James et al., 2017b).

4. Summary

Formulated as cautionary considerations when first software packages were contributing to the automation of the photogrammetric workflow, we showed that Chandler's (1999) advice regarding product validation by check points, the influence of inaccurate camera calibrations and processing high volumes of data remains relevant to the growing community of non-expert photogrammetry users. Practitioners should familiarise themselves with the importance of control and check points and know for which studies it is necessary to pre-calibrate the cameras used. Being aware of these considerations while making use of the wealth of new tools available ensures high-quality outputs capable of providing new insights in diverse areas of physical geography. Three such example applications spanning different areas and scales were presented, where developments in photogrammetry and acquisition methods open up new opportunities in micro-scale erosion modelling, landscape hydrology and the study of vegetation canopies. Although digital photogrammetry has advanced considerably since the publication of Chandler's (1999) seminal paper, many of the principles and precautions he advocates are as relevant in contemporary workflows as they were 20 years ago at the time of his publication.

Chapter 2

A Multi-Temporal Object-Based Image Analysis to Detect Long-Lived Shrub Cover Changes in Drylands

E. Guirado, **J. Blanco-Sacristán**, J.P. Rigol-Sánchez, D. Alcaraz-Segura, J. Cabello
Published in *Remote Sensing 11 (22), 2649*

Abstract

Climate change and human actions condition the spatial distribution and structure of vegetation, especially in drylands. In this context, object-based image analysis (OBIA) has been used to monitor changes in vegetation, but only a few studies have related them to anthropic pressure. In this study, we assessed changes in cover, number, and shape of Ziziphus lotus shrub individuals in a coastal groundwater-dependent ecosystem in SE Spain over a period of 60 years and related them to human actions in the area. In particular, we evaluated how sand mining, groundwater extraction, and the protection of the area affect shrubs. To do this, we developed an object-based methodology that allowed us to create accurate maps (overall accuracy up to 98%) of the vegetation patches and compare the cover changes in the individuals identified in them. These changes in shrub size and shape were related to soil loss, seawater intrusion, and legal protection of the area measured by average minimum distance (AMD) and average random distance (ARD) analysis. It was found that both sand mining and seawater intrusion had a negative effect on individuals; on the contrary, the protection of the area had a positive effect on the size of the individuals' coverage. Our findings support the use of OBIA as a successful methodology for monitoring scattered vegetation patches in drylands, key to any monitoring program aimed at vegetation preservation.

1. Introduction

A fundamental fact of ecological observation is that most living organisms do not show random distributions. In fact, environmental controls and anthropogenic impacts are determinants of the spatial patterns of these organisms. This implies that it is possible to know the performance of ecosystems through the study of the spatial distribution patterns of the organisms that live in them (Tilman and Kareiva, 2018; Maestre et al., 2005). This is particularly important in drylands where, as a result of water scarcity and edaphic limitations, vegetation appears to form isolated patches of one or more plant individuals (Ludwig et al., 2005; Thompson et al., 2011). In these ecosystems, it has been observed that the spatial pattern of these patches determines key aspects of ecosystem functioning such as primary production (Aguiar and Sala, 1999), water and nutrient cycles (Puigdefábregas, 2005), and biotic interactions (Reynolds et al., 1999; Berdugo et al., 2019). Tools to produce accurate vegetation maps at the appropriate spatial scale over time could be very useful for gaining knowledge about the health and dynamics of dryland ecosystems.

Remote sensing has proven to be the most useful tool for monitoring changes in vegetation, as it is cost-effective, allows repeated mapping, and produces information on a

large scale (Zhang et al., 2003; Tsai et al., 2018; Minasny et al., 2018). Within this technique, pixel-based methods are the most commonly used. However, these methods show several limitations for producing accurate maps of vegetation patches or plant individuals in drylands. First, pixel-based methods do not consider the spatial context in which the pixels are framed, making it difficult to identify isolated image elements. Second, they often result in a final overlap of such elements from automatic classifications, when the analysis is based on high spatial resolution images (Schiewe et al., 2001). In drylands, the land surface is characterized by scattered vegetation in a matrix of bare soil and scattered shrubs, so contextual information is very useful for image classification (Zheng et al., 2017). Both characteristics limit the possibility of identifying and classifying patches of vegetation and individual plant elements.

Several methods have emerged as an alternative to pixel-based methods for mapping individuals or vegetation patches. For example, in the case of forests, light detection and ranging (LiDAR) and very high frequency (VHF) synthetic aperture radar (SAR) images allow the characterization of various attributes of individual trees from their three-dimensional structure (e.g., Hallberg et al., 2005; Maksymiuk et al., 2014; Hamraz et al., 2017). However, this method is difficult to use when vegetation shows reduced aerial volume such as in drylands. In these cases, object-based image analysis (OBIA) can be a good solution for mapping patches of vegetation and individual plants (Blaschke, 2010), particularly because there is currently a wide variety of freely available high spatial resolution orthoimages. OBIA can provide a more accurate and realistic identification of scattered vegetation in drylands because of the combined spectral information of each pixel with the spatial context (Deblauwe et al., 2008; Kéfi et al., 2007). This method has yielded good results in the monitoring of spatial patterns, patterns, functioning, and structure of vegetation in these environments (Burnett and Blaschke, 2003; Hellesen et al., 2013).

OBIA may be particularly useful for assessing the dynamics of populations of long-lived plants of conservation concern. In this case, it is difficult and costly to assess the environmental controls of population dynamics due to their high persistence and sometimes low rate of regeneration, which requires very long-term studies (Kallio, 1971; Eriksson, 1996). It has been proposed that the maintenance of long-lived plant populations is the result of a balance between regeneration (replacement of individuals by recruiting new recruits) and persistence (maintenance of individuals in space, physically and temporarily), or a combination of both strategies (Bellingham and Sparrow, 2000; Bond and Midgley, 2001), depending on abiotic stress and biotic competition (García and Zamora, 2003). Monitoring populations of persistent individuals over time is complicated, as there are continuous disturbances in the environment that can alter their performance (Bellingham and Sparrow, 2000). However, the availability of the analysis of historical aerial orthophotographs and high spatial resolution satellite images with OBIA provides a good opportunity to reconstruct the interannual dynamics of long-lived plant populations over long periods of time, thus enabling the evaluation of changes experienced by these shrub populations.

Ziziphus lotus (L.) Lam, a long-lived shrub from Mediterranean drylands (Rey et al., 2018), shows characteristics for a multi-temporal analysis of the spatial distribution in its populations with OBIA. This shrub species depends on groundwater (Guirado et al., 2018), forms fertility islands, and is considered an engineering species (Tirado, 2009) of an ecosystem of interest for conservation at the European level (Directive 92/43/CEE). The main European

population of the shrub species is located in a flat coastal area surrounded by greenhouses in the Cabo de Gata-Níjar Natural Park, Spain. This population has been affected by several threats for many decades, including sand mining (Martínez-Lage, 1999; Tirado 2009), reducing the amount of sand available to develop the Z. lotus fertility islands; urban pressure (Daniele et al., 2010), which has reduced the potential distribution of Z. lotus; and the expansion of intensive agriculture (Cancio et al., 2016; Martín-Rosales et al., 2007), responsible for the decline in the level of the aquifer's water table, which may have caused the seawater intrusion (García García 2003; Mendoza-Fernández, 2015). Since 1944, several studies have evaluated this community of Z. lotus. Shrub patterns to identify groundwater dependence (Guirado et al., 2018), the formations of shrubs in dunes (Rivas Goday, 1944) , shrub spatial aggregation and consequences for reproductive success (Tirado and Pugnaire, 2003), and mutual positive effects between shrubs (Pugnaire et al., 2011) have been researched. Yet, the monitoring of the shrub population dynamics has never been studied. Despite most of the shrub population being located within the protected area, its temporal dynamics could be affected by several human-induced disturbances. However, due to the slow growth of shrubs and the inertia in the extinction of individuals, it is difficult to assess such dynamics without considering the population structure of the shrub species over the last several decades. This work proposes the use of remote sensing methods to map the spatial distributions of shrubs and to analyze their size and shape as a means of identifying anthropic disturbances. Our guiding hypothesis was that Z. lotus, phreatophytic shrubs, were affected by soil loss and seawater intrusion that decreased their cover area. On the contrary, after the legal protection of the area in 1987, the shrubs increased their cover area. Within this framework, the objectives of this work were as follows: (i) to make precision maps of scattered shrubs from historical remotely sensed images using OBIA and (ii) to extract information on changes in the shape, size, and spatial distribution of shrubs, and thus infer their relationships with human disturbances over a period of 60 years (1956–2016).

2. Materials and Methods

2.1. Study case

We used a reliable and reproducible methodology to monitor structural changes in scattered vegetation of a dryland coastal zone using very high spatial resolution images and OBIA. The temporal dynamics of the Ziziphus lotus (L.) Lam population in a semi-arid coastal zone was evaluated to infer the effects of human disturbances on the shape and size of individuals over a period of 60 years. Two human disturbances were evaluated: (i) the extraction of coastal sands in the 1970s (Martínez-Lage, 1999), which eliminated the aeolian sands found in the upper layer of the soil using heavy equipment and created roads and dirt tracks in the area, and (ii) the seawater intrusion in the mid-1980s caused by groundwater withdrawals for greenhouse irrigation. The withdrawals resulted in the water table of the main aquifer dropping by 30 m (García García, 2003). In addition, we evaluated the impacts of the protection of the area in 1987 in the shrub species.

The study area is located on a coastal aeolian plain in the Cabo de Gata-Níjar Natural Park, Spain (36º49'46.3''N, 2º17'37.1''W; Fig. 6). This area is one of the driest in Europe, with a mean annual precipitation, temperature, and potential evapotranspiration (PET) of 200

mm, 19 °C, and 1390 mm, respectively (Oyonarte et al., 2012). The area is a hydrogeological complex located between two wadis with numerous fractures (Goy and Zazo, 1986; Sola et al., 2007) and shows the typical landscape of arid areas with bare soil and patches of shrubs dominated by *Z. lotus* shrubs (Tirado and Pugnaire, 2003; Rivas Goday and Bellot, 1944). This vegetation is supported by a shallow, unconfined coastal aquifer composed of gravel and sand deposits located in the discharge zone at the end of the two wadis. A major fault hydrologically separates this aquifer from the main regional one (Hornillo-Cabo de Gata, Daniele et al., 2010). Consequently, inflows to the aquifer come mainly from scarce local rainfall.

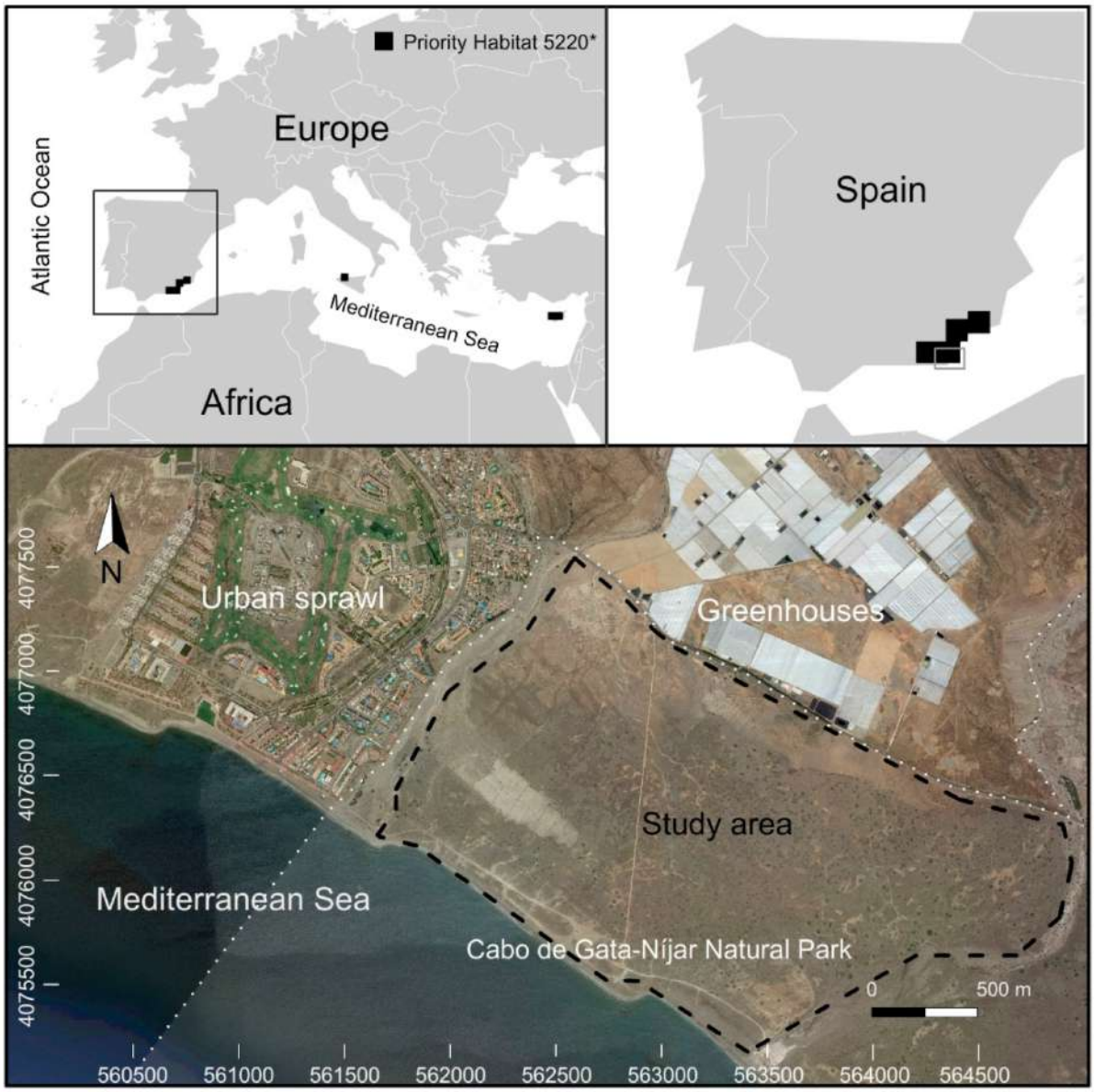

Figure 6. Upper images: the distribution of *Ziziphus lotus* priority habitat 5220* in the Mediterranean area. Lower image: Dashed line shows the study area under urban and intensive agricultural pressure in 2016. UTM projection Zone 30N; WGS 1984 Datum. Map data: Google, Maxar.

The scattered shrubs of Ziziphus lotus in SE Spain form the largest population of this shrub species in Europe. This population is protected by the Habitat Directive (5220* habitat,

92/43/CEE) and the Water Framework Directive (WFD) in Europe (Tirado, 2009). In this area, *Z. lotus* forms intricate structures of 1–3 m tall, accumulating sand under its cover called nebkas. This forms favorable microclimatic conditions under its cover with respect to the outside and increases the water availability due to hydraulic lift (Pugnaire et al., 2011), carbon exchanges, and energy cycles (Tirado and Pugnaire, 2003), creating islands of fertility (Tirado et al., 2015), which increases the diversity of animal and plant species. For this reason, *Z. lotus* is considered an ecosystem engineering species in this environment (Tirado, 2009; Cancio et al., 2016).

2.2. Datasets and Ground Truth

Eight orthoimages from two sources were used, namely, six orthoimages from the Andalusian Environmental Information Network (REDIAM) with a spatial resolution of 1 m/pixel from 1956 and 1977 (panchromatic images) and 0.5 m/pixel from 1984, 1997, 2004, and 2008 (multispectral images), and two Google Earth orthoimages from 2013 and 2016, with a resolution of 0.5 m/pixel (multispectral images). To work with the same spatial and spectral resolution, we homogenized the images to the lowest spatial resolution (i.e., 1 m/pixel) and transformed them into panchromatic images (1 band) from the three spectral band images with QGIS software v. 3.8 (manufacturer, city, state abbreviation, country). For sand mining mapping, we used airborne LiDAR data with 1 m point spacing obtained in 2011. A summary of the dataset is shown in Table 2.

Table 2. Data sources, spatial resolution, band numbers and year of the data used in the object-based shrub mapping and sand extraction estimation from airborne laser scanning (light detection and ranging (LiDAR)).

Data Source	Spatial Resolution	Band Number	Year
Andalusian Environmental Information Network (REDIAM)	1 m/pixel	1	1956
	1 m/pixel	1	1977
	0.5 m/pixel	3	1984
	0.5 m/pixel	3	1997
	0.5 m/pixel	3	2004
	0.5 m/pixel	3	2008
Google Earth™	0.5 m/pixel	3	2013
	0.5 m/pixel	3	2016
Airborne laser scanning	1 m point spacing	-	2011

Two hundred perimeters of *Z. lotus* and 200 points of bare soil with scarce vegetation were randomly taken as the ground truth. A submeter precision GPS (Leica GS20 Professional Data Mapper; Leica, Wetzlar, Germany) was used. To do this, 12 longitudinal transects along the coast with a separation of 150 m between them were followed. The perimeter was taken with a distance of 1 m between nodes and the bare soil points were taken with a separation of at least 2 m from the nearest shrub. In addition, 200 shrub perimeters were digitized in each historical image with a distance of 1 m between nodes coinciding with the pixel size of the orthoimages in QGIS software v. 3.8.

2.3. Object-Based Image Analysis

OBIA consists of two phases, namely, the segmentation of the image into almost homogeneous objects and its subsequent classification based on similarities of shape, spectral information, and contextual information (Blaschke, 2010). In the segmentation phase, it is necessary to establish an appropriate scale level depending on the size of the object studied in the image (Aksoy et al., 2015); for example, low values for small vegetation and high values for large constructions (Benz et al., 2004; Drägut et al., 2014). During the classification, the segmented objects are classified to obtain cartographies of the classes of interest using algorithms such as nearest neighbor (Kavzoglu et al., 2017). The success of the classification depends on the accuracy of the previous segmentation (Zhan et al., 2005).

2.3.1. Image Segmentation

To segment the images, we used the multiresolution segmentation algorithm implemented in eCognition v. 8.9 software (Definiens, Munich, Germany). This algorithm depends on three parameters: (i) Scale, which controls the amount of spatial variation within objects and therefore their output size; (ii) Shape, which considers the form and color of objects; if it is set to high values, the form will be considered and if it is close to 0, the color will be considered instead; (iii) Compactness, a weighting to represent the smoothness of objects formed during the segmentation; if it is set to high values, the compactness will be considered complex and if it is set to values close to 0, the smoothness will be considered as simple (Tian and Chen, 2007). To obtain the optimal value for each segmentation parameter, we used a ruleset in eCognition v8.9 that segmented the image by systematically increasing the Scale parameter in steps of 5 and the Shape and Compactness parameters in steps of 0.1 (Kavzoglu and Yildiz, 2014). The Scale ranged from 5 to 50, and the Shape and the Compactness ranged from 0.1 to 0.9. A total of 6480 shapefiles were generated with possible segmentations of *Z. lotus* shrubs in a computer with a Core i7-4790K, 4 GHz and 32G of RAM memory (Intel, Santa Clara, CA, USA). To evaluate the accuracy of all segmentations, we developed an R script to calculate the Euclidean Distance v.2 (ED2; (Liu et al., 2012) ; Equation (1)), measuring the arithmetic and geometric discrepancies between the 200 reference polygons of *Z. lotus* and the corresponding segmented objects:

$$\mathrm{ED2} = \sqrt{(\mathrm{PSE})^2 + (\mathrm{NSR})^2}.$$

ED2 optimizes geometric and the arithmetic discrepancies with the “Potential Segmentation Error” (PSE; Equation (2)) and the “Number-of-Segments Ratio” (NSR; Equation (3)), respectively. According to Liu et al. (2012), values of ED2 close to 0 indicate good arithmetic and geometric coincidence, whereas high values indicate a mismatch between them:

$$\mathrm{PSE} = \frac{\sum |s_i - r_k|}{|r_k|},$$

where r_k is the area of the reference polygon and si is the overestimated area of the segment obtained during the segmentation;

$$\mathrm{NSR} = \frac{abs(m - v)}{m},$$

where NSR is the arithmetic discrepancy between the polygons of the resulting segmentation and the reference polygons and abs is the absolute value of the difference of the number of reference polygons, m, and the number of segments obtained, v.

2.3.2. Classification and Validation of Segments

We used the k-nearest neighbors algorithm to classify the best segmentations (lowest ED2 values)in two classes, that is, (i) Ziziphus lotus shrub (Z) and (ii) Bare soil with sparse vegetation patches (S). In order to train the classification algorithm, 70% of the ground-truth samples (140 Z and 140 S) and the features of greatest separability (J) between them, obtained using the separability and threshold (SEaTH) algorithm, were used (Nussbaum and Menz, 2008; Gao et al., 2011). The remaining 30% of the ground-truth samples (60 Z and 60 S) were used as the validation set (Dobrowski et al., 2008; Wang et al., 2015), and the accuracy of the classifications was evaluated using error and confusion matrices, extracting Cohen's kappa index of accuracy (KIA) (Cohen, 1968) and the overall accuracy (OA) of them. Finally, errors in shrub segmentation were evaluated by estimation of the root-mean-square Error (RMSE) and the mean bias error (MBE) between reference polygons and segments classified as *Z. lotus* shrubs.

2.4. Sand Extraction Curvature Analysis

The evaluation of areas affected by sand extraction within the study area in the 1970s was performed using a geomorphometric analysis of the land surface (Jordan, 2003). The analyses were based on a LiDAR-derived digital elevation model (DEM) dataset, generated using an ArcGIS toolbox for multiscale DEM geomorphometric analysis. This toolbox allows the generation of a number of curvature-related land surface variables (Rigol-Sánchez, 2015), including plane, profile, mean, minimum profile, maximum profile, tangential, non-sphericity, and total Gaussian curvature; positive and negative openness; and signed average relief. Several maps were derived for each curvature variable at different spatial scales. The sizes of the analysis window ranged from 3 × 3 m to 101 × 101 m with a 14 m interval. Univariate and bivariate statistics were calculated for variables related to curvature (Jordan, 2003; Evans, 1972).

A window size of 61 m was selected for the geomorphometric analysis of the curvature of the surface, which provided a good compromise between the size of land surface depressions resulting from sand mining operations and spatial generalization. The sand extraction areas were located and digitized on a final map and validated with a field survey. In addition, an estimation of the volume of soil loss resulting from sand extractions was performed. To calculate the volume of soil loss, a new digital surface model was generated without the soil loss zones extracted with the previous curvature analysis. Then, the difference was applied to

the initial surface model with the areas identified as soil loss and to the digital surface model without soil loss, obtaining the volume of the previously identified soil loss areas

2.5. Shrub Area and Shape Dynamics

Variations in the size and number of shrubs were determined by calculating the number of shrubs lost and differences in shrub cover area between consecutive image pairs. To calculate losses and gains in the coverage of the individuals, we assumed that a resulting negative area meant a loss of surface coverage, whereas a positive area meant a gain of coverage. To determine the edge effect and the health indicator on shrubs (Collinge and Palmer, 2002), the round shape index was calculated as the ratio between the cover area and the perimeter of each shrub in different years (Schumaker, 1996). In order to evaluate whether the shrub cover reduction that occurred between 1956 and 1977 was related to sand extraction, the average minimum distance (AMD) and average random distance (ARD) between shrubs and sand extraction areas were calculated using PASSaGE v.2 software (The Biodesign Institute, Arizona State University, Tempe, AZ, USA; Rosenberg and Anderson, 2011) with 999 permutations. We assumed that the shrubs in the 1956 image rather than the 1977 image were removed during sand mining, and those that reduced their cover were affected during this process. To evaluate whether the shrub population was affected by seawater intrusion between 1977 and 1984, the AMD and the ARD between the shrubs and the coastline were calculated as previously. Shrubs affected by sand extractions (those appearing in the 1956 image but not in the 1977 one) were not included in this analysis. When calculating the AMD, the shrubs that showed a reduction in cover over the corresponding period were used, whereas for the calculation of the ARD simulated shrubs were used. In order to evaluate the effects of protecting the shrubs within the Natural Park in 1987, reduction in shrub cover and number of shrubs in the 1984–2016 period was determined.

3. Results

3.1. Segmentation Accuracy

The average values of the Scale and the ED2 were 25 and 0.45, respectively (Table 3). The most precise segmentations were from 1977 and 2016, with a Scale of 20 and an ED2 of 0.35 in both. The least accurate segmentations were the ones of 1956 and 2004, with ED2 values of 0.59 and 0.51, respectively. The lowest RMSE was obtained in the image of 2016, with a value of 46.38 m2 and an MBE of −6.36 m^2, overestimating the cover area of the shrubs. The highest RMSE was up to 120.64 m2, and in 5 of the 8 years (1956, 1977, 1997, 2004, and 2008) the area of the shrubs was underestimated as indicated by the MBE.With a computation time of 20 s per segmentation, we spent 36 h for a total of 6480 segmentations.

Table 3. Parameters used for the segmentation and their accuracies. RMSE, root-mean-square error; MBE, mean bias error; ED2, Euclidean Distance v.2. Lower (better) values of RMSE and ED2 are highlighted in bold type.

Year	1956	1977	1984	1997	2004	2008	2013	2016
Scale parameter	30	20	35	30	15	20	20	20
RMSE (m^2)	112.91	69.96	110.04	120.64	80.57	84.26	97.02	**46.38**
MBE (m^2)	14.07	15.07	−6.59	0.78	32.78	15.74	−9.96	−6.37
ED2	0.59	**0.35**	0.43	0.49	0.51	0.47	0.42	**0.35**

3.2. Classification and Characteristics of *Ziziphus lotus* Shrubs

The analysis of class separability and threshold with the SEaTH algorithm showed that the best features for discriminating between classes (i.e., those with the highest separability) were mainly related to texture (i.e., the family of features related to the Gray-Level Co-Occurrence Matrix (GLCM)) and brightness of objects (Table 4).

Table 4. Features used in the classifications and separability between them using the separability and threshold (SEaTH) algorithm. In bold, the two features for each year with the highest separability used to classify the images

Year	1956	1977	1984	1997	2004	2008	2013	2016
				Separability (J)				
Brightness	**0.92**	**1.24**	**0.88**	**0.97**	**1.04**	1.13	0.53	**0.86**
GLCM Homogeneity	0.03	0.87	0.47	0.29	0.34	0.56	0.45	0.8
GLCM Contrast	0.25	0.77	0.14	0.29	0.94	0.26	1.01	0.79
GLCM Entropy	0.06	0.38	0.38	0.24	0	0.41	**1.24**	0.56
GLCM Mean	**0.91**	**1.32**	**0.89**	**1**	**1.03**	1.14	0.57	**0.86**
GLCM SD	0.06	0.35	0.2	0.3	0.06	0.45	0.84	0.26
GLCM Correlation	0.01	0.06	0.06	0.2	0.35	**1.93**	0.94	0.59
Area	0.55	0.15	0.92	0.04	0.38	0.7	1.08	0.19
Border Length	0.7	0.54	0.27	0.35	0.06	1.37	0.79	0.07
Border Index	0.79	0.69	0.51	0.5	0.17	1.7	0.28	0.32
Compactness	0.73	0.63	0.46	0.51	0.5	1.38	0.29	0.46
Density	0.32	1.11	0.52	0.82	0.86	0.64	**1.42**	0.85
Roundness	0.63	0.35	0.25	0.36	0.22	1.44	0.29	0.2
Shape Index	0.82	0.7	0.52	0.57	0.25	**1.74**	0.22	0.4

All the classifications were highly accurate, with values of OA and KIA close to 1 (Table 5). The most accurately segmented image (OA = 0.98; KIA = 0.97) was the image of 2004, whereas the worst one was the image of 1956 (OA = 0.89; KIA = 0.79).

Table 5. Error matrix of all the classified images in the study. Z, Ziziphus lotus; S, Bare soil with sparse vegetation patches; Uncl., Unclassified; Prod., Producer's accuracy; User, User's accuracy; Held, Helden; KIA-c, KIA per class; AO, Overall accuracy; KIA, Kappa index of agreement. Highest (best) KIA values for Z (*Z. lotus*) and S (Bare soil) classes are highlighted in bold type.

Year		**1956**			**1977**			**1984**			**1997**	
Class	Z	S	sum	Z	S	sum	Z	S	sum	Z	S	sum
Z	52	5	57	47	0	47	59	2	61	57	1	58
S	7	55	62	13	60	73	0	58	58	3	59	62
Uncl.	1	0	1	0	0	0	1	0	1	0	0	0
Sum	60	60		60	60		60	60		60	60	
Prod.	0.86	0.92		0.78	1		0.98	0.97		0.95	0.98	
User	0.92	0.88		1	0.82		0.97	1		0.98	0.95	
						Total						
KIA-c	0.74	0.84		0.64	1		0.95	0.94		0.9	0.96	
OA	0.89	0.89		0.89	0.89		0.97	0.97		0.97	0.97	
KIA	0.79	0.79		0.78	0.78		0.95	0.95		0.93	0.93	
Year		**2004**			**2008**			**2013**			**2016**	
Class	Z	S	sum	Z	S	sum	Z	S	sum	Z	S	sum
Z	59	1	60	55	0	55	57	1	58	58	1	59
S	1	59	60	5	60	65	3	59	62	2	59	61
Uncl.	0	0	0	0	0	0	0	0	0	0	0	0
Sum	60	60		60	60		60	60		60	60	
Prod.	0.98	0.99		0.92	1		0.95	0.99		0.96	0.99	
User	0.99	0.98		0.99	0.92		0.99	0.95		0.99	0.96	
						Total						
KIA-c	0.95	0.98		0.84	0.99		0.9	0.98		0.92	0.99	
OA	0.98	0.98		0.96	0.96		0.97	0.97		0.98	0.96	
KIA	**0.97**	0.97		0.91	0.91		0.94	0.94		0.96	**0.99**	

3.3. Shrub Number, Area, and Shape Dynamics

During the 60-year period evaluated, the number of shrubs decreased by 742. The moment of highest shrub population was 1977, with 2625 shrubs. Conversely, the lowest number of shrubs was detected in 2016, with 1883 shrubs (Table 6). However, the total shrub area between 1956 and 2016 increased by 3692 m^2. In addition, we observed an increase in the maximum cover area value of shrubs after 1997. Finally, the most circular shrubs appeared in 1956 (i.e., the lowest values of the round shape index) and the high values of the round shape index increased over the years (Table 6).

Table 6. The number of shrubs detected each year and their cover-related average statistics. The highest number of bushes, the maximum area, the total cover area, and the lowest (best) round shape index are highlighted in bold type.

Year	1956	1977	1984	1997	2004	2008	2013	2016
Number of shrubs	2055	**2625**	2434	2345	2071	2078	1999	1883
Average area (m^2)	82.62	78.32	87.98	76.51	93.78	100.57	99.5	111.31
SD area (m^2)	67.65	67.23	79.45	66.91	76.77	82.28	77.84	83.22
Minimum area (m^2)	8	5	7	**4**	6	7	8	6
Maximum area (m^2)	525	570	643	701	586	**742**	678	658
Total cover area (m^2)	152,932	208,702	209,763	177,706	**223,322**	208,889	198,708	212,394
Round shape index	**1.32**	1.52	1.47	1.53	1.71	1.76	2.04	1.94
SD round shape index	0.16	0.26	0.26	0.27	0.36	0.38	0.47	0.46

In general, the cover area of shrubs between pairs of years showed an increase, with a trend of smaller individuals to lose more cover area than larger shrubs. In the period 1984–1997, 1423 shrubs reduced their cover area. In the period 1977–1984 (Table 7), 1650 shrubs increased their cover area.

Table 7. Change of cover and frequency of the difference in Ziziphus lotus area in the studied years (1956–2016). The negative and positive areas are the result of the subtraction between the year and its predecessor. The highest lost area, the largest positive area, the balance between greater areas, the positive frequency and the negative frequency of shrubs are highlighted in bold type.

	Difference of Area Between 1956–1977	Difference of area Between 1977–1984	Difference of Area Between 1984–1997	Difference of area Between 1997–2004	Difference of area Between 2004–2008	Difference of area Between 2008–2013	Difference of area Between 2013–2016
Negative area (m^2)	−27,797	−18,917	**−56,838**	−25,968	−32,426	−34,902	−29,684
Positive area (m^2)	42,753	69,207	31,594	**84,898**	60,870	44,147	45,101
Balance of areas (m^2)	14,956	50,290	−25,244	**58,930**	28,444	9245	15,417
Negative frequency (n)	752	903	**1423**	824	726	861	893
Positive frequency (n)	1158	**1650**	871	1405	1319	1150	978

3.4. Sand Extraction Mapping and Curvature Analysis

The results of the analyses indicated that more than 187 m^3 of sand were extracted in the study area (4.2 km^2). According to (Martínez-Lage, 1999), a visual analysis of resulting maps also suggested that sand extractions were distributed spatially following a connected network and following existing roads in the area (Figure 7).

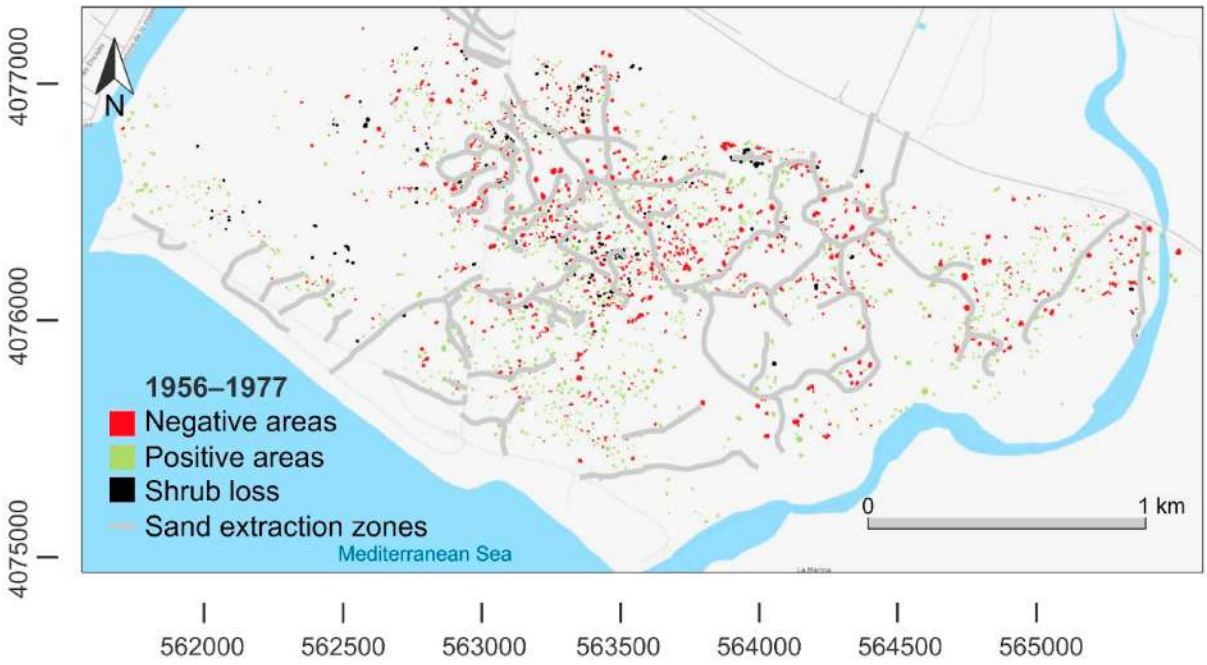

Figure 7. Sand extraction areas and differences of cover areas of Ziziphus lotus shrubs in the 1956–1977 period, when massive sand extractions took place in the study area. In red are shown negative areas, in green, positive areas, and in black, shrub loss. Spatial coordinate system, WGS84/UTM Zone 30 N.

3.5. Spatial Relationships of Shrubs with Sand Extractions, Coastline (Seawater Intrusion), and Protected Area

Between 1956–1977, 752 shrubs reduced their cover area in the sand mining event. The AMD between the shrubs and the zones of sand extractions presented an average minimum distance of 25.57 ± 37.49 m. The ARD analysis showed an average minimum distance of 127.48 m ± 23.68 m between the random simulated shrubs and the zones of the sand extractions (Figure 2). Seawater intrusion (1977–1984) reduced the cover area by 903 shrubs. The AMD analysis showed an average minimum distance of 681.32 m ± 50.15 m to the coastline. The ARD analysis showed an average minimum distance of 882.67 m ± 57.66 m between the random simulated shrubs and the coastline (Figure 8).

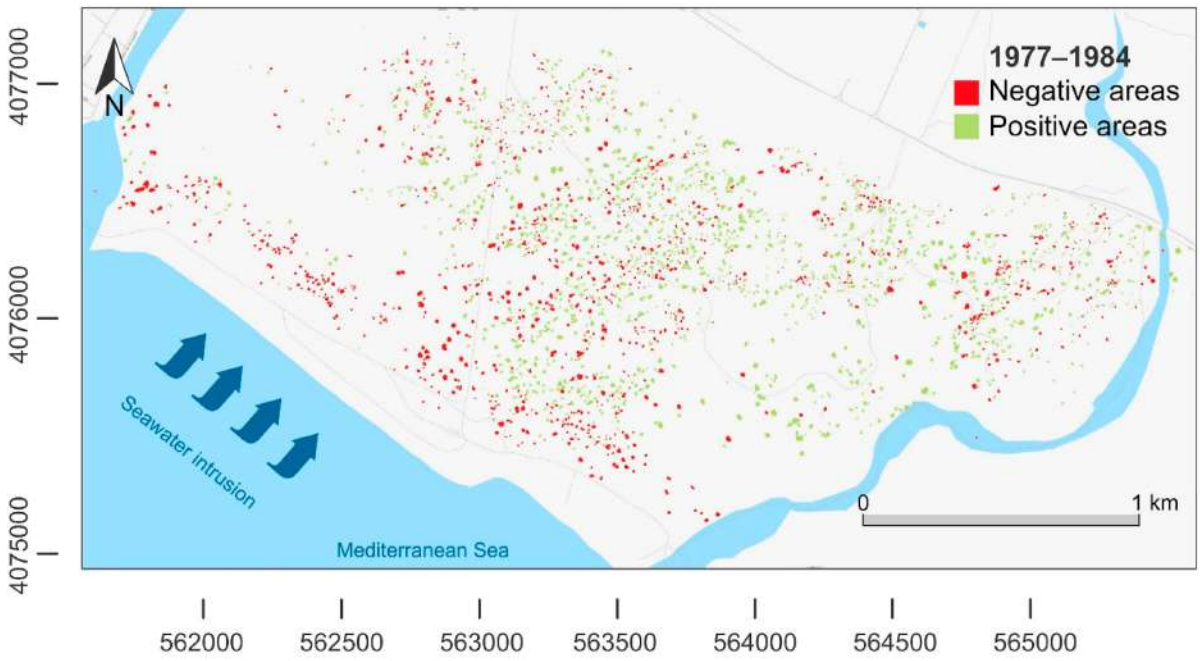

Figure 8. Differences of cover areas of Ziziphus lotus shrubs in the 1977–1984 period, when massive groundwater withdrawals took place in the study area. In red are shown negative areas and in green, positive areas. Spatial coordinate system, WGS84/UTM Zone 30 N.

In the period 1984–2016, 551 individuals were lost (Figure 9), but in the area there was a total gain of more than 23 m^2 (Table 5), coinciding with the protection of the study zone under the Cabo de Gata-Níjar Natural Park.

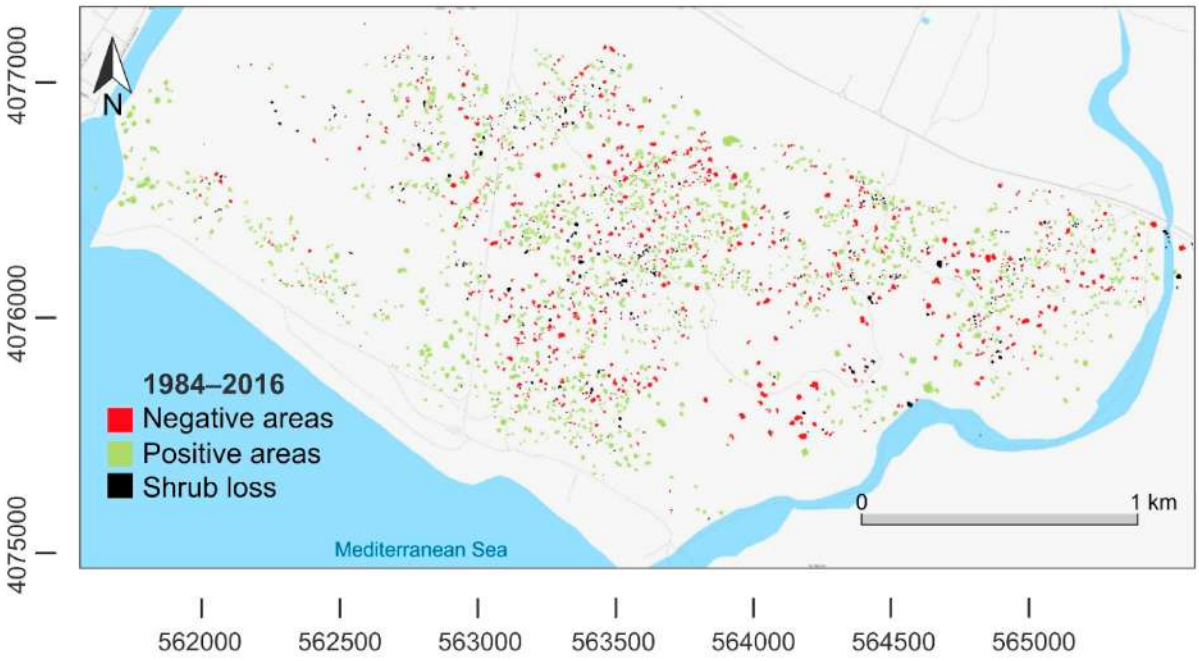

Figure 9. Differences of cover areas of Ziziphus lotus shrubs in the 1984–2016 period, when the area was protected under the Cabo de Gata-Níjar Natural Park. In red are shown negative areas, in green, positive areas, and in black, shrub loss. Spatial coordinate system, WGS84/UTM Zone 30 N.

4. Discussion

The first step in inferring human disturbances in vegetation was to generate an accurate object-based map of the study area. The high accuracies obtained in the segmentations, evaluated with the ED2 index, facilitated the classifications of the shrubs, obtaining similar accuracies to previous studies in which other species of shrubs with OBIA were detected (Hellesen and Matikainen, 2013; Laliberte et al., 2004). In the classification step, the segments of Z. lotus and bare soil with sparse vegetation showed high separability, using features related to their brightness and texture as a consequence of clear spectral differences between vegetation and bare soil (Fernández-Buces et al., 2006). According to Yu et al. (2006) and Gao et al. (2011), the best spectral-related features for discriminating between vegetation and bare soil with sparse vegetation were Brightness, and the GLCM family of features, which present high separability values in well-differentiated classes, such as vegetation and soil (Gao et al., 2011; Murray et al., 2010; Laliberte et al., 2012). The worst features to discriminate (i.e., lowest separability) were the geometry-related ones (e.g., Roundness, Area). This is contrary to previous studies, in which Roundness has been suggested as a potential feature to discriminate between rounded shrubs and bare soil (Hellesen and Matikainen, 2013; Laliberte et al., 2012; Laliberte and Rango, 2009). This discrepancy with previous studies could be explained by the high heterogeneity in the vegetation form that can present after disturbance (Aguiar and Sala, 1999). However, care must be taken interpreting these results, since shadows generated by large individuals may result in an overestimation of shrub cover area (Asner et al., 2008; Walsh et al., 2008), and individuals growing together may be underestimated as a result of appearing in the images as one (Laliberte et al., 2004).

The spatial distribution of sand extraction areas was unrelated to the topography of the area but was related to the location of older roads and tracks. This suggests that sand extractions were preferentially located to previous sand extractions in an effort to minimize labor costs. This observation is consistent with a previous study on sand extraction in the region (e.g., Martínez-Lage, 1999). According to Patridge (1992), the negative effect on shrubs by sand mining was shown in the low values of AMD calculated in the period 1956–1977. This reduction in population cover area could be related to sand mining during the 1960s and 1970s (Martínez-Lage, 1999), which might confirm the positive effect that sands have on the health of *Z. lotus* shrubs in the study area Tirado (2009) and in other areas of North Africa (Tengberg and Chen, 1998; Wang et al., 2014).

The lower value of the AMD between shrubs with reduced cover in the period 1977–1984 to the coastline suggested by the ARD that this reduction could be related to a decrease in the freshwater table and the intrusion of seawater into the aquifer (García García, 2003; Sánchez, 2008). The smallest shrubs were the most affected, which can be related to difficulties of access to groundwater due to their smaller roots compared to larger and more developed individuals (Guirado et al., 2018; Houérou, 2006). These results agree with previous studies evaluating the negative effect that seawater intrusion has on vegetated communities and groundwater-dependent ecosystems (e.g., Howard and Merrifield, 2010; Ponce, 2019).

In addition, the results of this work could be affected by other natural conditions or affections, for example, shrubs could be affected by herbivory (Aguiar and Sala, 1999; Roques et al., 2001), climate change (Sturm et al., 2001), or uncontrolled use of pesticides (Leonard

and Yeary, 1990). We argue that in order to better understand the results obtained in this work, it is necessary to complement remote sensing techniques with in situ works. For example, complementing the results obtained with the presence–absence of isotopes and relating them with the seawater intrusion (Bear et al., 1999; Mahlknecht et al., 2017) could provide a better understanding of how this phreatophytic community responds to anthropic perturbations over time.

Although 742 *Z. lotus* individuals were lost during the study period, their average size and the round shape of the shrubs were higher and bigger at the end than at the beginning of the period. However, the variability of these characteristics also increased over time, which means that a greater variety of shapes and sizes was observed in the population. This could be explained by the 1987 declaration regarding the Cabo de Gata-Níjar Natural Park, where the study area is located. This protection, in addition to a slow recovery of the aquifer after undergoing seawater intrusion between 1977 and 1984, could have contributed to a slow but continued development in time by adults, which might have better access to fresh water from the aquifer due to a more developed root system (Jackson et al., 1996) up to a length of 60 m (Nègre, 1959). Furthermore, the fact that the largest shrubs were the most developed in time supports the longevity character of this species through longevity (Rey et al., 2018), which is an important strategy for its survival in the Mediterranean region (García and Zamora, 2003). This, together with the anthropic pressure on the system, may explain the development of adult individuals, but the lack of recruitment of juveniles, as observed by Rey et al. (2018) not only in this area but also in other regions in SE Spain.

5. Conclusions

The combination of very high-resolution historical images and OBIA is a powerful tool for identifying and monitoring communities of sparse vegetation in drylands (Laliberte et al., 2004). Our results suggest that monitoring changes in the number and the cover of a shrub community in a semi-arid ecosystem could help to infer anthropogenic disturbances that affect its health. The vegetation conditions showed that the loss of sandy substrate affected *Z. lotus* negatively, either by reducing its cover or by eliminating individuals by direct sand extraction processes. In addition, seawater intrusion into the aquifer influenced the cover and structure of the shrubs close to the coastline in a period of massive groundwater extraction (García García et al., 2003), negatively affecting the smallest shrubs for the most part. However, the legal protection of the area had a positive effect on the health of the remaining individuals, which increased their coverage. The implementation of semi-automatic methods to infer the effects of human activities on shrub populations, such as the one evaluated in this study, could help improve the monitoring programs of existing protected areas. This could reduce the cost of these activities, not only in economic terms but also from a human perspective, which is key to the long-term preservation of any protected area.

Chapter 3

Spectral Diversity Successfully Estimates the α-Diversity of Biocrust-Forming Lichens

J. Blanco-Sacristán, C. Panigada, G. Tagliabue, R. Gentili, R. Colombo, M. Ladrón de Guevara, F. T. Maestre, M. Rossini

Published in *Remote Sensing 11 (24), 2942*

Abstract

Biocrusts, topsoil communities formed by mosses, lichens, liverworts, algae, and cyanobacteria, are a key biotic component of dryland ecosystems worldwide. Experiments carried out with lichen- and moss-dominated biocrusts indicate that climate change may dramatically reduce their cover and diversity. Therefore, the development of reproducible methods to monitor changes in biocrust diversity and abundance across multiple spatio-temporal scales is key for evaluating how climate change may impact biocrust communities and the myriad of ecosystem functions and services that rely on them. In this study, we collected lichen-dominated biocrust samples from a semi-arid ecosystem in central Spain. Their α-diversity was then evaluated using very high spatial resolution hyperspectral images (pixel size of 0.091 mm) measured in laboratory under controlled conditions. Support vector machines were used to map the biocrust composition. Traditional α-diversity metrics (i.e., species richness, Shannon's, Simpson's, and Pielou's indices) were calculated using lichen fractional cover data derived from their classifications in the hyperspectral imagery. Spectral diversity was calculated at different wavelength ranges as the coefficient of variation of different regions of the reflectance spectra of lichens and as the standard deviation of the continuum removal algorithm (SD_CR). The accuracy of the classifications of the images obtained was close to 100%. The results showed the best coefficient of determination (r^2 = 0.47) between SD_CR calculated at 680 nm and the α-diversity calculated as the Simpson's index, which includes species richness and their evenness. These findings indicate that this spectral diversity index could be used to track spatio-temporal changes in lichen-dominated biocrust communities. Thus, they are the first step to monitor α-diversity of biocrust-forming lichens at the ecosystem and regional levels, a key task for any program aiming to evaluate changes in biodiversity and associated ecosystem services in drylands.

1. Introduction

Biocrusts are communities formed by photoautotrophic (algae, lichens, cyanobacteria, liverworts, and bryophytes) and heterotrophic (bacteria, fungi, protozoa, and nematodes) organisms that live on the soil surface and cover a large part of the non-vegetated surface in drylands worldwide (Belnap and Lange, 2003). These communities influence fundamental ecosystem processes in drylands, including—but not limited to—nutrient cycling, soil respiration, and runon-runoff dynamics (Weber et al., 2016), and are critical for maintaining

the multiplicity of ecosystem services they provide (Rodríguez-Caballero et al., 2018). Attributes of biocrust communities, such as their cover, composition, and diversity, largely modulate their impacts on multiple ecosystem functions simultaneously (Bowker et al., 2004, 2013), and thus have been suggested as indicators of ecosystem functioning in drylands (Bowker et al., 2010; Tongway and Hindley, 2004).

Multiple lines of evidence suggest that ongoing climate change can dramatically affect biocrust communities, reducing their cover and diversity (Reed et al., 2016. Rodríguez-Caballero et al., 2018 estimated a global reduction of their cover by 40% globally within the next 65 years, and quick reductions in their cover have already been observed in experiments simulating climate change (Ferrenber et al., 2015; Maestre et al., 2015; Ladrón de Guevara et al., 2018). As biocrusts contribute to ecosystem multifunctionality (Weber et al., 2016; Maestre et al., 2015; Bowker et al., 2013; Delgado-Baquerizo et al., 2016), changes in their composition, cover and diversity could lead to a reduction of the capacity of drylands to provide essential ecosystem services such as atmospheric CO2 sequestration and the maintenance of soil fertility. For this reason, finding accurate and operational methods to estimate the cover and diversity of biocrust constituents is a key goal for any ecosystem monitoring program in drylands.

Remote sensing has been highlighted several times as an important tool for biodiversity monitoring and conservation (Nagendra, 2001; Turner et al., 2003; Pettorelli et al., 2014; Rocchini et al., 2015). It is one of the most cost-effective approaches to identify biodiversity hotspots and to predict changes in species composition, potentially providing repeated measurements and making it possible to study temporal changes in biodiversity (Gillespie et al., 2008). In this context, the spectral variation hypothesis (SVH) proposes that the larger the spectral heterogeneity of an environment is, the higher the number of species found here will be (Palmer et al., 2002). This hypothesis has been validated several times using α-diversity metrics with vascular plants (Schäfer et al., 2016; Wang et al., 2016; Aneece et al., 2017; Wang et al., 2018a; Wang et al., 2018b). Even though measures of spectral diversity based on spectral dispersion (i.e., the coefficient of variation (CV) or the standard deviation (SD)) have shown good correlations with the richness, diversity, evenness, and composition of vascular plants (Wang et al., 2018b; Rocchini et al., 2010; Gholizadeh et al., 2018), the SVH has never been tested using lichens.

The use of optical remote sensing of biocrusts so far has mainly focused on mapping and monitoring their distribution (Karnieli, 1997; Chen et al., 2005; Weber et al., 2008; Rodríguez-Caballero et al., 2014; Rozenstein et al., 2015; Panigada et al., 2019) and only one study (Waser et al., 2007) investigated lichens' α-diversity at the landscape level through correlation of high-resolution data with field samples. Since biocrusts are spectrally characterized by narrow absorption features in specific spectral regions (Weber and Hill, 2016), hyperspectral data have shown potential when discriminating them from vegetation and other soil features (e.g., (Weber and Hill, 2016; Ustin et al., 2009; Weksler et al., 2018; Rodríguez-Caballero et al., 2017). However, confounding factors such as water content and biocrust tridimensional structure might hinder their spectral characterization. For this reason, several authors (Rodríguez-Caballero et al., 2014; Panigada et al., 2019; Weber and Hill, 2016; Rodríguez-Caballero et al., 2017; Lehnert et al., 2018; Román et al., 2019) proposed the use of the continuum removal (CR) algorithm (Clark and Roush, 1984) to ensure the comparability of biocrusts' absorption

features. The CR quantifies the absorption features at specific wavelengths, normalizing the reflectance spectra to a common baseline. This is achieved by approximating the continuum between local spectral maxima through straight-line segments: a value of 1 is assigned to the local maxima, and a value between 0 and 1 is obtained in correspondence of the absorption features. This approach might be particularly useful to enhance the discrimination of lichens, which are characterized by subtle spectral differences (Rees et al., 2004).

In this framework, the objective of this study was to apply the SVH to capture the α-diversity of lichens to support dryland monitoring by (i) evaluating the potential of hyperspectral high spatial resolution images to identify biocrust-forming lichens (at the genus level); (ii) exploring the relationships between spectral diversity metrics and the α-diversity of lichens within biocrust communities.

2. Materials and Methods

2.1. Study Area and Sampling

The study area is located in Aranjuez, central Spain (40°01′53.9″N 3°32′50.8″W; Fig. 10). The climate is semi-arid Mediterranean, with mean annual temperature and rainfall of 15 °C and 349 mm, respectively. The plant cover is below 40%, and is dominated by *Macrochloa tenacissima* and other small shrubs, such as *Helianthemum squamatum* and *Gypsophila struthium*. A well-developed biocrust community, a mixture of lichens and mosses, is present between vegetation, covering up to more than 50% of the plant interspaces. In lichen-dominated biocrusts, *Acarospora* spp., *Buellia* spp., *Diploschistes* spp., *Fulgensia* spp., *Psora* spp., and *Squamarina* spp. are the most abundant genera, while in moss-dominated biocrusts, *Pleurochaete squarrosa*, *Tortula revolvens*, and *Didymodon acutus* are the most abundant mosses. Since this study focused on lichens, we decided to cluster the mosses identified (under the term *Moss*). Finally, in patches of soil dominated by cyanobacteria, genera as *Microcoleus* spp., *Tolypothrix* spp., and *Nostoc* spp. are present (Cano-Díaz et al., 2018). See Maestre et al., 2013 for a species list of the biocrust-forming lichens and mosses in our study area.

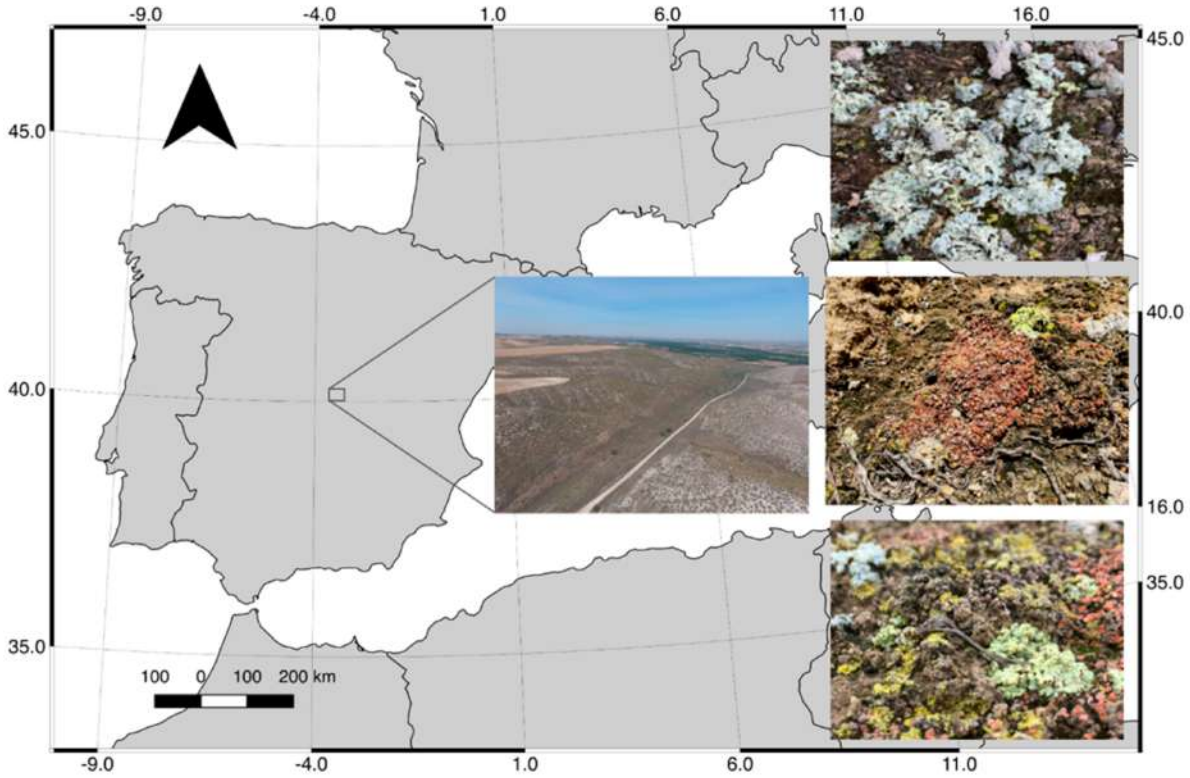

Figure 10. Location of the study area in central Spain and some examples of the dominant lichen communities found in the area.

Following the sampling protocol described in (Weber et al., 2008), we collected 54 biocrust samples using Petri dishes of 8.5 cm of diameter from 18 plots (three samples per plot randomly chosen). These plots were distributed following two altitudinal transects in two separated slopes of the study area with different exposures (north- vs. south-facing). Each transect was divided in three levels depending on the height of the transect with respect to its base, placing three plots on each level.

2.2. Hyperspectral Imagery Acquisition

Hyperspectral images of the biocrust samples were acquired with a hyperspectral scanning imaging system (Garzonio et al., 2018) measuring spectral reflectance in 840 bands in the visible (VIS) and near-infrared (NIR) spectral region (i.e., 380–1000 nm), with a spectral resolution of 2–3 nm (calculated at full width at half maximum; Fig. 11). The system consists of a custom high-precision linear stage that embeds a hyperspectral imaging spectrometer (Hyperspec® VNIR, HeadWall Photonics, USA) and a dedicated halogen stable light source (i.e., 600 or 1000 W, LOT Quantum Design). Powered by an electrical engine, both the spectrometer and the halogen light source are able to move back and forth at a defined speed. The system is a push-broom scanner and it measures lines of 1004 pixels while moving forward by means of the linear stage until an image of the whole studied object is collected. We used a water-filter tube between the lamp and the mirror reflecting the light to the samples to avoid sample overheating.

Figure 11. Picture of the system used to acquire the hyperspectral imagery. The system consists of: (**a**) samples holder and motor driver; (**b**) HeadWall VNIR camera thermostated by heaters; (**c**) stable halogen lamp; (**d**) calibrated Lambertian Spectralon panel; (**e**) PC connected to the spectrometer by a dedicated interface.

Two sets of images were collected: one with the dry samples (dry set) and another 10 min after evenly watering the samples with 30 mL of distilled water (wet set). A total of 18 images (six samples on each set; Fig. 12) with a spatial resolution of 0.091 mm were taken. A calibrated white Lambertian Spectralon® panel (Labsphere, North Sutton, USA) was placed close to the samples to calculate the reflectance as the ratio between the radiance reflected by the biocrust samples and the panel. The instrument's dark current signal was measured by manually closing the imaging spectrometer aperture prior to capturing each image and subtracted from the measured radiance.

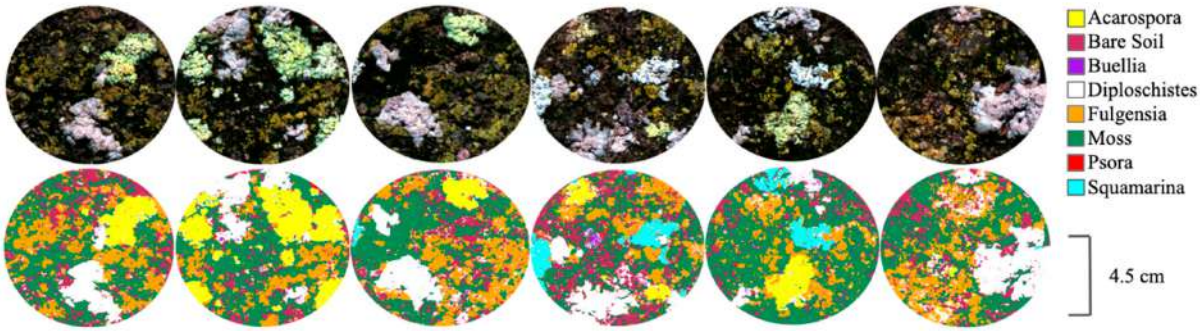

Figure 12. True color composite samples (upper images) from one of the hyperspectral images used and the classification derived (lower images).

2.3. Images Processing and Classification

Both sets of images were pre-processed and classified to characterize the composition of each sample. First, the parts in the images not belonging to the samples were masked and the

reflectance was computed between 420 and 900 nm. To reduce the noise in the measured signal, a Savitzky-Golay smoothing filter (Savitzky and Golay, 1964) was applied using a 20 band-window width. A minimum noise fraction (MNF) transformation was applied to the smoothed reflectances to synthesize the main information in a reduced number of MNF components as well as to remove the residual noise in the data. The first 15 MNF components of each image transformation were used as input of the classification algorithm.

The training set for the classification was created by selecting pure endmembers of each classes by visual-identification on the images of the samples. The following classes were considered in the classification process: *Acarospora* (*Acarospora* spp.), *Buellia* (*Buellia* spp.), *Diploschistes* (*Diploschistes* spp.), *Fulgensia* (*Fulgensia* spp.), *Psora* (*Psora* spp.), *Squamarina* (*Squamarina* spp.), *Moss* and *Bare Soil*. Biocrust classification was performed with a supervised machine learning method, using a total of around 1000 pixels per class identified in each image to train the support vector machine (SVM) algorithm.

The SVM is a supervised classification method based on statistical learning theory (Corters and Vapnik, 1995; Vapnik, 2005). Using training samples from the classes of interest, it separates them by a decision surface, called hyperplane, that maximizes the margin between them. The closest training samples to the hyperplane are the ones used by the algorithm, called support vectors. SVM is a binary classifier in its simplest form, but can also act as a multiclass classifier by creating a binary classifier for each possible pair of classes. SVM uses a penalty parameter that allows a certain degree of misclassification. Fine tuning is important to avoid overfitting of the model because increasing its value increases the cost of misclassifying points and forces the creation of a more accurate model, which might be not generalizable. We used a radial basis kernel function, which usually performs well in remote sensing applications (Foody et al., 2006). This kernel is controlled by two parameters that determine the final classification accuracy, the penalty parameter (C) and the width of the Gaussian kernel (c). A large C reduces the training dataset error, but may result in model overfitting to the training data, reducing their generalizability. We used the SVM in a pairwise classification way to classify the images and evaluate the best parameters to use for each classification using the LIBVSM library (Rodríguez-Caballero et al., 2014; Chang and Lin, 2001).

2.4. Validation of Classifications

The validation set for each classification was created selecting 300 pixels per class of pure endmembers by visual-identification. We assessed the accuracy of the classifications using the receiver operating characteristics (ROC) technique (DeLeo, 1993) and the area under the curve (AUC; Bradlye, 1997; Hanley and McNeil, 1982) derived from it. A ROC graph is a two-dimensional depiction of a classifier's performance (Fawcett, 2006) and is constructed calculating the sensitivity and specificity of the resulting classification for each possible classification threshold, where

$$\text{sensitivity}=a/a+c$$
$$\text{specificity}=b/b+d,$$

with a and d as the true positives and the true negatives for a certain classification, respectively, and b and c as the corresponding false positives and false negatives. The

'sensitivity' is the probability that a pixel of a particular class is correctly classified, while the 'specificity' is the probability that a pixel not belonging to that class is correctly classified. In this way, the best performing classification would be that with the highest possible value of both sensitivity and specificity. We evaluated the probability of detection (calculated as the sensitivity) against the false positive rate (calculated as 1 – specificity). A ROC graph was calculated for each of the classifications produced (i.e., 18 classifications, six samples each), averaging the curves obtained for each class.

From each ROC graph, we calculated its corresponding area under the curve (AUC), that is an overall quantitative performance score of the classification that allows to reduce the ROC performance to a single scalar value independent of a single prediction threshold (Bradlye, 1997; Fawcett, 2006). The AUC represents the probability that a randomly chosen positive sample is correctly classified with greater suspicion than a randomly chosen negative one (Hanley and McNeil., 1982). This value might range from 0.5 (a random assignment to the class of interest) to 1 (a perfect classification). The AUC values were calculated by joining the points of the ROC through a composite trapezoid rule using the AUC function from the R package DescTools (Signorell et al.). To assess classification accuracy, we also evaluated the average accuracy creating a confusion matrix with the average accuracies from the classifications of each set of images (i.e., dry and wet), extracting the overall accuracy and Cohen's kappa coefficient (Congalton, 2008). The points used to create these matrices were the same used to create the ROC curves.

2.5. Computation of the Spectral Diversity

Using the classifications previously obtained, we calculated, for each biocrust sample, the average spectral reflectance of each lichen genera from the reflectance images. We then calculated the pigment absorption features by the continuum removal method, normalizing the spectra to a common baseline. Several metrics were then calculated as indicators of spectral diversity for each sample: the coefficient of variation (CV; i.e., ratio of the standard deviation to the mean), calculated between 420–900 nm ($CV_{420\text{-}900}$), between 550–750 nm ($CV_{550–750}$), and at 680 nm (CV_{680}), and the standard deviation of the continuum removal (SD_CR), calculated between 550–750 nm ($SD\_CR_{550–750}$; i.e., absorption feature related to the presence of chlorophyll) and at 680 nm (SD_CR_{680}; i.e., maximum peak of this absorption feature).

2.6. Biodiversity Metrics

The fractional cover of each lichen class (classified at the genus level) was used to calculate the following α-diversity metrics for each sample: species richness (S), Shannon's index (H'; (Shannon, 1948), Simpson's index (D; (Simpson, 1949) and Pielou's index (J'; Pielou, 1966). The details of the calculation are reported in Table 8. These metrics were calculated using the 'vegan' R package, version 2.4–5 (Oksanen et al.).

Table 8. Diversity metrics used in this study. p_i is the fractional cover of the i^{th} class.

α-Diversity Metric.	Formula
Species richness (S)	S = Number of classes
Shannon's index (H')	$H' = -\sum pi * \ln(p_i)$
Reciprocal of Simpson's index (D)	$D = 1 / \sum p_i^2$
Pielou's index (J')	$J' = H' / \ln(S)$

2.7. Statistical Analysis

To evaluate the spectral diversity metrics that better capture the α-diversity of biocrust-forming lichens, we evaluated through linear regression models the relationships between spectral diversity (calculated as the average CV and CR of the three samples from each plot) and α-diversity metrics (species richness, Shannon's index, Simpson's index, and Pielou's index), calculated using the fractional cover of each plot (the average of three samples). Due to the high heterogeneity of four plots, their samples were not averaged, and the values of the single samples were used in the analysis. Species richness was calculated as the total number of genera observed in the three samples from each plot. Due to the small sample size (n = 26) in this analysis, the cross-validated statistics obtained with the leave-one-out cross-validation procedure were also computed to compare performances of different spectral diversity metrics in predicting α-diversity.

3. Results

3.1. Classifications and Accuracy Evaluation

The classification (Fig. 12) of both dry and wet images was highly accurate. The high values of the AUC derived from the ROC curves showed that the SVMs used were successfully trained to classify biocrust-forming lichens (Fig. 13).

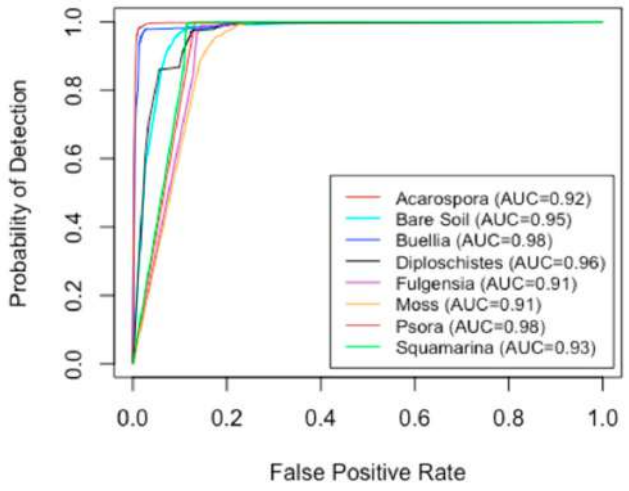

Figure 13. ROC curves of the genera classifications and the derived AUC values of the wet samples.

The classification of the wet dataset had an average AUC of 0.95 (Fig. 13), a kappa coefficient of 0.97 and an overall accuracy of 97.83% (Table 9). The lowest accuracies were achieved classifying *Moss* and *Fulgensia*, with AUCs of 0.91 and 0.92, respectively. The most accurate results were obtained for *Buellia* and *Psora*, with AUCs values of 0.99 and 0.98, respectively. Bare soil was the most confused class, mostly with moss, even though it was better classified than in the dry set of images, where it presented an AUC of 0.82. The dry set was less accurate, presenting an average AUC of 0.93, an average kappa coefficient of 0.95 and an overall accuracy of 95.69%. All the lichens were accurately classified, with values of AUC over 0.95, similar to those obtained from the wet set. Moss presented the lowest accuracy, with an AUC of 0.75, and was the most misclassified, being confused mostly with bare soil.

Table 9. Average confusion matrix obtained crossing the ground truth (columns) with the results of the classification (lines) performed on wet samples. 300 pixels per class in each image were randomly selected as validation set to create this matrix. A total of 20,400 random selected pixels were used. The ground truth (%) shows the class distribution in percent for each ground truth class.

	Ground truth (%)							
	Acarospora	**Bare Soil**	**Buellia**	**Diploschistes**	**Fulgensia**	**Moss**	**Psora**	**Squamarina**
Acarospora	99.96	0	0	0.04	0	0	0	0
Bare soil	0.04	97.55	0	0.72	0.4	0.32	1.06	0
Buellia	0	0	93.45	4.26	0	0	0	0.98
Diploschistes	0	1.63	6.49	94.89	0.24	0	1.3	0.23
Fulgensia	0	0.04	0	0	99.31	0	0.05	0
Moss	0	0.76	0	0	0.05	99.65	0.3	0
Psora	0	0.02	0	0	0.05	0.03	97.29	0
Squamarina	0	0	0.06	0.09	0	0	0	98.79

3.2. Spectral Characterization of Biocrusts

Dry biocrusts had increasing reflectances from the blue region until 700 nm. In the visible region the reflectances of various biocrust classes differ because of different pigment content and composition (Fig. 14) differences in the NIR region are mainly related to the biocrust tridimensional structure. Lichens presented higher reflectances than bare soil and moss across the whole spectrum. Their higher reflectance in the NIR region is related to their more developed structure, which causes multi-scattering of light in this region. *Acarospora*, *Squamarina*, *Buellia*, and *Diploschistes* are light-colored lichens that showed higher reflectances in the visible region; *Psora* presented the lowest reflectance among lichens. Mosses had the lowest reflectance due to their darker color and less developed structure, resulting in a reduction of light scattering. The application of the continuum removal algorithm in the spectral range 450–900 nm highlighted the absorption features caused by different pigments. The chlorophyll absorption feature at 680 nm was present in all the classes. Bare soil showed a weak absorption feature at 680 nm, evidencing the presence of cyanobacteria colonizing the soils interspace within lichens and moss patches. *Psora* showed an absorption feature around 550 nm due to phycoerythrin, which is absent in the other lichens. An absorption feature at 500 nm related to the presence of carotenoids was observed in mosses. *Fulgensia*

presented an absorption peak around 490 nm due to the presence of carotenoids or phycoerythrin.

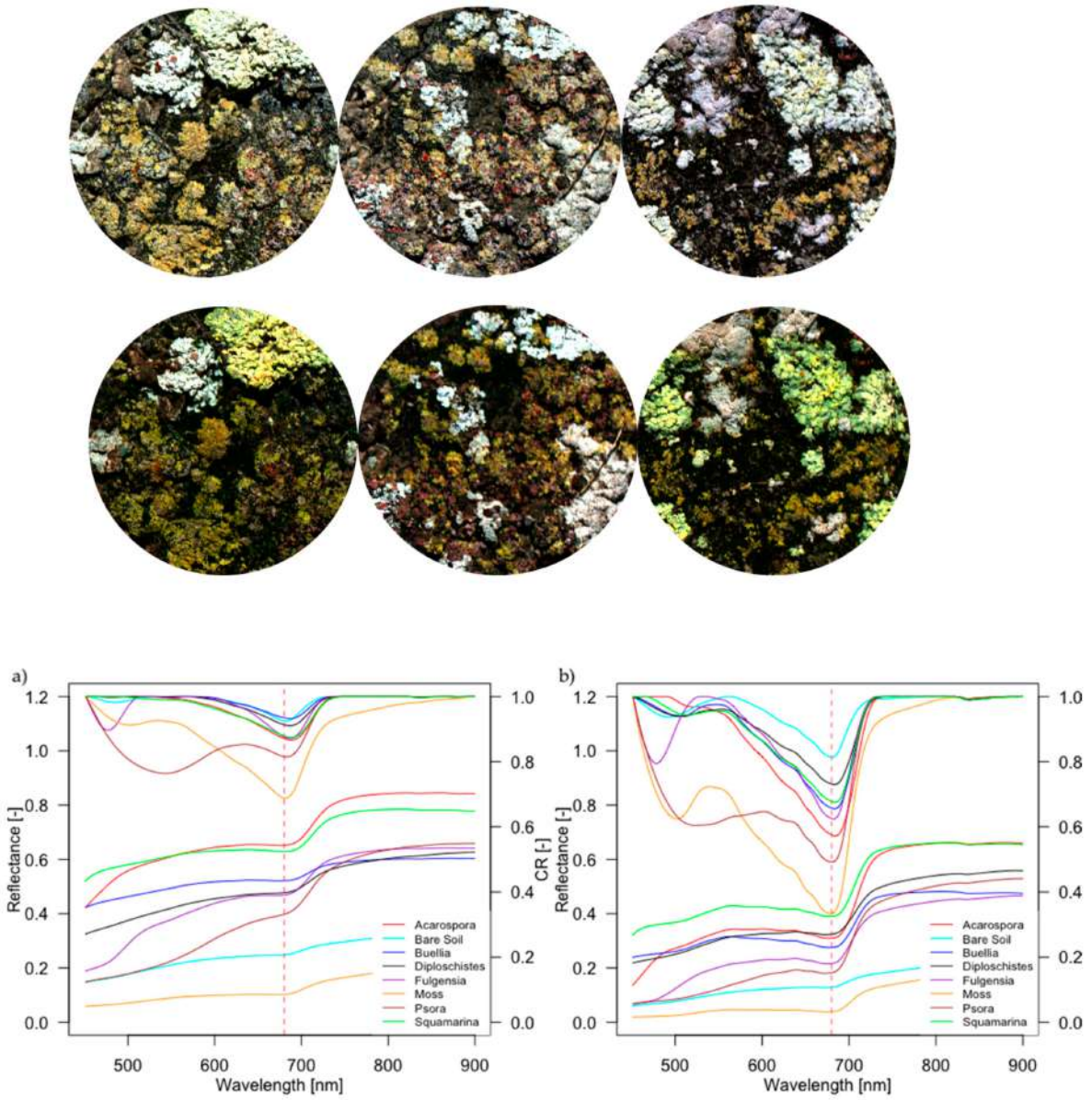

Figure 14. Top**:** RGB composites of some of the samples used in the study, showing the change of color that takes place from dry (first row) to wet (second row) state of biocrusts. Down: Mean reflectance spectra and mean continuum removal absorption spectra between 450–900 nm of the biocrust classes and bare soil studied in this work. The red dashed line marks the absorption feature at 680 nm related to the presence of chlorophyll. (a) Dry samples; (b) Wet samples.

Watering had a strong effect on biocrust optical properties (Fig. 14b), causing a decrease of reflectance across the whole spectrum. The change was particularly evident in the absorption feature caused by chlorophyll at ~680 nm, which became deeper, evidencing the abrupt change in the reflectance from red to NIR, typical of vegetation (i.e., red edge region). The continuum removal algorithm allowed to enhance this absorption feature at ~680 nm related to the activation of chlorophyll after watering, increasing its variation (Fig. 15).

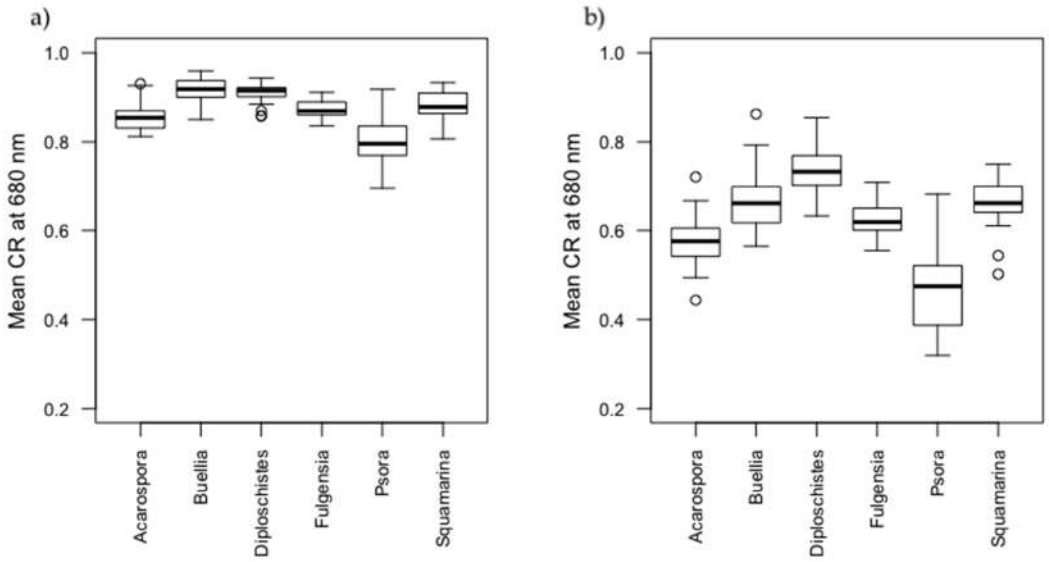

Figure 15. Mean continuum removal at ~680 nm of the lichen classes identified. Bars indicate the first and third quartile of each class. (**a**) dry samples; (**b**) wet samples.

3.3. Fractional Cover of Biocrusts and Diversity Metrics

The most abundant classes were moss and bare soil, covering more than 76% and 46% of the surface in some samples, respectively (Table 10). The most abundant lichen was *Diploschistes*, while the least were *Psora* and *Buellia*, which appeared scarcely. Species richness ranged from 2 to 6. Shannon's index ranged from 0.18 to 1.53, with a mean value of 1.03, and Simpson's index from 0.08 to 0.77, with a mean of 0.56. Pielou's index ranged from 0.14 to 0.95, with a mean value of 0.66.

Table 10. Fractional cover values of the classes evaluated in this work. Samples: number of samples where the class was identified. Plots: number of plots where the class was identified. Mean Fc, Max Fc, Min Fc, SD Fc: mean, maximum, minimum and standard deviation of the fractional cover observed for each class. Classes: Acarospora: *Acarospora* spp.; Buellia: *Buellia* spp., Bare Soil: bare soil; Diploschistes: *Diploschistes* spp., Fulgensia: *Fulgensia* spp.; Moss: mosses; Psora: *Psora* spp.; Squamarina: *Squamarina* spp.

Class	Samples	Plots	Mean Fc (%)	Max Fc (%)	Min Fc (%)	SD Fc (%)
Acarospora	37	17	3.8	32.8	0.3	5.8
Bare Soil	54	18	21.6	46.1	5.1	8.1
Buellia	33	13	2.4	13.8	0.5	3
Diploschistes	54	18	14.6	53.1	0.1	11
Fulgensia	53	18	12	25.4	0.7	7.3
Moss	54	8	43.5	76.9	4.9	17
Psora	41	16	1.9	12.6	0.1	2.6
Squamarina	27	13	4.3	4.3	0.3	4.5

3.4. Relationships between Biodiversity and Spectral Diversity

The correlation analysis between spectral diversity (CV and SD_CR) and α-diversity metrics (i.e., species richness, Shannon's Index, Simpson's Index, and Pielou's Index) showed that there were no significant correlations with the dry samples (results not shown). Conversely, positive and statistically significant relationships were found when the samples were wet (Table 11).

Table 11. Slopes, coefficients of determination (r^2) and *p*-values (between brackets) of the linear regression models calculated between spectral diversity metrics (standard deviation of the continuum removal calculated between 550–750 nm ($SD\_CR_{550–750}$) and at 680 nm (SD_CR_{680}); coefficient of variation calculated between 420–900 nm ($CV_{420–900}$), between 550–750 nm ($CV_{550–750}$), and at 680 nm (CV_{680})) and α-diversity metrics (Species richness (S), Shannon's index (H'), Simpson's index (D), and Pielou's Index (J')) when the samples were wet.

α-Diversity Metric	$SD\_CR_{550–750}$	SD_CR_{680}	$CV_{420–900}$	$CV_{550–750}$	CV_{680}
Species richness (S)	0.001	0.003	0.005	0.013	0.08
	-	-	-	-	-
Shannon's Index (H')	0.012	0.022	0.056	0.063	0.071
	0.33(0.001)	0.41(0.0004)	-	-	0.16(0.03)
Simpson's Index (D)	0.02	0.049	0.156	0.164	0.184
	0.39(0.0004)	0.47(0.0001)	-	-	0.26(0.007)
Pielou's Index (J')	0.023	0.041	0.112	0.118	0.141
	0.39(0.0004)	0.42(0.0002)	-	-	0.19(0.02)

When the spectral diversity was calculated as $SD\_CR_{550-750}$ and SD_CR_{680}, the relationships with α-diversity were positive and strongly significant for all the diversity metrics (Table 11). The standard deviation of the CR at 680 nm (SD_CR_{680}), which is related to the difference in chlorophyll content, was the spectral diversity metric better related to α-diversity metrics. Neither the SD_CR nor the CV captured the species richness. The Simpson's index was positively correlated to the CV at all the spectral ranges analyzed (420–900, 550–750, and 680 nm), especially at 680 nm. While Simpson's and Pielou's indices were the metrics that correlated best with SD_CR_{680} ($r^2 = 0.47$ and $r^2 = 0.42$, respectively; Table 11, Fig. 16), they did not show any significant correlation with $CV_{420–900}$ or $CV_{550–750}$. The statistics in cross-validation (Table 12) of the linear regressions presented similar values to the original analysis, showing the stability of the predictions made by the linear regression models between spectral diversity and α-diversity of lichens.

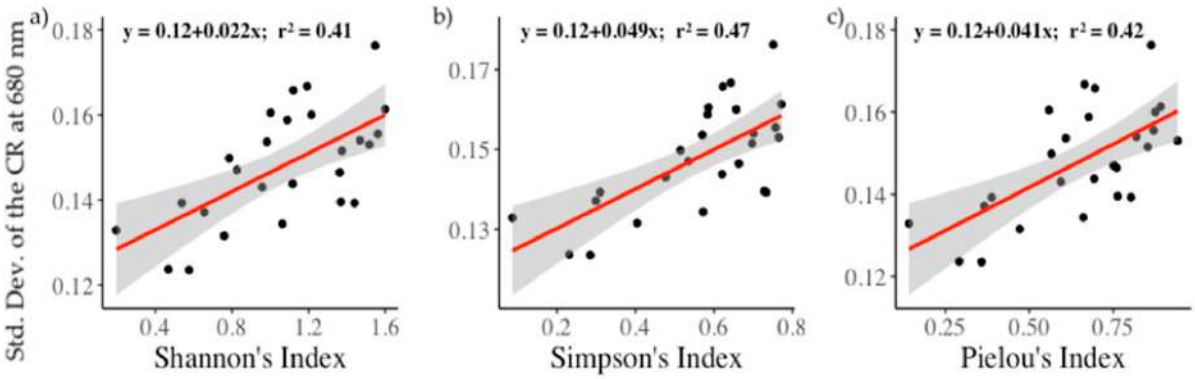

Figure 16. Linear regression between the spectral diversity measured as the Standard Deviation of the Continuum removal at 680 nm and three α-diversity metrics: (**a**) Shannon's index, (**b**) Simpson's index, and (**c**) Pielou's index. Shaded areas represent ±95% symmetrical confidence intervals.

Table 12. Summary of statistics in fitting (r^2 and RMSE) and cross-validation (r^2_{cv} and $RMSE_{cv}$) of the linear regression models between the spectral diversity measured as the standard deviation of the continuum removal at 680 nm and the α-diversity metrics (Shannon's, Simpson's, and Pielou's indices). RMSE: root mean square error; r^2: coefficient of determination.

α-Diversity Metric	r2	RMSE	rCV2	RMSECV
Shannon's index (*H'*)	0.41	0.01	0.32	0.01
Simpson's index (*D*)	0.47	0.009	0.39	0.01
Pielou's index (*J'*)	0.42	0.009	0.35	0.01

4. Discussion

The high accuracies obtained using SVM to classify hyperspectral imagery reinforce their use to differentiate biocrusts (Rodríguez-Caballero et al., 2014). Differences in the reflectance of biocrust constituents are subtle (Fig. 14), but SVMs are capable of differentiating spectrally similar classes when the inputs are spectral signatures (Gualtieri and Cromp, 1998; Watanachaturaporn et al., 2005; Plaza et al., 2009). Even though the accuracy metrics from both sets of images were similar, the classification improved when biocrusts were wet. This result is explained by the enhanced differences that appear in the reflectance spectra when biocrusts are metabolically activated after irrigation (Weber and Hill, 2016). Several studies have characterized the optical properties of biocrust communities in the same optical range used in this study (Rees et al., 2004). However, the spatial scale of these studies only allowed characterization of biocrust communities. Conversely, the fine spatial resolution of the imaging system used in this work allowed to characterize for the first time the pure spectral signature of six lichen genera, to compare their characteristics and to capture the spectral diversity among them. In fact, we used a pixel size lower than the size of each object of interest (i.e., thallus of lichens), as suggested by Ricotta et al. (1999) and Sticker and Southworth, 2008.

Lichens present different structural and biochemical traits, which create wavelength-dependent variations that can be integrated by spectral diversity, as shown in vascular plants by (Schweiger et al., 2018). Different genera of lichens are characterized by particular

biochemical traits that promote spectral variations, so their spectral diversity can be exploited to infer their α-diversity. However, it is important to understand which are the best metrics to represent the relationship between lichen spectral diversity and α-diversity. Since the absorption peak around 680 nm has been widely investigated as a spectral feature of biocrusts and is present in all lichens (e.g., Weber and Hill, 2016; Román et al., 2019; O'Neil, 1994; Karnieli and Sarafis, 1996; Chamizo et al., 2012), we tested if a spectral diversity metric focused on this feature may be suitable for monitoring changes in their composition. We found that using a spectral diversity metric based on this absorption feature (i.e., the SD_CR_{680}) increases the spectral variability determined by the chlorophyll content of different lichens, while removing the confounding influence of other factors such as the structure of lichens. In fact, some lichen genera are characterized by a strong tridimensional component (e.g., *Diploschistes* spp., *Squamarina* spp.) relative to others, which can determine a higher intra-genera variability compared to the inter-genera variability. The normalization of the reflectance spectra to a common baseline through the CR algorithm minimized these structural effects, allowing to capture the spectral variability of lichens determined by the chlorophyll content. Conversely, the CV is influenced by both variations in the content of pigments and the structure of biocrusts, which may hide inter-genera variability. This might be the reason why the CV did not perform as well as expected in previous studies conducted with vascular plants (e.g., Aneece et al., 2017; Wang et al., 2018a,b), where the structural component constitutes were the main source of spectral variability. Conversely, the results obtained in this study highlight the dominant role of the chlorophyll content to determine the differences between lichen genera and the importance of using the absorption feature centered at ~680 nm to capture their spectral diversity. Nevertheless, using absorption features that are found in the shortwave infrared region of the spectra of lichens (Weber and Hill, 2016) might help to improve the results obtained in this study, that investigated only the visible and near infrared spectral domain.

Among the α-diversity metrics tested, the Simpson's index correlated the most with the spectral diversity of lichens. The better performance of the Simpson's index compared to the Shannon's index is in agreement with recent studies conducted in tropical forests (Schäfer et al., 2016) and in a prairie grassland (Wang et al., 2018a). The latter found similar and weaker relationships between spectral diversity and evenness (calculated as Pielou's index) as we did here, although they correlated these metrics with the CV instead of the SD_CR. This might be due to the fact that Shannon's index assumes that all the species are present and randomly sampled (Peet, 1974), and the Simpson's index is more sensitive to dominant or common species, as noted by (Wang et al., 2018), making it more suitable when this is the case. The similar relationships obtained in cross-validation show that these results are reliable despite their sample size.

The imagery used in this study captured with high detail the lichen genera present in our samples, allowing to identify positive and significant relationships between the spectral diversity and the α-diversity of lichens. The methodology proposed in this study should be in principle applied to monitor α-diversity of lichens at wider scales, a key task to understand the shifts in the composition that these communities are undergoing in the actual context of global change (Rodríguez-Caballero et al., 2018; Ferrenber et al., 2015; Maestre et al., 2015; Ladrón de Guevara et al., 2018). However, the upscaling of this methodology may be not trivial due to the decreased spatial and/or spectral resolution when working on wider scales.

Many ecological processes maintain scale-dependent relations (Wang et al., 2018a; Stohlgren et al., 1997; Kalkhan et al., 2007; Kumar et al., 2009) and a sampling scale bigger than the object studied might cause a loss of information that is provided at finer spatial resolutions (Rocchini et al., 2010). In order to understand if the relations found in this work hold with decreasing spatial resolution, the spatial sensitivity of the spectral diversity–biodiversity relationship should be investigated. A previous work in a prairie grassland (Wang et al., 2018) identified a strong scale dependence of the spectral diversity–biodiversity relationships and suggested that the optimal pixel size for distinguishing α-diversity in prairie plots was similar to the size of an individual herbaceous plant (1 mm to 10 cm). This might hamper the monitoring of the α-diversity of lichen-dominated biocrusts at landscape scale with sensors installed on satellite or airborne platforms, which most likely would have a bigger pixel size than the one used in this work.

Conversely, the use of unmanned aerial vehicles (UAVs), which can carry light-weight imaging sensors of different spatial (reaching 2–4 cm/pixel in many cases) and spectral resolutions (Aasen et al., 2018) may allow replicating studies like ours at landscape level (Anderson and Gaston, 2013). Many of these sensors do not have very high spectral resolution, but have at least one band at ~680 nm (Aasen et al., 2018), which would allow to calculate the SD_CR_{680} (the spectral diversity metric that presented the highest predictability of lichens' α-diversity in our study) to monitor α-diversity of lichens at larger spatial scales. Achieving the results shown in this work at landscape scale might also be hampered by the spectral properties that other components (e.g., vascular plants, mosses, bare soil) have on the spectral reflectance measured from remote sensors, which might hinder the separation of the pure spectral component of lichens and to estimate their α-diversity. This issue could be however solved using spectral mixture analysis (Somer et al., 2011), a technique that models a mixed spectrum as a combination of its spectral components weighted by the correspondent subpixel fractional covers (Keshava and Mustard, 2002) and has already proved to be successful for mapping biocrusts (Rodríguez-Caballero et al., 2014).

5. Conclusions

The very high accuracies obtained classifying the hyperspectral images using SVMs showed the reliability of this methodology to identify different biocrust-forming lichens. Therefore, we were able to extract pure spectral signatures of different biocrust constituents and to evaluate the relationships between α-diversity and spectral diversity of lichens. We found that the SD_CR680 nm was the spectral diversity metric that predicted the best α-diversity metrics that include richness and evenness in their calculations (i.e., Pielou's and Simpson's indices). As such, we suggest that this index could help to track spatio-temporal changes in lichen-dominated biocrust communities. In this context, the results of this study will help to improve future works upscaling the methodology here shown to coarser scales in drylands, a key task in any monitoring program aiming to assess the impacts of ongoing climate change and desertification processes in these environments.

Chapter 4

UAV-based RGB, thermal infrared and multispectral imagery to investigate the terrain control on the spatial distribution of dryland biocrusts

J. Blanco-Sacristán, C. Panigada, R. Gentili, G. Tagliabue, R. Garzonio, M.P. Martín, M. Ladrón de Guevara, F. T. Maestre, M. Rossini

Submitted to *Earth Surface Processes and Landforms*

Abstract

Biocrusts, topsoil communities formed by mosses, lichens, liverworts, bacteria, fungi, algae, and cyanobacteria, are a key biotic component of dryland ecosystems. While climate patterns control the distribution of biocrusts in drylands worldwide- terrain and soil attributes can influence biocrust distribution at landscape scale. In the last two decades, unmanned aerial vehicles (UAVs) have been used to study dryland vegetation and terrain. In this work, multi-source UAV-retrieved imagery was used for the first time to map and study biocrusts' ecology in a typical dryland ecosystem in central Spain. RGB imagery was processed, using structure-from-motion (SfM) techniques, to allow for the analysis of terrain attributes related to microclimate and terrain stability and their relationship with soil properties. Thermal infrared (TIR) imagery was used to calculate the apparent thermal inertia (ATI) of soil and relate it to soil moisture. Finally, multispectral imagery was used to produce maps of dryland ecosystem components (i.e. vegetation, bare soils and lichen- and moss-dominated biocrusts). The relationships between soil properties and UAV-derived variables at field plot level were first evaluated. Then, the relationship between biocrusts and terrain attributes was studied at ecosystem level using the RGB- and TIR-derived variables. Lichen-dominated biocrusts were associated with areas with high slopes and low values of ATI, while biocrust-forming mosses dominated lower and moister, north-faced areas, characterised by gentler slopes and higher values of ATI. Notably, we found that elevation is a key terrain attribute in the study area and might control other variables, such as soil properties and solar radiation in areas with complex morphology. This study shows the potential of using UAVs to improve our understanding of drylands and, particularly, to evaluate the control that the terrain has on biocrusts' distribution, which is a key element in any program aiming to evaluate changes in biodiversity and associated ecosystem services in drylands.

1. Introduction

Drylands constitute one of the largest biomes on Earth, covering ~47% of the terrestrial surface (Koutroulis, 2018). In these environments, topography determines the redistribution of scarce precipitation and therefore controls water content and the spatial distributions of soil nutrients and organic matter affected by subsurface flows, runoff and infiltration (e.g., Puigdefábregas and Sánchez, 1996; Aguiar and Sala 1999; Puigdefábregas et al. 1999; Puigdefábregas, 2005; Manzoni et al., 2006). This affects not only vegetation distribution, but

also components that appear in plant interspaces, such as biocrusts communities (Rodríguez-Caballero et al., 2019). Biocrusts are a combination of topsoil communities including mosses, lichens, liverworts, bacteria, fungi, algae and cyanobacteria. They play an important role in nutrient cycling (Elbert et al., 2012; Weber et al., 2015), soil C fluxes (Castillo-Monroy et al., 2011; Tucker et al., 2019), runoff/runon dynamics (Chamizo et al., 2012a; Rodríguez-Caballero et al., 2015; Faist et al., 2017) and are a key component for dryland ecosystems' services maintenance (Rodríguez-Caballero et al., 2017). The effect that these communities have on dryland surfaces depends on the dominant and developmental stage of the crust (Belnap and Lange, 2013; Concostrina-Zubiri et al., 2013; Faist et al., 2017; Tucker et al., 2019). For example, biocrusts can increase water availability for plants by augmenting water retention in topsoil (Eldridge et al., 2020) and reducing soil evaporation (e.g., Chamizo et al., 2016; Adessi et al., 2018). They modify sediment accumulation, carbon and nutrient content (e.g., Chamizo et al., 2017) and affect surface roughness (e.g., Rodríguez-Caballero et al., 2015; Wang et al., 2017). For this reason, evaluating the spatial pattern of different types of biocrust-dominated surfaces is important to understand their role in the ecosystem.

Sensors technology has progressed in the last decades to the point that multi- and hyperspectral imagers that could previously only be flown on expensive airborne platforms, have been miniaturized (Toth and Józków, 2016) and can therefore be carried onboard unmanned aerial vehicles (UAVs) (Aasen et al., 2018). This has allowed researchers to obtain and exploit a wide range of spectral information to better understand dryland functionality, often reaching sub-decimetre spatial resolutions. Previous work has used UAVs to recognize dryland vegetation (e.g., Cunliffe et al., 2016; Sankey et al., 2017; Milling et al., 2018), proving that it is an achievable task. However, remote sensing of biocrusts has traditionally been relegated to other platforms, such as airborne (e.g., Weber et al., 2008; Rodríguez-Caballero et al., 2014) and satellites (e.g. Panigada et al., 2019), with a few exceptions (Jung et al., 2020; Sevgi et al., 2020; Havrilla et al., 2020). In addition, biocrusts are difficult to distinguish due to their small size and similar optical properties to vegetation and soil (Weber and Hill, 2016; Smith et al., 2019). Hence, UAVs integrated with multispectral cameras can greatly benefit the identification of dryland biocrusts.

The research field is starting to explore the potential of RGB imagery acquired from UAVs to identify dryland biocrusts (Jung et al., 2020; Sevgi et al., 2020; Havrilla et al., 2020). However, even though narrow-band multispectral sensors might offer more spectral information from biocrusts than RGB ones (Havrilla et al., 2020), to our knowledge, they have not been used onboard UAVs for biocrust identification in drylands. By applying the continuum removal algorithm (CR; Clark and Roush, 1984) to hyper- or multispectral data, the reflectance spectra of biocrusts can be normalized to a common baseline. Several authors have exploited subtle differences in their absorption features for their identification using this algorithm (e.g. Rodríguez-Caballero et al., 2017; Panigada et al., 2019; Román et al., 2019; Blanco-Sacristán et al., 2019). Multispectral sensors usually have at least one spectral band in the red region at ~ 660-680 nm, that is the chlorophyll-*a* absorption feature, which is present in all chlorophytic biocrusts (Weber and Hill, 2016) and allows comparison between their absorption in this region of the optical spectrum. In this context, the CR has never been applied to multispectral imagery acquired using UAVs to differentiate dryland biocrusts by exploiting differences in common absorption features among chlorophytic biocrusts. This increased

differentiation added to the sub-decimetrical resolution that can be achieved by mounting these sensors onboard UAVs could greatly benefit their identification, particularly when bare soil and biocrusts are mixed.

UAVs have been commonly used to obtain digital surface models (DSM) from RGB imagery, from which digital terrain models (DTMs) of very fine spatial resolutions can be derived to calculate topography-related variables using digital photogrammetry (Westoby et al., 2012). These detailed DTMs allow to apply hydrological models and to study the impact of changing terrain properties on landscape's hydrology (e.g., Lucieer et al., 2014). Thus, using these models it is possible to study components of hydrological systems, such as surface and subsurface flows, which are key to understanding nutrient and sediment transport in the landscape (Stieglitz et al., 2003). However, relationships between soil properties and topography are site-dependent in ecosystems of complex morphologies, where microclimatic conditions are different from the ones observed at wider scales and can favour the formation of a heterogeneous community assembly (Rossi et al., 2014). In this context, and since soil properties greatly control biocrust distribution in drylands (Rodríguez-Caballero et al., 2019), using DTM-derived variables to evaluate the effect of the terrain on dryland soil properties offer a tool of great help for their study. However, not all physical properties of soils can be evaluated through DTMs, and other key variables for biocrust development, such as soil moisture, need additional data sources in order to be estimated.

Soil moisture plays a key role in surface water flow by controlling transport processes in the soil–plant–atmosphere system (Campbell and Norman, 1988). However, the estimation of the soil moisture involves on-site measurements by standard point-based techniques (e.g., the thermogravimetric method or time domain reflectometry) and requires interpolation techniques in order to obtain spatially explicit information. Soil thermal conductivity changes with fluctuations on moisture level (Minacapilli et al., 2009), therefore, thermal inertia can be used to estimate soil moisture. Materials with high thermal inertia have more uniform surface temperatures throughout the day and night than materials with low thermal inertia. Since thermal inertia cannot be estimated using remote sensing, apparent thermal inertia (ATI) is used instead to be related with soil moisture as proved by Van doninck et al., (2011) in arid and semi-arid environments. Maps of ATI can be obtained using multitemporal thermal infrared (TIR) imagery to estimate the diurnal temperature cycle. The co-albedo needed for this calculation can be derived from multispectral visible-near infrared (VIS-NIR) data. However, the coupling between ATI and soil moisture is not straight forward in heterogeneous surfaces, as in drylands, since ATI might be directly related to soil moisture only in areas where only a single soil or land cover type is present (van Doninck et al., 2011). For this reason, using TIR cameras on board UAVs would allow the derivation of high spatial resolution maps of ATI, which might solve this problem of mixed surfaces.

The objective of this work was to evaluate the effect of terrain attributes in the distribution of dryland ecosystem components' using UAV-based imagery by i) mapping dryland constituents (i.e. vegetation, biocrusts, and bare soil) through multispectral imagery; ii) estimating terrain attributes from Structure from Motion (SfM) techniques applied to RGB imagery and evaluating their effects on soil properties; iii) estimating soil moisture using maps of ATI derived from TIR imagery; iv) evaluating through a multivariate statistical approach how terrain attributes and soil moisture affect biocrust distribution in the study area.

2. Materials and Methods

2.1. Study area

This study was conducted in a typical dryland ecosystem in Aranjuez, Spain (Fig. 17). The climate in this area is semiarid Mediterranean, with mean values of annual temperature and rainfall of 15ºC and 349 mm, respectively. The soil is classified as Gypsiric Leptosol (IUSS Working Group WRB, 2006). The vascular vegetation cover in this area is <40% and is dominated by *Macrocloa tenacissima* tussocks and, in a lesser amount, small shrubs, such as *Helianthemum squamatum* and *Gypsophila struthium*. On the surface not covered by vascular vegetation, a rich biocrust community develops, dominated by lichens, including *Diploschistes diacapsis, Squamarina lentigera* and *Psora decipiens* among others. A moss-dominated crust also develops, with species such as *Pleurochaete squarrosa* and *Tortula revolvens.* Cyanobacteria genera, such as *Microcoleus, Tolypothrix* and *Nostoc* can also be found in the area (Cano-Díaz et al., 2018). See Maestre et al. (2013) for a complete list of species of the visible biocrusts in the study area. We worked in two different areas within the study site: Area A, which covers an extension of 5.4 hectares, has a moderate slope a dominant West exposure in Zone 1 and a smaller slope exposed to the East in Zone 2; and Area B, which covers 1.2 hectares and presents an abrupt hill, mainly exposed to the South in Zone 3, and a minor slope exposed to the North in Zone 4.

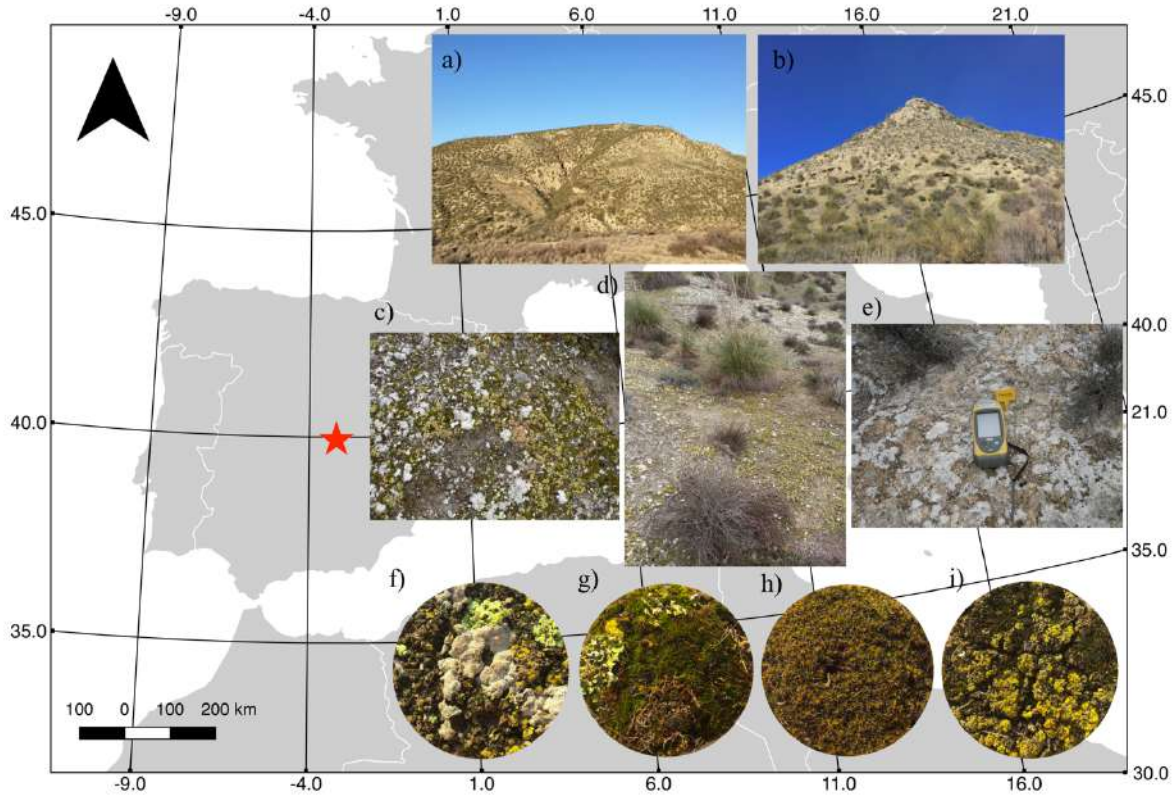

Figure 17. Location of the study area in Aranjuez, central Spain. a) Area A of this study; b) Area B of this study; c-e) Communities of biocrust found in the study area; f-i) detailed view of the dominant biocrust surface covers.

2.2. Field campaign

In March, 2018, a field campaign took place to characterise biocrust and vascular vegetation covers, soils and to collect RGB, multispectral and TIR UAV-based imagery. We collected soil samples to measure the physical properties of the soil in the study area, as described in section 2.2.1. The RGB imagery was collected to create DTMs that could allow to derive terrain attributes that are related with the soil attributes previously studied, as described in section 2.3.1. Multispectral imagery was collected to map the study area, as described in section 2.3.2. Finally, the TIR imagery was collected to evaluate soil moisture, as described in section 2.3.3. A general workflow with the main actions of this work is represented in Fig. 18.

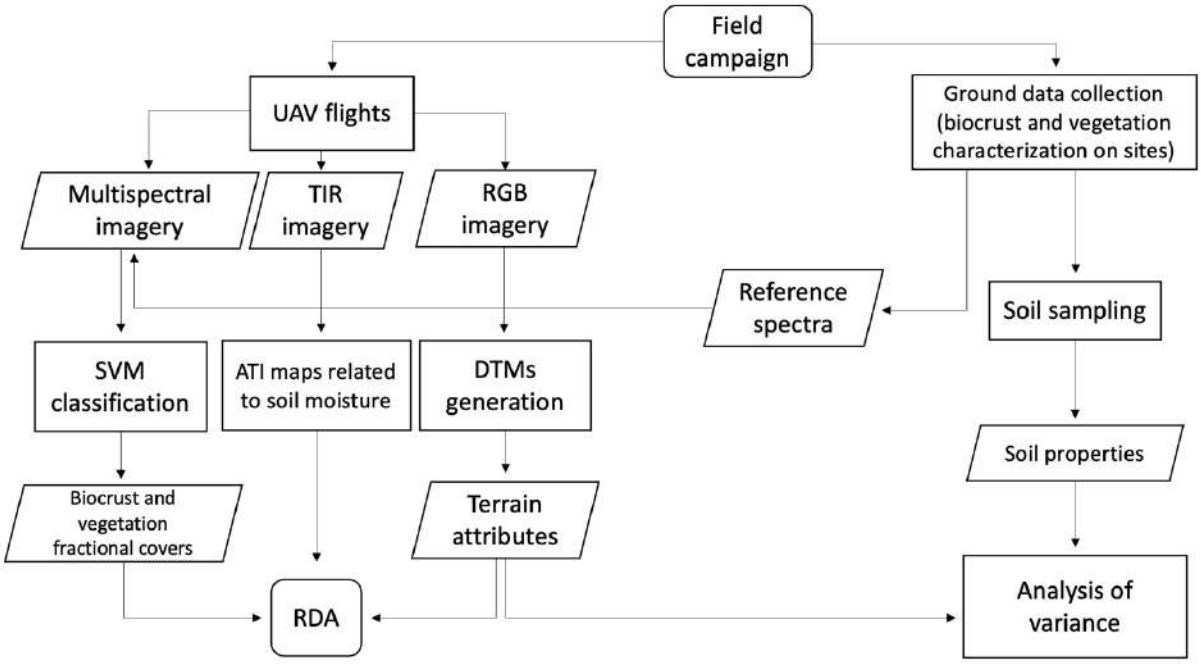

Figure 18. Workflow with the main processes carried out in this work. UAV: unmanned aerial vehicle; TIR: thermal infrared; RGB: red, green and blue; SVM: support vector machine; ATI: apparent thermal inertia; DTM: digital terrain model; RDA: redundancy analysis.

2.2.1. Biocrust characterization and soil sampling

Soil samples were collected in the field on the 21st of March, 2018. A total of 23 2x2 m plots were placed within the two areas to capture the variations in biocrust communities and vascular vegetation that were identified by an expert. Pictures were also taken with a camera mounted on a tripod at 1 m height. Three representative soil sub-samples were taken in each plot from 0-10 cm depth (after removing the litter layer) and pooled to one sample, which represented the average soil characteristics of the plot. The samples were chemically and physically analysed in the laboratory applying standard techniques (Colombo and Miano, 2015). The samples were dried and sieved (2 mm mesh) and analysed to determine the percentage of soluble salts (SolSal), total phosphorus (P_{tot}), percentage of organic carbon (OrgCarb) and total nitrogen (N_{tot}). Soil moisture was measured in the field at 0-10 cm depth

at three representative locations within each plot using a FieldScout TDR-100 soil moisture meter (Spectrum Technologies, USA).

2.2.2. UAV flights

Three photogrammetric flights (Table 13) using an eBee SQ (senseFly, Switzerland) fixed-wing UAV were conducted by the company 3D Scanner (Zaragoza, Spain), on March 20th, 2018. These flights were conducted in winter, which corresponds to the wet season in the study area, because biocrusts are more colourful when are well hydrated by the rains, and therefore they are easier to map and differentiate from spectral information. Three different spectral cameras: SODA (senseFly, Switzerland), Parrot Sequoia (senseFly, Switzerland) and thermoMAP (senseFly, Switzerland) were flown to acquire RGB, multispectral and TIR images respectively. Two sets of TIR imagery were acquired: the first before sunrise, and the second at noon. During this second flight, multispectral imagery was simultaneously acquired. A third flight, right after the previous one, was performed to acquire RGB images on the site.

An overlap of 80% between the RGB images was planned during the third flight, and an overlap of 70% between the multispectral images was achieved during the second flight. The multispectral Parrot Sequoia camera is a compact bundle of 4 cameras with complementary metal-oxide-semiconductor sensors, each one equipped with an individual narrow-band filter (Assmann *et al*., 2018). This results in a multi-band image composed by four bands: Green (550 ±40 nm), Red (660 ± 40 nm), Red Edge (735 ± 10 nm) and NIR (790 ± 10 nm). A white reference Micasense® panel was measured with the Sequoia camera immediately before and directly after the drone survey in order to calibrate the images.

Table 13. Technical information of the UAV flights using thermoMAP Parrot Sequoia Parrot and S.O.D.A. sensors.

Flight	Sensor	Start time (UTC)	Duration (min)	Average flight altitude (m. a. s. l.)	Spatial resolution (cm/pixel)
1	thermoMAP	06:15	30	620	10.3
2	Sequoia	12:00	25	635	5.8
3	thermoMAP	12:30	30	620	10.3
4	S.O.D.A.	13:15	18	675	0.5

2.2.3. Ground data

Reflectance factors were obtained in the field in order to calibrate and validate spectral data acquired from the UAV sensors using an ASD FieldSpec® FR3 field spectroradiometer (Analytical Spectral Devices, USA) which features a spectral range from 350 nm to 2500 nm, optical resolution of 1 nm and a nominal field of view of 25º. Two types of reference targets were measured during the flight campaign: white and black 2 x 2 m targets made of PVC-coated canvas material (Odyssey' trademark material; Kayospruce Ltd., UK) assumed to be lambertian surfaces; and selected homogeneous plots from the main communities of biocrusts in the study site (Fig. 17). Before each target measurement, down-welling radiance was measured on a calibrated 99% reflective Spectralon® panel (Labsphere Inc., USA) to optimize

the instrument parameters and calculate reflectance factors. Eight to ten spectra were taken on each target and were averaged to obtain the final spectrum for each. These ground spectral measurements were acquired around solar noon, contemporaneously to the multispectral images by the Parrot Sequoia camera (drone flight 2). Their exact location was registered using a Topcon GPR-1 (Topcon, Japan) differential global navigation satellite system (dGNSS) so the ground targets could be accurately located in the UAV images. The spectra of all ground measurements were resampled to the Sequoia spectral resolution using the response function of the sensor (Fawcett et al., 2019). These spectra were used to apply an empirical line correction (Conel et al., 1987) to the multispectral images in order to guarantee radiometric quality in the final reflectance orthomosaics.

Simultaneously with the drone flights, the coordinates of 10 reference targets were taken in each area by means of dGNSS geodetic receivers (one Topcon HiPer Pro antennas and one Topcon GPR-1 [Topcon, Japan]). The targets were deployed in clear areas as black and white grids printed on thick paper sheets (297 x 420 mm). In each area, six of these targets were used as Ground Control Points (GCPs) for the generation of the orthophoto and Digital terrain model (DTM), while the remaining 4 were used as Ground Validation Points (GVPs) for validation. We used a rapid-static measurement technique and the coordinates were corrected during post-processing (Hofmann-Wellenhof et al., 2007). One of the two GNSS devices was used as master and the other as rover. The master station was placed in a clear flat area for a cumulative time of 5 hours and was used as a static reference point. The rover was used to measure the centre point of each GCP and GVP keeping it over the point for at least 2 minutes, taking a measurement every second with at least 6 satellites in the field of view of the receiver, according to the protocol proposed by Hegarty and Chatre (2008). The master and rover data were post-processed using Topcon Tools software (Topcon Positioning Systems, Inc.). The dGNSS system used during the surveys has a horizontal precision of 3 mm + 0.5 ppm and a vertical precision of 5 mm + 0.5 ppm according to the Topcon HiPer Pro specification data.

2.3. UAV data processing

2.3.1. RGB images: Orthophoto, DTM and terrain attributes

RGB images acquired over areas A and B of the study site by the S.O.D.A. camera were processed into orthophotos and grid-based DSMs following a SfM workflow (Lucieer et al., 2014; Westoby et al., 2012) in *Agisoft Photoscan* v. 1.4 (Agisoft, Russia). A detailed description of the SfM algorithms used in *Agisoft PhotoScan* can be found in Verhoeven (2011). The images captured during the flights were aligned using an image feature recognition algorithm similar to Lowe's (2004) scale invariant feature transform method, which automatically detects and matches unique image feature characteristics that are stable under variations in view perspective and illumination across input photographs. This alignment results in a sparse 3D point cloud, which is used to create a dense point cloud by an iterative bundle adjustment algorithm, which recreates its 3D geometry and camera positions from a sequence of two-dimensional images acquired from multiple viewpoints (Ullman, 1979). The onboard navigation sensors allowed the camera positions and 3D point cloud to be

automatically georeferenced within the precision of the instrument. The GCPs were then manually identified on the images, and their dGNSS coordinates were imported to optimize spatial accuracy and improve the geometry of the 3D point cloud. To increase the density of the point cloud and to convert them into the orthomosaics of each area, a multi-view stereo image matching algorithm was applied to the point clouds. The GVPs were also identified in the images and they were used for model accuracy assessment.

To generate free-of-vegetation DTMs, points belonging to vegetation were removed from the point cloud (Fig. 19) using the CANUPO plug-in (Brodu and Lague, 2012) in CloudCompare. For each area, two point clouds representing each class (vegetation and bare soil) were manually segmented from the point cloud. These sub-clouds were used for training the classifier computing a dimensionality descriptor on the original point cloud with a regular ramp of scale values (sampled from 0.1 to 1 with steps of 0.1). The classifier was applied to the point cloud (using selected points as core points) classifying and removing vegetation points. Finally, isolated points were removed by using the noise filter tool (specifying a radius of 0.3 m and a relative error) and the DTMs were exported from CloudCompare with a resolution of 10 cm, interpolating empty cells with average values. To minimize potential errors in the DTMs' values, they were smoothed in ArcMap by applying an average filter with the Focal statistics tool by considering a circle window of 1 m.

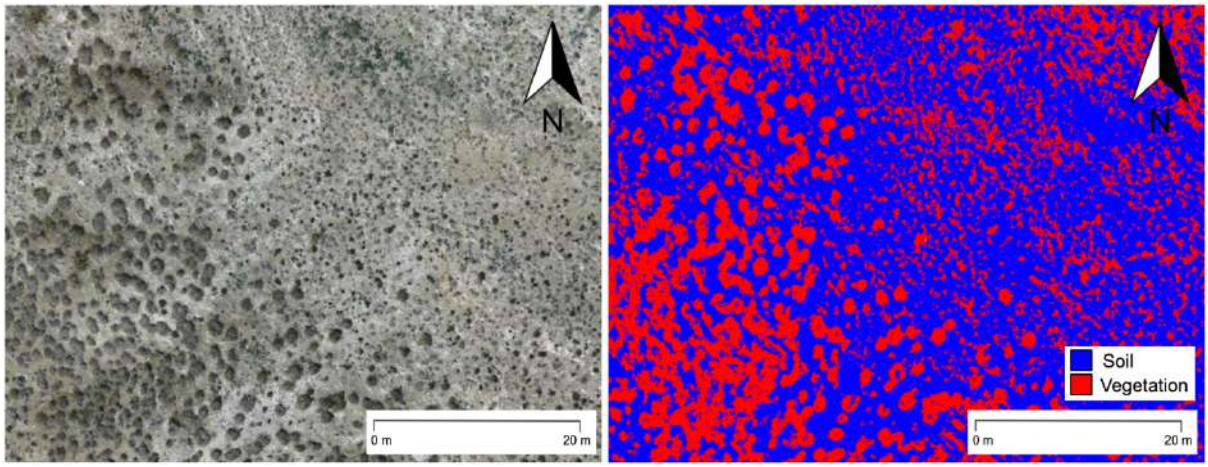

Figure 19. Example of vegetation classification derived from the point cloud used to derive the vegetation-free DTM in Area A of the study site. Left: RGB natural colour composite with vegetation and bare soil areas. Right: Classification of vegetation (red) and bare soil (blue).

Several terrain attributes were calculated from the DTM of each area. The Elevation was extracted from the DTMs. The Slope of each cell was calculated applying the 9 parameters second order polynomial method (Zevenbergen and Thorne, 1987) within the *Slope* function in QGIS v. 2.18.12. The Aspect was derived from the DTM using the *Aspect* function in QGIS v. 2.18. The Northernness (i.e. the exposure of each cell of the DTM to the North) was calculated as the cosine of each cell of the Aspect model. Since this variable has values ranging from -1 to 1, to avoid problems in later calculations, +1 was added to each pixel value.

The Contributing catchment area (CCA) of each pixel of the DTMs was modelled using the TauDEM toolbox (Tarboton, 1997; Tesfa et al., 2011) in ArcMap v. 10.5. For this, the pits were first removed from the DTM and the *D-Infinity Contributing Area* function was used to

calculate it. The D-Infinity algorithm (Tarboton, 1997) calculates the flow direction using the steepest downwards slope on the eight triangular facets formed in a 3 x 3 pixel window centred on the grid cell of interest. The topographic wetness index (TWI; Beven and Kirkby, 1979), which quantifies the topographic control on hydrological processes, was calculated for each cell using Equation 1,

$$TWI = ln\left(\frac{A}{tan\beta}\right) \quad \text{Eq. 1}$$

where A is the upstream area for each pixel and β is the slope in degrees.

The length slope factor (LSF; Renard et al., 1977), indicator of the potential sediment transport or erosion risk under specific slope conditions, was calculated following Equation 2,

$$LSF = (n+1) * \left(\frac{A}{22.13}\right)^{n} * \left(\frac{sin\beta}{0.0896}\right)^{m} \quad \text{Eq. 2}$$

where LSF is the length slope factor, A the CCA, β the slope gradient and n and m are constant parameters fitted to 0.4 and 1.3 respectively.

The potential incoming solar radiation (PSIR) was calculated using the DTM of each area and the geometric solar radiation model implemented in ArcGIS Solar Analyst tool by assuming a uniform clear sky condition with a constant transmissivity of 0.5 (Fu and Rich, 2003) and a diffuse radiation proportion of 0.3. The map of the whole year PSIR [Wh m^{-2} $year^{-1}$] was used in this study as indicator of the potential evapotranspiration (Monteith and Szeicz, 1962).

2.3.2. Multispectral Parrot Sequoia images

The images were processed in Pix4DMapper (Pix4D S.A., Switzerland). The workflow implemented in this software follows the next steps to obtain the final reflectance for each spectral band of the image. First, the calibration coefficient K for converting measured pseudo-radiance R to reflectance is derived for each band as

$$K = \frac{\rho ref}{Rref} \quad \text{Eq. 3}$$

where ρ_{ref} is the known reflectance of the panel for the Sequoia band and R_{ref} represents the measured pseudo-radiance averaged over the imaged pixels of the reference panel. Values for ρ_{ref} are provided by the manufacturer if MicaSense® reflectance panels are used. The digital number (P) of each pixel can be converted to pseudo-radiance in arbitrary units R according to Equation (4).

$$R = f^2 \frac{P-B}{A\gamma\varepsilon+C} \quad \text{Eq.4}$$

where γ is the ISO number, ε is the exposure time in seconds, f is the f-number and A, B and C are camera-specific calibration coefficients which model the non-linear behaviour of the sensor (Fawcett et al., 2020).

Finally, the reflectance per pixel (ρ) of the scene can then be derived as

$$\rho = KR \quad \text{Eq. 5}$$

To correct the reflectances measured by the multispectral sensor, the empirical line method (Smith and Milton, 1990) was applied. This method is based on an empirical relationship between the drone reflectance and ground reflectance of the reference targets (i.e. black and white reference panels) collected with an ASD Field Spectrometer in the field.

The white panel saturated on the Sequoia images, therefore homogeneous biocrust targets were used as bright targets instead. The linear equation obtained for each multispectral band was applied to obtain the final reflectance of the multispectral images.

The spatial accuracy of these multispectral orthomosaics was assessed based on the residuals of the GCPs and the GVPs used for their generation. The final multispectral orthomosaics had a spatial resolution of 7.7 cm/pixel.

The CR algorithm was computed on the reflectance of the final multispectral images. The CR algorithm normalises the reflectance spectrum to a common baseline at certain wavelengths and allows the comparability of absorption features in the spectra that are produced by pigments. This is achieved by approximating the continuum between local spectral maxima through straight-line segments: a value of 1 is assigned to the local maxima, and a value between 0 and 1 is obtained in correspondence of the absorption features. The absorption feature related to chlorophyll-*a* was computed at 660 nm by extracting the value of the CR in the red band (CR_{red}). The CR_{red} was used to improve later classification of the images.

Seven different surface covers were identified in the study site during field surveys (Fig. 20): bare soil (Soil), bright lichens (BL; patches of *Squamarina* spp., *Diploschistes* spp., *Buellia* spp.), bright lichens with moss (BLM; *Squamarina* spp., *Diploschistes* spp., *Buellia* spp. and *Tortula revolve*ns (Zone 1) or *Syntrichia ruralis* (Zone 2)), moss (Moss; *Tortula revolvens* (Zone 1) and *Syntrichia ruralis* (Zone 2)), *Fulgensia* spp. and moss (Fulg; *Fulgensia* spp. and *Tortula revolvens* (Zone 3) or *Pleurochaete squarrosa* (Zone 4)), green vegetation (GreenVeg; green tussocks of *Macrocloa tenacissima*) and dry vegetation (DryVeg; dry individuals of *Helianthemum squamatum*, *Gypsophila struthium* and *Macrocloa tenacissima*). Those surface covers were used as reference for the digital classification of the multispectral orthomosaic.

At least 15 polygons (around 100 pixels) per class were selected on each orthomosaic to train the support vector machine (SVM) algorithm used in the classification. These training areas were selected using ancillary information such as field notes and high resolution RGB orthomosaics. The four bands of the multispectral images were used as input in the SVM.

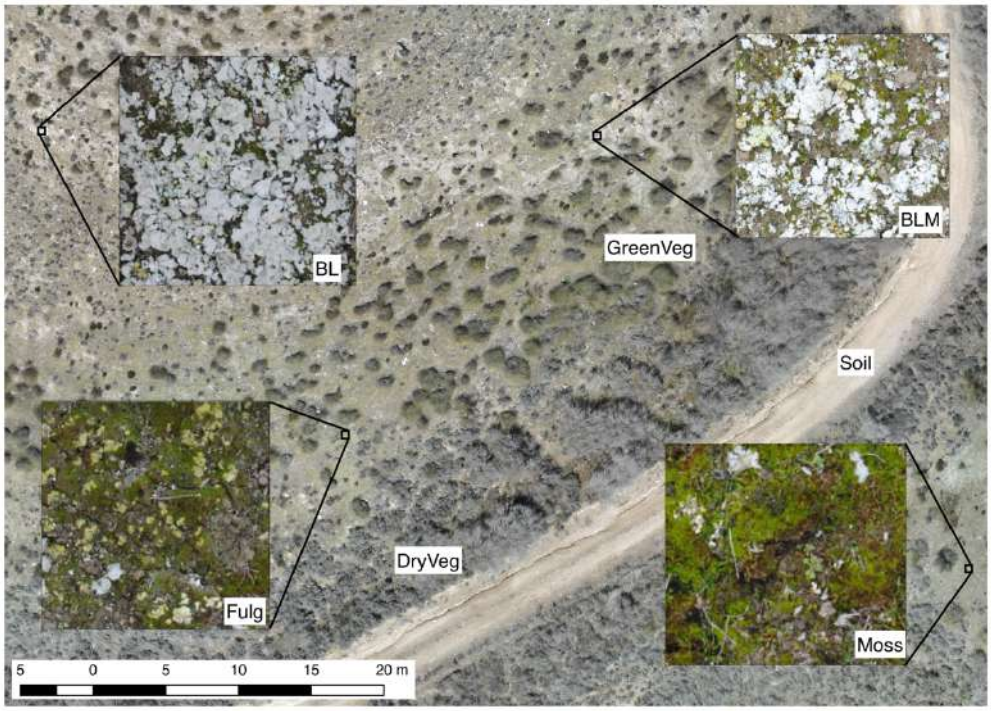

Figure 20. Orthomosaic of Area B of the study zone and details of the classes used to classify the multispectral images. BL: bright lichens; BLM: bright lichens and moss; Fulg: *Fulgensia* spp. and moss; GreenVeg: green vegetation; DryVeg: dry vegetation.

The SVM is a statistical learning theory-based supervised classification method (Cores and Vapnik, 1995; Vapnik, 2005). It uses training samples of the target categories and separates them using a decision surface called hyperplane, which maximizes the margins between them. The support vectors are the closest training samples to this hyperplane, and are the ones used by the algorithm. SVM allows a certain degree of misclassification by using a penalty parameter. However, to avoid overfitting of the model, fine tuning of this parameter is important, since increasing its value increases the cost of misclassifying points, forcing the creation of a more accurate but not generalizable model. In this work, a radial basis kernel function was used, which is controlled by two parameters: the penalty parameter (C) and the width of the Gaussian kernel (c). Large values of C reduce the training dataset error but can result in overfitting of the model to the training data. The best parameters used for each classification were evaluated using the LIBVSM library (Chang and Lin, 2011). The SVM was used in a pairwise classification way to classify the images and derive thematic maps with the spatial distribution of the main surface covers in the two areas. CR_{red} was used to improve the discrimination of some categories with similar spectral behaviour such as DryVeg and Moss, but different pigment absorption.

Classification accuracy was assessed through confusion matrices (Story and Congalton, 1986). In these confusion matrices the ground truth data (the columns) are compared to the classified data (the rows). The major diagonal represents the agreement between these two data sets, and the overall accuracy (OA) of the classification is calculated by dividing the sum of the entries of this diagonal by the total number of samples taken. The validation dataset was

created by selecting independent 50 pixels per class of pure endmembers in the same way as for the training dataset.

2.3.3. Thermal imagery and ATI calculation

TIR images acquired by the thermoMAP camera were calibrated during the flight using an integrated shutter for in-flight radiometric calibration. This shutter automatically closes after every picture is captured and self-calibrates by comparing the grey level of each photo with the temperature measured by the built-in temperature sensor of the camera. Raw images were converted using Pix4D software (Pix4D, Switzerland) to temperature in degrees Celsius with the equation

$$T = 0.01\ R - 100 \quad \text{Eq. 6}$$

where T is the absolute temperature in degrees Celsius and R is the radiometric value of thermoMap thermal images. Emissivity of biocrusts and typical soils was measured in the laboratory and found to be close to 1 for both targets (see Supplementary Material) in the range of the thermoMAP (8.5–13.5 μm). Since the aim of using these images in this study was to measure properties related to biocrusts, emissivity was neglected and thus not included in this calculation.

Two orthomosaics (one captured before sunrise and one at noon) of each target area with a spatial resolution of 15 cm/pixel were generated using Pix4D (Pix4D, Switzerland). The accuracy of these TIR orthomosaics was assessed based on the residuals of the GCPs and the GVPs used for their generation and for accuracy assessment respectively.

Thermal inertia of a certain material describes its resistance to temperature variations (Short and Stuart, 1982). In this work, land surface temperature differences and albedo were used in the definition of the concept of thermal inertia to assess the space–time variability of soil water content (Verstraeten et al., 2006). A simple formulation of thermal inertia is the apparent thermal inertia (ATI; K^{-1}), which is derived directly from multi-spectral remote sensing imagery (Price, 1985; Mitra 2004; Van doninck et al, 2011):

$$ATI = C\frac{1-\alpha}{\Delta T} \quad \text{Eq. 7}$$

where ATI is the amplitude of the diurnal temperature range [K] calculated as the difference between the maximum and the minimum daily surface temperature; α is the surface spectral albedo [-]; and C is the solar correction factor [-] that changes over space and time to normalize for solar flux variations with latitude and solar declination changes between seasons. In this study, ATI is calculated as the difference between the temperature orthomosaic captured at noon and the one captured before sunrise. C was calculated to have a value of 1.19. We approximated the albedo by using the brightness calculated as the arithmetic mean from multispectral orthophotos:

$$\alpha = \frac{\rho GREEN + \rho RED + \rho REG + \rho NIR}{4} \quad \text{Eq. 8}$$

where $\rho GREEN$, ρRED, ρREG and ρNIR are the corresponding Green, Red, Red Edge and NIR bands, respectively. Multispectral bands were calibrated so the brightness map can reasonably be considered to be a proxy of the broadband visible albedo.

The correlation between ATI and soil moisture was tested through a linear regression model between the mean ATI value extracted from these orthomosaics and the mean soil moisture measured during the field campaign on each plot. The average value of ATI on each 2x2 m plot was obtained in QGIS v. 2.18.12, by averaging the ATI values of the corresponding polygons excluding from the calculation the vegetation pixels. A vegetation-free mask was created for this purpose by using the classifications of the multispectral images and was applied to the ATI orthomosaics.

2.4. Statistical analysis

To evaluate if there were statistically significant differences between the four zones of study, a post-hoc Duncan test following a one-way ANOVA analysis was performed. To analyse the effect of the terrain attributes in relation to the spatial distribution of soil properties measured in the sampling plots, the correlation ratio (Pearson, 1926) was calculated between the terrain attributes calculated from the RGB images and the ATI and the soil characteristics retrieved from ground measurements. The average value of the terrain attributes on each plot was obtained in QGIS v. 2.18.12, by averaging the terrain attribute values of the corresponding polygons, excluding from the calculation the vegetation pixels. The correlation ratio can assume values in the range 0-1, with values close to 1 meaning that the terrain attribute variable explains all the data variance, is calculated as:

$$\eta^2 = \frac{\sigma_{\underline{y}}^2}{\sigma_y^2}, \text{ where } \sigma_{\underline{y}}^2 = \frac{\sum_x n_x (\underline{y}_x - \underline{y})^2}{\sum_x n_x} \text{ and } \sigma_y^2 = \frac{\sum_{x,i} n_x (y_{xi} - \underline{y})^2}{n} \quad \text{Eq. 9}$$

where each observation is y_{xi}, x indicates the terrain attributes (divided in three classes standardizing the values, using maximum and minimum values of each variable), and i indicates an observation. If n_x is the number of observations in the x topography variable, $\underline{y}_x$ is the mean of the category x and $\underline{y}$ is the mean of the whole population.

The relationship between the different biocrust covers and the terrain variables in the whole study area was evaluated through a redundancy analysis (RDA) performed using the *vegan* R package (Oksanen et al., 2017) version 2.4. To test the significance of the selected variables in the RDA, permutation tests (N=999) were performed using the marginal effect of the terms in the *anova.cca* function.

The CCA variable was removed from the analysis to avoid multicollinearity, since it was used to calculate TWI and LSF. Based on this, a set of 7 terrain attributes were considered in the analysis: PSIR as an indicator of the potential evapotranspiration (Monteith and Szeicz, 1962) and as a proxy of thermal microclimate (Durham et al., 2018; Suggitt et al., 2018); LSF as an index of surface stability (Renard et al., 1977); TWI as an index of the topographic control on hydrological processes (Sörensen et al., 2006); Elevation; Slope gradient, as it has implications for dryland components distribution not captured by other variables (Rodríguez-Caballero et al., 2019); Northernness, as indicator of facing of the slope; and ATI, as proxy of soil moisture. The vegetation (combination of DryVeg and GreenVeg) and soil fractional covers were also included as variables in this analysis. The dataset used in this analysis was obtained through a random sampling in the study area, where 540 points were selected. A buffer of 3 m was used to summarize the terrain attributes and the fractional cover of each point. To

avoid spatial auto-correlation (Haining, 1980) in the random sampling, in both study areas a semi-variograms' analysis was performed on the first principal component of the principal component analysis (PCA) of the multispectral images, which captures most information in the original multispectral bands (Tian et al., 2005).

3. Results

3.1. Image pre-processing: radiometric and geometric accuracy

A summary of the geometric accuracy is shown in Table 14. For the RGB orthomosaics, the total RMSE was lower than 10 pixels in both models. For the multispectral images, the total RMSE was lower than 4 pixels in both images. For the TIR orthomosaics, the total RMSE was lower than 3 pixels.

Table 14. Root mean square error (RMSE) for the 6 Ground Control Points (GCPs) and 4 Ground Validation Points (GVPs) for RGB, multispectral and thermal surveys.

Area	Imagery	GCP RMSE XY cm (pixel)	GCP RMSE Z cm (pixel)	GCP Total RMSE cm (pixel)	GVP RMSE XY cm (pixel)	GVP RMSE Z cm (pixel)	GVP Total RMSE cm (pixel)
Area A	RGB	2.17 (4.3)	4.2 (8.4)	4.7 (9.4)	2.2 (4.4)	2.3 (4.6)	3.2 (6.4)
Area B		1.58 (3.1)	1.3 (2.6)	2.1 (4.2)	1.9 (3.8)	1.3 (2.6)	2.4 (4.8)
Area A	Multispectral	18.8 (3.2)	21.8 (3.7)	22.4 (3.8)	19.4 (3.3)	13.7 (2.3)	21.8 (3.7)
Area B		11.1 (1.9)	17.1 (2.9)	18.2 (3.1)	13.7 (2.3)	21.44 (3.7)	22.3 (3.8)
Area A	TIR	21.2 (2.1)	23.4 (2.2)	24.7 (2.4)	23.1 (2.2)	22.4 (2.1)	24.5 (2.3)
Area B		16.6 (1.6)	17.3 (1.6)	19.8 (1.9)	16.8 (1.6)	15.9 (1.5)	19.9 (1.9)

3.2. Classification of the multispectral orthomosaics and evaluation of the classification accuracy

SVM classification generated land cover maps of the two target areas in the study site (Fig. 21). OAs higher than 90% where achieved in both areas. As shown in the confusion matrices (Table 15), BL and GreenVeg were the most accurately classified covers in this area, but there was some confusion between BLM and Moss, where 10% of Moss was misclassified as BLM. All classes were correctly classified in Area B, with an OA of 93%. However, there was some confusion between Moss and DryVeg, with 14% of Moss classified as DryVeg. In both areas, the most dominant class was DryVeg, while the least ones were the classes with lichens and mosses mixed (i.e. BLM and Fulg in Area A and Area B, respectively; Table 16).

Table 15. Confusion matrices of the classification of both areas of study. Top: confusion matrix of Area A. Bottom: confusion matrix of Area B. BL: bright lichens; BLM: bright lichens and moss; Fulg: *Fulgensia* spp. and moss; GreenVeg: green vegetation; DryVeg: dry vegetation.

		Field data (%)					
		Soil	DryVeg	GreenVeg	BL	BLM	Moss
Classified data (%)	Soil	94	0	0	4	6	0
	DryVeg	0	98	4	0	0	4
	GreenVeg	0	2	96	0	0	0
	BL	4	0	0	96	2	0
	BLM	0	0	0	0	82	6
	Moss	2	0	0	0	10	90

		Field data (%)					
		Soil	DryVeg	GreenVeg	BL	Fulg	Moss
Classified data (%)	Soil	96	0	0	6	0	0
	DryVeg	0	98	0	0	4	14
	GreenVeg	0	2	100	0	0	0
	BL	0	0	0	94	0	0
	Fulg	4	0	0	0	94	6
	Moss	0	0	0	0	2	80

Table 16. Fractional cover of each class in the study areas as resulted from the classification of the multispectral images. -: class not present.

	Surface cover (%)						
	Soil	DryVeg	GreenVeg	BL	BLM	Fulg	Moss
Area A	4.01	59.88	10.23	1.32	10.21	-	14.32
Area B	8.94	43.11	8.03	0.86	-	14.84	24.19

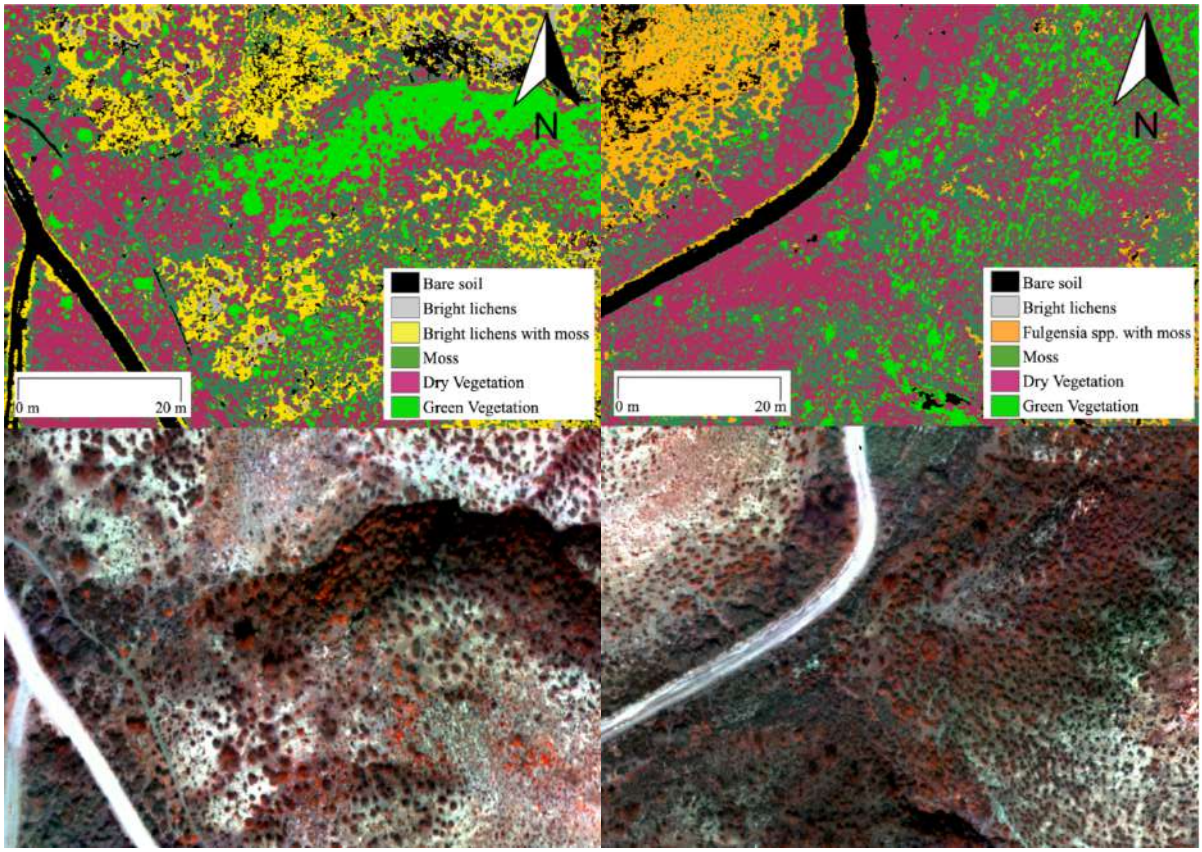

Figure 21. Details of the support vector machine classifications (top) of the multispectral images (bottom), represented as false-colour composite (bands NIR, Green and Red). Left: area A; right: area B.

The reflectances (Fig. 22b) of biocrust classes in the overall brightness and in the red edge region, i.e. the region of rapid change in reflectance between red absorption due to pigment content and near infrared reflectance due to the structure, were the highest among the evaluated. Classes dominated by lichens had higher reflectances, and BL was the class with the highest reflectance among them. Classes dominated by mosses had the lowest reflectances among biocrusts, and only vegetation reflectances were lower. The application of the continuum removal algorithm (Fig. 22a) highlighted the absorption due to chlorophyll at ~660 nm. Moss was the biocrust class with the highest absorption at ~660 nm due to chlorophyll (i.e. lowest CR_{red} value), while GreenVeg was the class showing the highest absorption of all the evaluated classes. While similar in the spectral shape, DryVeg and Moss presented differences in their CR_{red} and reflectance values. This absorption feature was present in all classes but Soil, and allowed to better differentiate it from biocrust classes. Pixels classified as DryVeg with values of CR_{red} greater than 0.75 were assigned to Moss and pixels of BL with values of CR_{red} of 1 were assigned to Soil. These subtle differences allowed to improve the classification done by the SVM, which slightly confused these two classes, by using thresholds in the CR_{red}. Final accuracies (Table 15) are the result of using these thresholds after the SVM classifications.

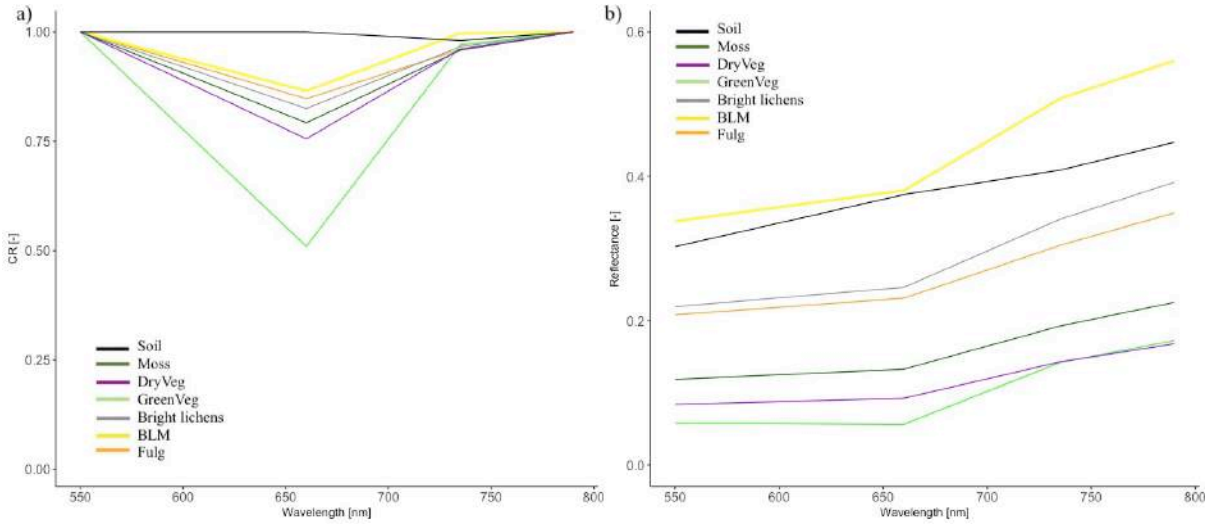

Figure 22. Mean continuum removal absorption spectra (a) and mean reflectance spectra (b) of the vegetation, biocrust and soil classes used in this work, extracted from the Sequoia multispectral images. Shaded area is the standard deviation of each spectra. DryVeg: dry vegetation; GreenVeg: green vegetation; BLM: bright lichens with moss; Fulg: *Fulgensia* spp. with moss.

3.3. Thermal data and soil moisture

ATI was calculated from the TIR imagery captured, and maps of ATI were created, masking the vegetation component. The soil moisture that was measured in the 23 field plots correlated well with the ATI values (r^2=0.83; Fig. 23), indicating that ATI is a good estimator of soil moisture in the study area, even when soils are covered by biocrusts. ATI was then used as a proxy of soil moisture in the subsequent analysis.

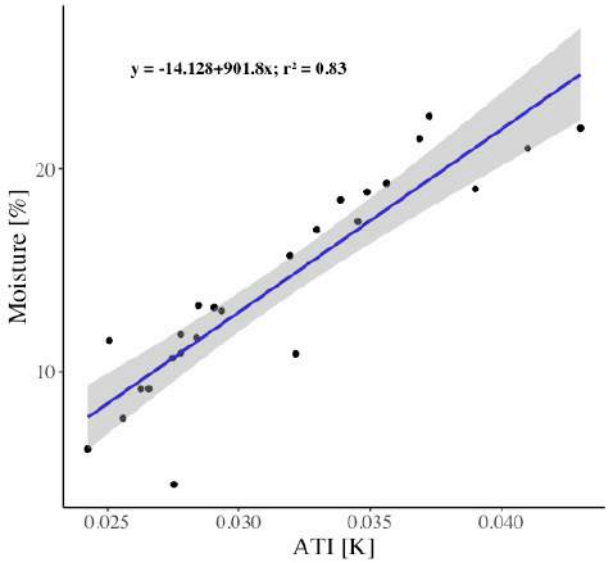

Figure 23. Linear regression between Apparent Thermal Inertia (ATI) and soil moisture in the 23 field plots used in this study. Shaded areas represent ±95% symmetrical confidence interval.

3.4. Analysis of soil properties

Soils in the study area are Gypsiric Leptosols and this is represented by the very high content of SalSol, reaching values higher than 90% in some of the plots, and the low presence of OrgCarb (Table 17). Plots presented similar and low nutrients content, reaching values of P_{tot} of 0% in some plots and close to 0% of N_{tot}. Moisture presented high variation among the plots, with mean values around 14%.

Table 17. Soil attributes retrieved from the 23 2x2 m plots deployed in the field. Mean, Max, Min, SD: mean, maximum, minimum and standard deviation, respectively. SolSal: soluble salts; OrgCarb: organic carbon; P_{tot}: total phosphorus; N_{tot}: total nitrogen.

Soil attribute	Mean	Max	Min	SD
Moisture (%)	14.3	22.6	4.44	5.3
SolSal (%)	81	96	19	15.02
OrgCarb (kg m^{-2})	0.92	3.96	0.14	0.74
P_{tot} (%)	0.6	7.26	0	1.44
N_{tot} (%)	0.08	0.37	0.01	0.07

3.5. Statistical analysis

3.5.1. Relationships between terrain attributes and soils in the study plots

Terrain attributes in the field plots were found to range differently in the four zones sampled (Fig. 24). The Elevation presented similar values in zones 1 and 2 (area A) and in zones 3 and 4 (area B). The Slope was higher in zones 1 and 3, reaching values of 35% of slope gradient. As expected, LSF presented similar patterns to Slope. The TWI presented values not statistically different around 3.5 in the four zones. PSIR showed an opposite pattern to Northernness, with higher values in zones 1 and 3, which are mainly exposed to South-West and South, respectively, indicating higher evapotranspiration. PSIR presented lower values in zone 2 mainly exposed to the East and minimum values in zone 4, mainly exposed to the North. In line with the previous results, the ATI, i.e. soil moisture, presented the highest values in North-facing plots, while values in the other slopes were similar.

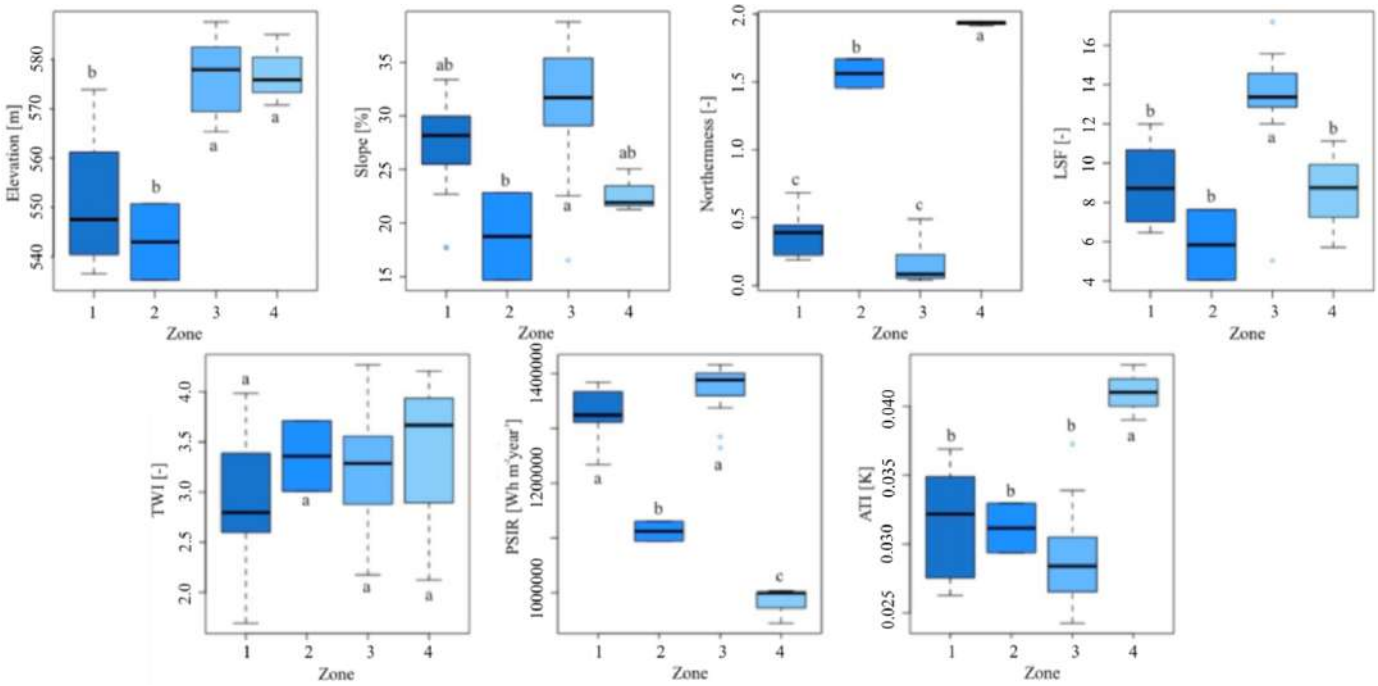

Figure 24. Box plots of the terrain attributes for the different aspects of the plots deployed in the field. The different lowercase letters indicate statistically significant differences between aspects (post-hoc Duncan test following one-way ANOVA). 1, 2, 3 and 4 indicate the study areas of the study, which are mainly exposed to West, East, South and North, respectively. LSF: length slope factor; TWI: topographic wetness index; PSIR: potential solar incoming radiation; ATI: apparent thermal inertia.

Among the terrain attributes investigated, Northernness, ATI and PSIR are the ones that explained most of variance of the soil properties (Table 18). PSIR explained much of this variance, with values of η^2 close to 0.4 when related with SalSol, OrgCarb, P_{tot} and N_{tot}. Northerness and ATI showed slightly lower values of μ^2than PSIR for the same soil properties.

Table 18. Descriptive statistics (i.e. mean and standard deviation) of soil properties grouped in terciles of terrain attributes:, Slope, North (Northerness), ATI (apparent thermal inertia), PSIR (potential solar incoming radiation). L: low; M: medium; H: high. Correlation ratio (μ^2) among soil variables and topography variables is also reported. Only variables with μ^2 higher than 0.2 are represented. Moisture (%); SolSal: soluble salts (%); OrgCarb: organic carbon (km m^{-2}); P_{tot}: total phosphorus (%); N_{tot}: total nitrogen (%).

North	L			M			H			η^2
SolSal	86.50	±	4.74	68.50	±	4.94	62.50	±	29.21	0.43
OrgCarb	1.24	±	0.57	1.39	±	0.62	3.27	±	2.49	0.35
P_{tot}	112.72	±	30.51	167.01	±	65.05	219.50	±	151.14	0.31
N_{tot}	0.06	±	0.03	0.07	±	0.05	0.17	±	0.13	0.35
ATI	L			M			H			η^2
SolSal	86.09	±	3.80	83.30	±	12.02	56.00	±	32.04	0.42
OrgCarb	1.18	±	0.49	1.19	±	0.53	3.30	±	3.04	0.32
P_{tot}	112.81	±	28.91	119.00	±	48.69	251.66	±	167.50	0.37
N_{tot}	0.06	±	0.02	0.06	±	0.03	0.18	±	0.15	0.35
PSIR	L			M			H			η^2
SolSal	56.00	±	32.04	78.25	±	12.31	86.31	±	4.67	0.45
OrgCarb	3.30	±	3.04	1.28	±	0.38	1.25	±	0.61	0.35
P_{tot}	251.66	±	167.50	125.00	±	68.01	116.43	±	27.38	0.37
N_{tot}	0.18	±	0.15	0.06	±	0.03	0.06	±	0.03	0.36

3.5.2. Relationships between topography and biocrusts and vegetation distribution at landscape level

The analysis of the semi-variograms of the PCAs of the multispectral images revealed different spatial autocorrelation in the data ranging from 0 to 3 m. Given this, the plots for the next analysis were selected randomly at a minimum distance of 3 m between them.

The RDA indicated that terrain variables significantly explained variation in biocrusts distribution in our study area (42.3% of the total inertia; F=92.5; p<0.001). The first two RDA-axes accounted for 69.2% of the variation for biocrust data (Fig. 25). The most significant variables were: ATI (F= 115.2; p<0.001), Elevation (F=100.8; p<0.001), Northernness (F=32.0; p>0.001) and Veg (F=29.7; p<0.001). In relation to such variables, differences were found between areas dominated by lichens and mosses. Lichen-dominated biocrusts appeared in the left side of the first axis, which was characterized by low values of ATI (i.e. low moisture) and high values of LSF, which indicates high potential soil erosion, and high values of PSIR, that is related to high SolSal, high slope gradient and high values of elevation. Among lichen-dominated biocrusts, Fulg class developed mostly in Zone 3, where there is a significant gradient of elevation and slope, thus these terrain attributes explained much of its distribution. Conversely, typical mosses of shaded areas (i.e. *Pleurochaete squarrosa* and *Syntrichia ruralis*) were more influenced by vegetation presence and soil moisture (high ATI values). Nevertheless, *Tortula revolvens* develops in soils with similar characteristics to those where lichens dominate.

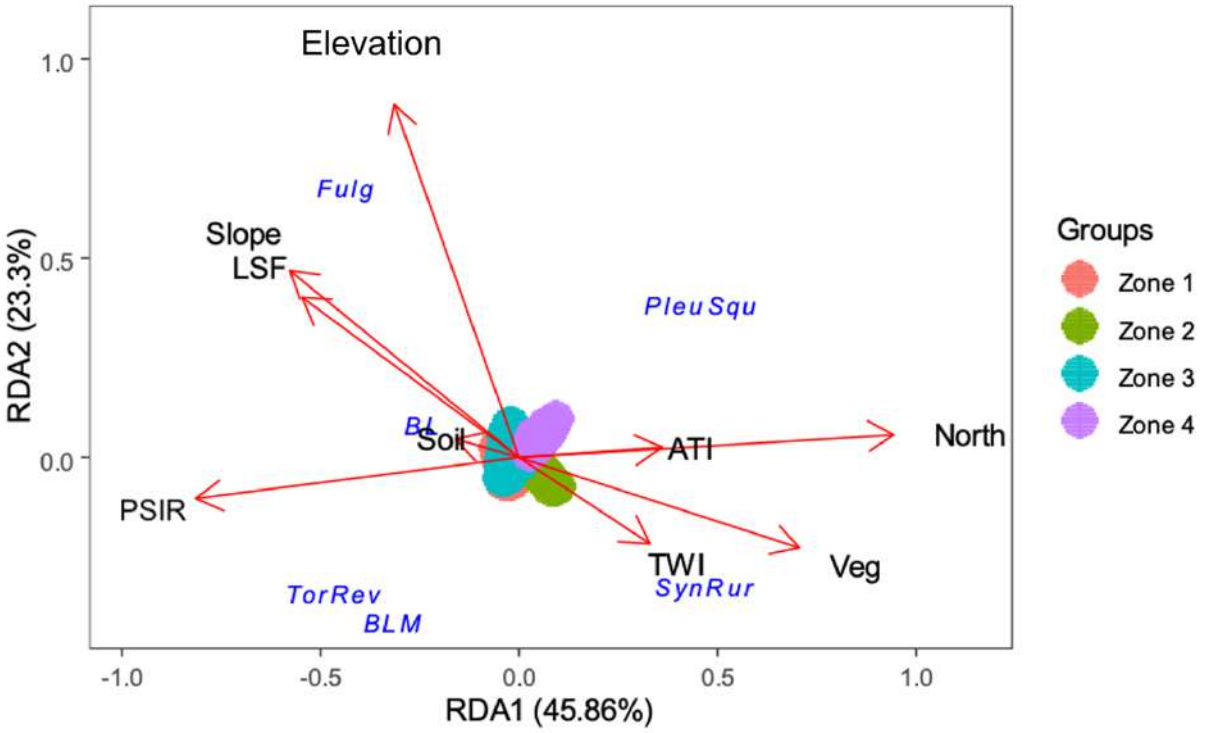

Figure 25. Redundancy analysis (RDA) of the coverage of biocrust and vegetation and terrain attributes in the four zones of the study area. Arrows indicate the direction of increase along a gradient of the corresponding terrain attribute and their direction represent the explanatory relationships with the axis. Length of each arrow is proportional to the correlation between the predictor variable and the ordination. LSF: length slope factor; ATI: apparent thermal inertia; TWI: topographic wetness index; Veg: vegetation; North: northernness; PSIR: Potential Solar Incoming Radiation; Veg: vegetation; BL: bright lichens; BLM: bright lichens with moss; Fulg: *Fulgensia* spp. with moss; PleuSqu: *Pleurochaete squarrosa*; TorRev: *Tortula revolvens*.

4. Discussion

The accurate classification of biocrusts obtained using UAV-based multispectral imagery shows the potential of these platforms to provide dryland composition maps with more detailed spatial resolutions than the ones produced in previous works using airborne and satellite imagery (e.g., Weber et al., 2008; Rodríguez-Caballero et al., 2014; Panigada et al., 2019). The high accuracy reached in discriminating between typical semiarid environmental components (i.e. vascular vegetation, different biocrust compositions and soils) reinforces the ability of SVM algorithm to distinguish between similar spectral classes (Plaza et al., 2009) and of the CR algorithm to improve identification of biocrusts (e.g., Blanco-Sacristán et al., 2019; Panigada et al., 2019; Román et al., 2019). Although differences in the absorption feature caused by chlorophyll at ~660 nm between biocrusts and bare soils are subtle (Weber and Hill, 2016), applying the CR allowed to exploit these differences improving the classification results.

It should be noted that UAV data collection took place during the wet season, when water content in biocrusts is high and pigments are metabolically active (Weber and Hill,

2016). This enhances differences in the spectral properties of biocrusts and improves their identification (Blanco-Sacristán et al., 2019). While the classifications from the multispectral images allowed to map the different environmental components of the study area, the values of ATI derived from TIR imagery correlated very highly with the soil moisture measured in the field. Even though the coupling between ATI and soil moisture is not straight forward in heterogeneous surfaces as in drylands (van Doninck et al., 2011), we demonstrated that the correlation between ATI and soil moisture is maintained also when biocrust cover is present. To our knowledge, these are the first maps of ATI derived from UAV in drylands with presence of biocrust cover. In this study, the ATI map was used to estimate how soil moisture affects biocrust type and distribution, but ATI maps could be also used to better understand water distribution in drylands, where this resource is a key limiting factor to the development of not only biocrusts but also vegetation (Puigdefábregas and Sánchez, 1996).

The UAV RGB images were used to produce fine DTMs from which terrain attributes were derived and utilised to evaluate their impact on soil properties. The overall RMSE of these DTMs was lower than 5 cm and is comparable to previous works using SfM techniques in drylands (e.g., Cunliffe et al., 2016; Gillan et al., 2017). We found that PSIR, ATI and Northernness were the terrain attributes mostly related to soil properties. These attributes explained in similar amounts the distribution of SolSal, OrgCarb, P_{tot} and N_{tot}., illustrating how related these three terrain attributes are. Increased shadows and higher soil moisture, indicated by low PSIR and high ATI, are related to a higher content of soil nutrients, as shown in plots located in zones 2 and 4, mostly East- and North-facing plots, respectively. Increased shadows and soil moisture control the survival and activity of microorganisms (Drenovsky et al., 2004; Borken and Matzener, 2009) and lead to better nutrient cycling and higher activity of microbial communities (e.g., Xue et al., 2018). This increased moisture favours not only the preservation of OrgCarb and its association with other mineral components (Plaza et al., 2012, 2013), but also the presence of vegetation and moss-dominated biocrusts in the most humid slopes. Conversely, plots from zones 1 and 3 presented the greatest PSIR, which can explain lower content of nutrients (lower microbial activity-lower nutrients) and increased content of SolSalt, already observed in other areas with high rates of evapotranspiration (Rodríguez-Caballero et al., 2019).

The variance in soil properties not explained by the terrain attributes could be explained by the presence of vegetation and biocrust cover. Vegetation patches enhance accumulation of water and nutrients capture, which increases biological activity under and close to their cover (e.g., de Graaf et al., 2014; Okin et al., 2015). In addition, vegetation increases shadows where it appears, promoting microbial activity (e.g., Huang et al., 2015; Xue et al., 2018) and thus soil nutrients content. Particularly, *M. tenacissima*, the dominant species in the study area, modifies stocks of soil carbon and organic matter (e.g. Gauquelin et al., 1996; Maestre et al., 2001; Kaouthar and Chaieb, 2009), while its effect on N content is less clear; some studies have found negative effects on this parameter (Armas and Pugnaire, 2011) while other positive effects (Castillo-Monroy et al., 2010) when compared to non-vegetated surfaces.

Together to the effect of vegetation on soil properties, biocrusts have been found to take up significant amounts of atmospheric C and N by photosynthesis and N fixation (Elbert et al., 2012), thus being an important pool and source of organic inputs into the soil in drylands

(Castillo-Monroy et al., 2011; Chamizo et al., 2012b; Concostrina-Zubiri et al., 2013). Furthermore, biocrusts strength soil structure by interacting with mineral particles and formatting aggregates (Belnap, 2013; Eldridge and Leys, 2003), thus protecting soil from C loss. Biocrusts promote microbial community growth where they appear and the increased shadows created by vegetation increase indirectly this growth (Huang et al., 2015). However, the role of biocrusts on soil nutrients content depends on biocrust composition and patch-size distribution (e.g., Delgado-Baquerizo et al., 2015; Sedia and Ehrenfeld, 2006; Bowker et al., 2013). For example, mosses have greater photosynthetic capacity compared to other types of biocrust (Weber and Hill, 2016), thus can incorporate higher levels of carbon to the soil, and positive relationships between Nitrogen and their presence of mosses have already been observed before (Delgado-Baquerizo et al., 2016). This might affect the increased soil nutrients content in the North- and East-facing plots in the study area, where mosses appear dominating plant interspaces, as observed in the RDA analysis in this work.

The different sensitivity of biocrusts to the distribution of resources conditions the composition of dryland landscapes. In this work, the RDA analysis conducted using data from 540 points showed that *Fulgensia spp.* presented a strong positive relationship with unstable zones (high values of Slope and LSF). *Fulgensia* spp. has already been observed in unstable terrains several times, highlighting the pioneering behaviour of this genus (Rodríguez-Caballero et al., 2013; Cantón et al., 2020; Miralles et al., 2020). Mosses typically found in shaded areas (i.e. *Pleurochaete squarrosa* and *Syntrichia ruralis*) dominated areas with low PSIR, North aspect and high presence of vascular vegetation. A positive plant-biocrust relationship is common for bryophytes (Zhou et al., 2020) and close correspondence with *M. tenacissima* presence has already been observed (Martínez-Sánchez, 1994).

The RDA showed a lower explanatory power of the terrain attributes regarding *Tortula revolves*, a moss that develops in arid environments, and BLM class dominated by the association of *Diploschistes diacapsis* and *Squamarina lentigera* (BLM). They appeared in more stable zones (i.e. low values of Slope and LSF), as already observed in geographic area with similar characteristics (e.g., Loppi et al., 2004; Ladrón de Guevara et al., 2018) and with high solar radiation. *Squamarina lentigera* in particular can be physiologically adapted to light-exposed environments, and requires high temperatures for optimal photosynthesis while being well hydrated (Lange et al., 1997). Nevertheless, *Diploschistes diacapsis,* the dominant species of BL was also found in area with higher slopes and LSF. This species is very versatile and can adapt its physiology depending on the characteristics where it grows (Pintado et al., 2005). This is why we found it, as dominant species in BL class, also in area with higher Slope and LSF representing here the early stage of biocrust development.

It is generally accepted that cyanobacteria-dominated crusts appear in the early stages of biocrust development (Belnap, 2006) and facilitate later stages of development by exuding polysaccharide sheaths, which bind soil particles, enhance moisture uptake and increase soil fertility by N-fixation (Belnap, 2006; Tsygankob, 2007). However, previous studies have cast doubt on the widely accepted view that regards cyanobacteria as needed in biocrust succession (e.g., Kidron, 2019, Read et al., 2016). In our study area, lichen-dominated biocrusts, particularly rich in *Diploschistes diacapsis,* can develop directly on outcrop rocks with very few millimetres of soil beneath them, as indicated by the presence of these biocrusts in the axis

of the RDA plot dominated by unstable terrain (i.e. high values of LSF, Slope and Elevation). In contrast to the classical biocrust development model, we found mixed patches of lichens and moss (thought to be of the last stages of development) in the left axis of the RDA plot, where the terrain is represented by greater slope. This might be explained by the fact that the successional development of biocrust communities might be more affected by water availability, rather than by soil stability in areas where gypsum substrates with fine soil texture favour stability. In these areas with outcrop rock, high concentrations of gypsum and higher solar radiation (i.e. high values of PSIR), lichens are more adapted to establish and develop than a moss-dominated biocrust or plants. These latter assemblages appear last and become dominant in areas with higher soil moisture and North-facing areas, where soil and micro-environmental conditions are less selective. In the Tabernas desert (southern Spain, Almería; Rodríguez-Caballero et al., 2019), a close site with 220 mm of mean annual rainfall, similar lichen-dominated biocrusts appear in north-faced slopes (low evapotranspiration, low PSIR), while in our study area they appear in south-facing slopes (high evapotranspiration, high PSIR). The local hydric availability might be more affected by the terrain attributes rather than rainfall water inputs, which ultimately affects biocrusts' distribution in drylands. For this reason, it is difficult to make generalizations in the development of biocrusts' communities and developing monitoring methodologies that allow up-scaling local relationships of biocrusts with the terrain is key for dryland ecology.

5. Conclusions

Providing detailed information from the terrain using RGB imagery and of soil moisture using maps of ATI help to understand the relationships of biocrusts with the ecosystems where they appear, as done in this work. Furthermore, accurate maps as the ones presented in this work can help to up-scale the local effect of biocrust components on ecosystem functioning by increasing the accuracy of erosion and infiltration modelling in drylands and help to understand their relationship with the terrain at higher scales than at plot level. These aspects of dryland ecology are key to understand the distinctive role that biocrust-dominated surfaces have on water runoff and erosion depending on the predominant type of biocrust (e.g., Rodríguez-Caballero et al., 2012, 2015; Wang et al., 2017). For this reason, producing maps with a very high resolution like the ones obtained in this work will help to monitor these communities in space and time, a key task to understand the compositional changes they are already and will experience in the next decades (Escolar et al., 2012; Ladrón de Guevara et al., 2018).

Since field-based data collection implies many drawbacks, mainly related to time and costs (Palmer et al., 2002), applying UAV-based methodologies as the one developed in this work will help to build standardized procedures in actual and future dryland monitoring programs, while providing very detailed information of these environments. However, not all drylands have the same structural and functional organisation and present a wide spectrum of compositions. We observed some discrepancies with the traditional biocrusts' development models, in which more advanced stages (i.e. mixed patches of lichens and moss) are assumed to appear in stable soils. Thus, we suggest to reconsider this traditional approach by evaluating it in future works using methodologies as the one developed in this study, which can provide the very fine spatial resolution maps of dryland composition and terrain attributes needed for this.

Replicating the methodology developed in this work in other drylands could help to better understand the relationships between biocrusts and their environment, which are likely to change due to the ongoing context of global change. This will contribute to our understanding of the underlying processes controlling biocrusts' spatial distribution in drylands and the development of current and future successional trajectories of these communities in relation with dryland terrain.

Chapter 5
Conclusions of this thesis

The main objective of this PhD thesis was to advance our understanding of terrain control on dryland functioning by using multi-source remotely sensed data. The existing links between terrain, dryland vegetation and biocrust optical properties were analyzed in the context of two different dryland ecosystems. This shows how powerful multi-source image analysis is to infer the effect that terrain has on dryland functioning. Furthermore, the link between biocrusts' optical properties and their composition was analyzed not only in relation with dryland terrain, but also in the context of their spectral diversity, proving how useful it might be to improve actual dryland monitoring and conservation programs.

To achieve this, I addressed different approaches for studying dryland vegetation and biocrust distribution using remote sensing sensors. First, I evaluated the evolution of SfM-based digital photogrammetry in the last two decades and discussed its potential to study terrain and vegetation in different scenarios, with a particular focus in drylands. Second, I used an OBIA approach to infer changes in a long-lived population of plants during more than 60 years and related its population dynamics to human actions. Third, I evaluated the identification of biocrust-forming lichens using SVMs and used their spectral diversity to estimate their α-diversity. Fourth, I used an innovative mixed approach, using image analysis on RGB, multispectral and TIR imagery in a dryland environment dominated by biocrust communities to evaluate the control exerted by the terrain on them. These approaches have been presented in Chapters 1, 2, 3 and 4 of this thesis and the main outcomes of each chapter are summarised below. Following these are concluding remarks and potential perspectives of this work.

1.1. Main results

Chapter 1. Terrain attributes of drylands with complex geomorphologies and covered by dense vegetation can be evaluated using Structure-from-Motion-based photogrammetry.

This is the main outcome of Chapter 1, aimed at evaluating the evolution of digital photogrammetry and its applicability in vegetation and terrain characterization in the last twenty years. Digital photogrammetry has considerably advanced in this period both in terms of software and hardware and its application in several environments and scales ensures this. However, many of the principles and cautions existing twenty years ago are still relevant, being necessary by practitioners to know how to properly use check and control points for validation, and the influence of inaccurate camera calibrations in the final outputs of this method. Considering these cautionary aspects, application of SfM-based digital photogrammetry in drylands, even when the terrain is complex and the vegetation is densely distributed, has proved to be useful for hydrology modelling purposes. This allows to evaluate the effect that terrain might have on nutrients' distribution and soil properties in drylands.

Chapter 2. Object-based image analysis is a powerful tool to infer anthropogenic actions on the health of dryland vegetation communities.

This is the main result of Chapter 2, aimed at monitoring a population of sparse shrubs in a groundwater-dependent dryland ecosystem during a 60 years-long period. The combination of very high-resolution historical images, OBIA and DTMs, derived from LiDAR data, allowed to track spatio-temporal changes in this population and to relate them with human actions. These results suggest that monitoring changes in the number and the cover of vegetation communities in dryland ecosystems help to infer anthropogenic disturbances that affect their health. In this study case, the groundwater extraction from the aquifer that feeds the population of plants and the massive extraction of sands in the area, both caused by human actions, were related with changes in the health and composition of the studied ecosystem. Thus, the implementation of semi-automatic methods to characterize dryland ecosystems as the one presented in this chapter can help to infer the effects of human activities on shrub populations in drylands. This could reduce costs and improve current and future dryland monitoring programs.

Chapter 3. Spectral Diversity can be used to estimate the α-diversity of biocrust-forming lichens.

This is the main outcome from the study of Chapter 3, aimed at using hyperspectral high spatial resolution images to identify biocrust-forming lichens at genus level for the evaluation of the relationships between the spectral and α-diversity of lichen-dominated communities. In this study, the very high accuracies obtained classifying the hyperspectral images using SVMs showed the reliability of this methodology to identify biocrust-forming lichens. Therefore, I was able to extract pure spectral signatures of different biocrust constituents and to evaluate the relationships between α-diversity and spectral diversity of lichens. The SD_CR_{680} nm was the spectral diversity metric found to predict the best α-diversity metrics that include richness and evenness in their calculations (i.e. Pielou's and Simpson's indices). As such, I suggest the use of this metric to track spatio-temporal changes in lichen-dominated biocrust communities. Upscaling the results of this study to coarser scales in drylands is a key task in any monitoring program aiming to assess the impacts of ongoing climate change and desertification processes in these environments. For this, using fixed-cameras deployed in the field or multiple sensors onboard UAVs could greatly help.

Chapter 4. Multi-source UAV-based imagery can be used to map dryland biocrusts and to evaluate the effect of the terrain on their distribution. TIR imagery can be used to evaluate soil moisture in heterogeneous dryland surfaces.

These are the main results of Chapter 4, aimed at understanding the effect of terrain attributes on biocrust distribution in drylands. In this work, I used a multi-source approach using TIR, RGB and multispectral data, each with specific aims to achieve the main objective. TIR imagery was used to estimate soil moisture by creating maps of ATI, RGB imagery was used to extract terrain attributes and multispectral imagery was used to map dryland ecosystem components. The TIR imagery allowed to create maps of ATI and to successfully relate this

variable with soil moisture for the first time in a dryland ecosystem dominated by biocrust communities. The fine spatial resolution of the RGB imagery allowed to filter the vegetation and to produce very fine DTMs, from which terrain attributes were derived and found to affect the variance of soil nutrients in the study area. The multispectral images allowed to produce the most finely detailed maps of drylands until the date. Fractional covers of the main surface units of biocrusts were related to terrain attributes and ATI. The aspect of the terrain, the soil moisture and the elevation were the terrain attributes explaining most of biocrust distribution in the study area. Furthermore, mixed biocrusts of lichens and mosses and lichen-dominated ones were found in unstable terrains, contrary to traditional biocrust development models in drylands. Thus, these models should not be generalized, since they can not be applied to all drylands worldwide. This work shows the potential of using UAVs on dryland ecology in systems with complex geomorphologies, where accurate representations of their composition are key to up-scale their local effects to regional levels.

1.2. Concluding remarks and outlook

In this PhD thesis, multiple approaches for identifying dryland vegetation and biocrust were tested and discussed. Through the four chapters presented, these approaches were evaluated to characterise vegetation and biocrust from a structural and functional point of view, providing a thorough understanding of dryland functioning, with a particular focus on the effect that terrain has on dryland composition. This was made possible by the integration of multi-source remote sensing data and their correct exploitation by using different remote sensing techniques, adequate to each study case.

Overall, the results obtained effectively demonstrate the strength of multi-source image analysis to identify vegetation and biocrust in drylands and to infer the effect that terrain has on their distribution. In particular, the use of RGB imagery by applying SfM-based digital photogrammetry allowed to create digital models of terrain and vegetation; the analysis of RGB imagery over a period of 60 years allowed to infer the effect of anthropogenc actions in a long-lived community of scattered vegetation; the analysis of very high spatial resolution hyperspectral imagery allowed to estimate the α-diversity of biocrust-forming lichens; the fusion analysis of RGB, multispectral and TIR imagery allowed to evaluate the effect that terrain has on dryland biocrust distribution. These achievements are particularly important under the actual scenario of climate change, which is expected to increase drylands' cover worldwide and change their composition and functioning in the next decades.

The methodologies here shown will allow to characterise in higher detail dryland vegetation and biocrust communities at regional scale, which has proved to be a challenging task until the date. Gathering data of drylands at this level will produce detailed and more complete datasets of dryland optical properties and functioning. An enhanced understanding of the link between dryland optical properties and dryland functioning will permit a more operational use of remotely sensed data to reveal new insights into dryland dynamics. Thus, this improved understanding of dryland functioning will allow to increase current knowledge of the key role these ecosystems play in global water and nutrients cycling. This is key for a right understanding of the complex system the Earth is.

Bibliography

Aasen, H., Honkavaara, E., Lucieer, A. & Zarco-Tejada, P. (2018). Quantitative remote sensing at ultra-high resolution with UAV spectroscopy: A review of sensor technology, measurement procedures, and data correction workflows. Remote Sens. 10, 1091.

Adessi, A., de Carvalho, R. C., De Philippis, R., Branquinho, C., & da Silva, J. M. (2018). Microbial extracellular polymeric substances improve water retention in dryland biological soil crusts. Soil Biology and Biochemistry, 116, 67-69.

Adhikari, B., & Nadella, K. (2011). Ecological economics of soil erosion: A review of the current state of knowledge. Annals of the New York Academy of Sciences, 1219, 134-152

Aguiar, M.R. & Sala, O.E. (1999). Patch structure, dynamics and implications for the functioning of arid ecosystems. Trends Ecol. Evol. 14, 273–277.

Aksoy, S., Tilton, J.C. & Tarabalka, Y. (2015). Image segmentation algorithms for land categorization. In Remote Sensing Handbook V.1 Remotely Sensed Data Characterization, Classification, and Accuracies; Taylor & Francis: Abingdon, UK, 2015; pp. 317–342. ISBN 978-1-4822-1786-5.

Anderson, K. & Gaston, K.J. (2013). Lightweight unmanned aerial vehicles will revolutionize spatial ecology. Front. Ecol. Environ. 11, 138–146.

Aneece, I.P.; Epstein, H.; Lerdau, M. (2017). Correlating species and spectral diversities using hyperspectral remote sensing in early-successional fields. Ecol. Evol. 7, 3475–3488.

Armas, C., & Pugnaire, F. I. (2011). Belowground zone of influence in a tussock grass species. Acta Oecologica, 37(3), 284-289

Armstrong A, Quinton JN, Heng BCP, & Chandler, J.H. (2011). Variability of interrill erosion at low slopes. Earth Surface Processes and Landforms 36(1): 97–106.

Assmann, J. J., Kerby, J. T., Cunliffe, A. M., & Myers-Smith, I. H. (2018). Vegetation monitoring using multispectral sensors—best practices and lessons learned from high latitudes. Journal of Unmanned Vehicle Systems, 7(1), 54-75.

Asner, G.P.; Knapp, D.E.; Kennedy-Bowdoin, T.; Jones, M.O.; Martin, R.E.; Boardman, J.; Hughes, R.F. (2008). Invasive species detection in Hawaiian rainforests using airborne imaging spectroscopy and LiDAR. Remote Sens. Environ. 112, 1942–1955.

Bear, J.; Cheng, A.H.-D.; Sorek, S.; Ouazar, D.; Herrera, I. (1999). Seawater Intrusion in Coastal Aquifers: Concepts, Methods and Practices; Springer Science & Business Media: Berlin, Germany, 1999; Volume 14.

Belnap, J., (2006). The potential roles of biological soil crusts in dryland hydrologic cycles. Hydrol. Process 20, 3159e3178

Belnap, J.; Lange, O.L. (2003). Biological Soil Crusts: Structure, Function, and Management; Springer Science & Business Media: Berlin, Germany, 2003; p. 150.

Benaud, P. (2017). Exploring the multiple techniques available for developing an understanding of soil erosion in the UK. Exeter: University of Exeter.

Bellingham, P.J.; Sparrow, A.D. (2000). Resprouting as a life history strategy in woody plant communities. Oikos 2000, 89, 409–416.

Benz, U.C.; Hofmann, P.; Willhauck, G.; Lingenfelder, I.; Heynen, M. (2004). Multi-resolution, object-oriented fuzzy analysis of remote sensing data for GIS-ready information. ISPRS J. Photogramm. Remote Sens. 2004, 58, 239–258.

Berdugo, M., Delgado-Baquerizo, M., Soliveres, S., Hernández-Clemente, R., Zhao, Y., Gaitán, J. J., Gross, N., Saiz, H., Maire, V., Lehmann, A., Rillig, M. C., Solé, R. V., and Maestre, F. (2020). Global ecosystem thresholds driven by aridity. Science, 367(6479), 787-790.

Berdugo, M.; Maestre, F.T.; Kéfi, S.; Gross, N.; Le Bagousse-Pinguet, Y.; Soliveres, S. (2019). Aridity preferences alter the relative importance of abiotic and biotic drivers on plant species abundance in global drylands. J. Ecol. 2019, 107, 190–202.

Berger, C., Schulze, M., Rieke-Zapp, D. & Schlunegger, F. (2010). Rill development and soil erosion: A laboratory study of slope and rainfall intensity. Earth Surface Processes and Landforms 35(12): 1456–1467.

Beven, K.J., Kirkby, M.J. (1979). A physically based, variable contributing area model of basin hydrology. Hydrological Sciences Bulletin 24: 43–69.

Blanco-Sacristán, J., Panigada, C., Tagliabue, G., Gentili, R., Colombo, R., Ladrón de Guevara, M., Maestre, F.T. & Rossini, M. (2019). Spectral Diversity Successfully Estimates the α-Diversity of Biocrust-Forming Lichens. Remote Sensing, 11(24), 2942.

Blaschke, T. (2010). Object based image analysis for remote sensing. ISPRS J. Photogramm. Remote Sens. 65, 2–16.

Bond, W.J.; Midgley, J.J. (2001). Ecology of sprouting in woody plants: The persistence niche. Trends Ecol. Evol. 16, 45–51.

Borken, W., Matzner, E. (2009). Reappraisal of drying and wetting effects on C and N mineralization and fluxes in soils. Global Change Biol. 15, 808-824.

Bowker, M.A., Belnap, J., Büdel, B., Sannier, C., Pietrasiak, N., Eldridge, D.J., Rivera-Aguilar, V. (2016). Controls on distribution patterns of biological soil crusts at micro- to global scales. In Biological Soil Crusts: An Organizing Principle in Drylands, Weber B, Büdel B, Belnap J (eds), Vol. 226, Ecological Studies (Analysis and Synthesis). Springer: Cham; 173–197.

Bowker, M.A.; Eldridge, D.J.; Val, J.; Soliveres, S. (2013). Hydrology in a patterned landscape is co-engineered by soil-disturbing animals and biological crusts. Soil Biol. Biochem. 61, 14–22.

Bowker, M.A.; Maestre, F.T.; Escolar, C. (2010). Biological crusts as a model system for examining the biodiversity-ecosystem function relationship in soils. Soil Biol. Biochem. 42, 405–417.

Bowker, M. A., Maestre, F. T., & Mau, R. L. (2013). Diversity and patch-size distributions of biological soil crusts regulate dryland ecosystem multifunctionality. Ecosystems, 16(6), 923-933.

Bowker, M.A., Mau, R.L., Maestre, F.T., Escolar, C., & Castillo-Monroy, A.P. (2011). Functional profiles reveal unique roles of various biological soil crust organisms in Spain. Funct. Ecol. 25, 787–795.

Bradlye, A.P. (1997). The use of the area under the ROC curve in the evaluation of machine learning algorithms. Pattern Recognit. 30, 1145–1159.

Brodu, N., & Lague, D. (2012). 3D terrestrial lidar data classification of complex natural scenes using a multi- scale dimensionality criterion: Applications in geomorphology. ISPRS Journal of Photogrammetry and Remote Sensing 68(1): 121–134.

Büdel, B., Belnap, J. (2016). Büdel, B., Belnap, J. Eds.; Ecological Studies; Springer: Berlin, Germany, 2016; Vol 226, pp. 451–476.

Bühler Y, Marty M, Egli L, Veitinger, J., Jonas, T., Thee, P. & Ginzler, C. (2015). Snow depth mapping in high-alpine catchments using digital photogrammetry. Cryosphere 9(1): 229–243.

Burkart A, Aasen H, Alonso L, et al. (2015). Angular dependency of hyperspectral measurements over wheat characterized by a novel UAV based goniometer. Remote Sensing 7(1): 725–746.

Burnett, C. & Blaschke, T. (2003). A multi-scale segmentation/object relationship modelling methodology for landscape analysis. Ecol. Model. 168, 233–249.

Campbell, G.S., Norman, J.M. (1988). Introduction to Environmental Biophysics, second ed. Springer edition, USA

Cancio, I.; González-Robles, A.; Bastida, J.M.; Manzaneda, A.J.; Salido, T.; Rey, P.J. (2016). Habitat loss exacerbates regional extinction risk of the keystone semiarid shrub Ziziphus lotus through collapsing the seed dispersal service by foxes (Vulpes vulpes). Biodivers. Conserv. 25, 693–709.

Cano-Díaz, C., Mateo, P., Muñoz-Martín, M. Á., & Maestre, F. T. (2018). Diversity of biocrust-forming cyanobacteria in a semiarid gypsiferous site from Central Spain. Journal of arid environments, 151, 83-89.

Cantón, Y., Chamizo, S., Rodriguez-Caballero, E., Lázaro, R., Roncero-Ramos, B., Román, J. R., & Solé-Benet, A. (2020). Water Regulation in Cyanobacterial Biocrusts from Drylands: Negative Impacts of Anthropogenic Disturbance. Water, 12(3), 720.

Carlson, K. M., Asner, G. P., Hughes, R. F., Ostertag, R., & Martin, R. E. (2007). Hyperspectral remote sensing of canopy biodiversity in Hawaiian lowland rainforests. Ecosystems, 10(4), 536-549.

Castillo-Monroy, A. P., Benítez, Á., Reyes-Bueno, F., Donoso, D. A., & Cueva, A. (2016). Biocrust structure responds to soil variables along a tropical scrubland elevation gradient. Journal of Arid Environments, 124, 31-38.

Castillo-Monroy, A. P., Maestre, F. T., Rey, A., Soliveres, S., & García-Palacios, P. (2011). Biological soil crust microsites are the main contributor to soil respiration in a semiarid ecosystem. Ecosystems, 14(5), 835-847.

Carey, S. K., & Woo, M. K. (1999). Hydrology of two slopes in subarctic Yukon, Canada. Hydrological Processes, 13(16), 2549-2562.

Cayan, D.R., Das, T., Pierce, D.W., Barnett, T.P., Tyree, M.& Gershunov, A. (2010). Future dryness in the southwest US and the hydrology of the early 21st century drought. Proc. Natl. Acad. Sci. U. S. A. 107, 21271–21276.

Chamizo, S., Cantón, Y., Lázaro, R., Solé-Benet, A., & Domingo, F. (2012). Crust composition and disturbance drive infiltration through biological soil crusts in semiarid ecosystems. Ecosystems, 15(1), 148-161.

Chamizo, S., Cantón, Y., Rodríguez-Caballero, E., & Domingo, F. (2016). Biocrusts positively affect the soil water balance in semiarid ecosystems. Ecohydrology, 9(7), 1208-1221.

Chamizo, S., Rodríguez-Caballero, E., Román, J. R., & Cantón, Y. (2017). Effects of biocrust on soil erosion and organic carbon losses under natural rainfall. Catena, 148, 117-125.

Chamizo, S., Stevens, A., Cantón, Y., Miralles, I., Domingo, F. & VanWesemael, B. (2012). Discriminating soil crust type, development stage and degree of disturbance in semiarid environments from their spectral characteristics. Eur. J. Soil Sci. 63, 42–53.

Chandler, J. (1999). Effective application of automated digital photogrammetry for geomorphological research. Earth Surface Processes and Landforms 24(1): 51–63

Chandler, J.H., Fryer, J.G. & Jack, A. (2005). Metric cap- abilities of low-cost digital cameras for close range surface measurement. The Photogrammetric Record 20(109): 12–26.

Chang, C.; Lin, C. (2011). LIBSVM: A library for support vector machines. ACM Trans. Intell. Syst. Technol, 2.

Chen, J.; Yuan Zhang, M.; Wang, L.; Shimazaki, H.; Tamura, M. (2005). A new index for mapping lichen-dominated biological soil crusts in desert areas. Remote Sens. Environ. 96, 165–175.

Clark, R.N. & Roush, T.L. (1984). Reflectance spectroscopy. Quantitative analysis techniques for remote sensing applications. J. Geophys. Res. 89, 6329–6340

Claps, P., & G. Laguardia. (2004). Assessing spatial variability of soil water content through thermal inertia and NDVI. Proc. SPIE, Int. Soc. Opt. Eng. 5232:378–387

Cohen, J. (1968). Weighted kappa: Nominal scale agreement provision for scaled disagreement or partial credit. Psychol. Bull. 70, 213–220.

Collinge, S.K.; Palmer, T.M. (2002). The influences of patch shape and boundary contrast on insect response to fragmentation in California grasslands. Landsc. Ecol. 17, 647–656.

Colombo C. & Miano T. (2015). Metodi di analisi chimica del suolo. Società italiana della scienza del suolo; Associazione Italiana dei Laboratori Pubblici di Agrochimica. Pubblicità & Stampa, Modugno (Bari), pp. 1-470.

Concostrina-Zubiri, L., Huber-Sannwald, E., Martínez, I., Flores Flores, J.L., Escudero, A. (2013). Biological soil crusts greatly contribute to small-scale soil heterogeneity along a grazing gradient. Soil Biol. Biochem. 64, 28–36.

Conel, J. E., Green, R. O., Vane, G., Bruegge, C. J., Alley, R. E., & Curtiss, B. J. (1987). AIS-2 radiometry and a comparison of methods for the recovery of ground reflectance.

Congalton, R.G.; Green, K. (2008). Assessing the Accuracy of Remotely Sensed Data: Principles and Practices, 2nd ed.; CRC Press, Taylor and Francis Group: London, UK, 2008.

Cook, B.I., Ault, T.R. & Smerdon, J.E. (2015). Unprecedented 21st century drought risk in the American Southwest and Central Plains. Sci. Adv. 1, e1400082

Cortes, C.; Vapnik, V. (1995). Support-Vector Networks. Mach. Learn. 1995, 297, 273–297.

Cunliffe, A.M., Brazier, R.E. & Anderson. K. (2016). Ultra-fine grain landscape-scale quantification of dryland vegetation structure with drone-acquired structure- from-motion photogrammetry. Remote Sensing of Environment 183: 129–143

Cunliffe, A. M., McIntire, C. D., Boschetti, F., Sauer, K. J., Litvak, M., Anderson, K., & Brazier, R. E. (2020). Allometric Relationships for Predicting Aboveground Biomass and Sapwood Area of Oneseed Juniper (Juniperus monosperma) Trees. Frontiers in Plant Science, 11(February), 1–12.

Dandois, J.P. & Ellis, E.C. (2010). Remote sensing of vegetation structure using computer vision. Remote Sensing 2(4): 1157–1176.

Dandois, J.P. & Ellis, E.C. (2013) High spatial resolution three-dimensional mapping of vegetation spectral dynamics using computer vision. Remote Sensing of Environment 136: 259–276.

Dandois JP, OlanoMand Ellis EC (2015). Optimal altitude, overlap, and weather conditions for computer vision UAV estimates of forest structure. Remote Sensing 7(10): 13895–13920.

Daniele, L.; Sola, F.; Izquierdo, A.V.; Bosch, A.P. (2010).Coastal aquifers and desalination plants: Some interpretations to new situations. In Proceedings of the Conference on Water Observation and Information System for Decision Support, Balwois, Ohrid, Republic of Macedonia, 25–29 May 2010.

Deblauwe, V.; Barbier, N.; Couteron, P.; Lejeune, O.; Bogaert, J. (2008). The global biogeography of semi-arid periodic vegetation patterns. Glob. Ecol. Biogeogr. 2008, 17, 715–723.

de Graaff, M.-A., Throop, H. L., Verburg, P. S. J., Arnone, J. A., & Campos, X. (2014). A synthesis of climate and vegetation cover effects on biogeochemical cycling in shrub- dominated drylands. Ecosystems, 17, 931–945

DeLeo, J.M. (1993). Receiver operating characteristic laboratory (ROCLAB): Software for developing decision strategies that account for uncertainty. In Proceedings of the 1993 (2nd) International Symposium on Uncertainty Modeling and Analysis, College Park, MD, USA, 25–28 April 1993; IEEE. Computer Society Press: College Park, MD, USA, 1993; pp. 318–325.

Delgado-Baquerizo, M., Gallardo, A., Covelo, F., Prado-Comesaña, A., Ochoa, V., & Maestre, F. T. (2015). Differences in thallus chemistry are related to species-specific effects of biocrust-forming lichens on soil nutrients and microbial communities. Functional Ecology, 29(8), 1087-1098.

Delgado-Baquerizo, M., Maestre, F. T., Eldridge, D. J., Bowker, M. A., Ochoa, V., Gozalo, B., Berdugo, M., Val, J. & Singh, B. K. (2016). Biocrust-forming mosses mitigate the negative impacts of increasing aridity on ecosystem multifunctionality in drylands. New Phytologist, 209(4), 1540-1552.

Delgado-Baquerizo, M.; Maestre, F.T.; Reich, P.B.; Jeffries, T.C.; Gaitán, J.J.; Encinar, D.; Berdugo, M.; Campbell, C.D.; Singh, B.K. (2016). Microbial diversity drives multifunctionality in terrestrial ecosystems. Nat. Commun. 2016, 7, 10541.

Dobrowski, S.Z.; Safford, H.D.; Cheng, Y.B.; Ustin, S.L. (2008). Mapping mountain vegetation using species distribution modeling, image-based texture analysis, and object-based classification. Appl. Veg. Sci. 2008, 11, 499–508.

Drăgut, L.; Csillik, O.; Eisank, C.; Tiede, D. (2014). Automated parameterisation for multi-scale image segmentation on multiple layers. ISPRS J. Photogramm. Remote Sens. 2014, 88, 119–127.

Drenovsky, R., Vo, D., Graham, K., Scow, K. (2004). Soil water content and organic carbon availability are major determinants of soil microbial community composition. Microbial Ecol. 48, 424-430.

Duffy JP, Cunliffe AM, DeBell L, et al. (2017). Location, location, location: Considerations when using lightweight drones in challenging environments. Remote Sensing in Ecology and Conservation 4(1): 7–19.

Elbert, W., Weber, B., Burrows, S., Steinkamp, J., Büdel, B., Andreae, M. O., & Pöschl, U. (2012). Contribution of cryptogamic covers to the global cycles of carbon and nitrogen. Nature Geoscience, 5(7), 459-462.

Eldridge, D. J., Zaady, E., & Shachak, M. (2000). Infiltration through three contrasting biological soil crusts in patterned landscapes in the Negev, Israel. Catena, 40(3), 323-336.

Eldridge, D. J., Reed, S., Travers, S. K., Bowker, M. A., Maestre, F. T., Ding, J., Belnap, J., Chaudhary, B., Faist, A., Ferrenberg, S., Huber-Sannwald, E., Malam Issa, O. & Antoninka, A. (2020). The pervasive and multifaceted influence of biocrusts on water in the world's drylands. Global Change Biology.

Eltner A and Schneider D (2015). Analysis of different methods for 3D reconstruction of natural surfaces from parallel-axes UAV images. Photogrammetric Record 30(151).

Eltner A, Kaiser A, Abellan A, et al. (2017). Time lapse structure-from-motion photogrammetry for continuous geomorphic monitoring. Earth Surface Processes and Landforms 42(14): 2240–2253.

Eriksson, O. (1996). Regional dynamics of plants: A review of evidence for remnant, source-sink and metapopulations. Oikos 1996, 77, 248–258.

Escolar C, Martínez I, Bowker MA, Maestre FT. (2012). Warming reduces the growth and diversity of biological soil crusts in a semi-arid environment: implications for ecosystem structure and functioning. Philosophical Transactions of the Royal Society of London. Series B: Biological Sciences 367: 3087–3099.

Evans, I.S. (1972). General geomorphology, derivatives of altitude and descriptive statistics. In Spatial Analysis in Geomorphology; Chorley, R.J., Ed.; Harper and Row: Manhattan, NY, USA, 1972; pp. 17–90.

Faist, A. M., Herrick, J. E., Belnap, J., Van Zee, J. W., & Barger, N. N. (2017). Biological soil crust and disturbance controls on surface hydrology in a semi-arid ecosystem. Ecosphere, 8(3), e01691.

Fawcett, T. (2006). An Introduction to ROC Analysis. Pattern Recognit. Lett. 2006, 27, 861–874.

Fawcett, D., Panigada, C., Tagliabue, G., Boschetti, M., Celesti, M., Evdokimov, A., Biriukova, K., Colombo, R., Miglietta, F., Rascher, U. & Anderson, K. (2020). Multi-Scale Evaluation of Drone-Based Multispectral Surface Reflectance and Vegetation Indices in Operational Conditions. Remote Sensing, 12(3), 514.

Fazeli H, Samadzadegan F and Dadrasjavan F (2016). Evaluating the potential of RTK-UAV for automatic point cloud generation in 3D rapid mapping. International Archives of the Photogrammetry, Remote Sensing and Spatial Information Sciences – ISPRS Archives 41(July): 221–226

Fernández-Buces, N.; Siebe, C.; Cram, S.; Palacio, J.L. (2006). Mapping soil salinity using a combined spectral response index for bare soil and vegetation: A case study in the former lake Texcoco, Mexico. J. Arid Environ. 2006, 65, 644–667.

Ferrenber, S.; Reed, S.C.; Belnap, J. (2015). Climate change and physical disturbance cause similar community shifts in biological soil crusts. Proc. Natl Acad. Sci. USA 2015, 112, 12116–12121.

Fisher PF and Tate NJ (2006). Causes and consequences of error in digital elevation models. Progress in Physical Geography 30(4): 467–489.

Foody, G.M.; Mathur, A.; Sanchez-Hernandez, C.; Boyd, D.S. (2006). Training set size requirements for the classification of a specific class. Remote Sens. Environ. 2006, 104, 1–14.

Fraser BT and Congalton RG (2018). Issues in Unmanned Aerial Systems (UAS) data collection of complex forest environments. Remote Sensing 10(6): 908.

Gao, Y.; Mas, J.F.; Kerle, N.; Pacheco, J.A.N. (2011). Optimal region growing segmentation and its effect on classification accuracy. Int. J. Remote Sens. 2011, 32, 3747–3763.

García, D.; Zamora, R. (2003). Persistence, multiple demographic strategies and conservation in long-lived Mediterranean plants. J. Veg. Sci. 2003, 14, 921–926.

García García, J.P.; Sánchez Caparós, A.; Castillo, E.; Marín, I.; Padilla, A.; Rosso, J.I. (2003). Hidrogeoquímica de las aguas subterráneas en la zona de Cabo de Gata. In Tecnología de la Intrusión de Agua de Mar en Acuíferos Costeros: Países Mediterráneos; IGME: Granada, Spain, 2003.

Garzonio, R.; Di Mauro, B.; Cogliati, S.; Rossini, M.; Panigada, C.; Delmonte, B.; Maggi, V.; Colombo, R. (2018). A novel hyperspectral system for high resolution imaging of ice cores: Application to light-absorbing impurities and ice structure. Cold Reg. Sci. Technol. 2018, 155, 47–57.

Gauquelin, T., Jalut, G., Iglesias, M., Valle, F., Fromard, F., & Dedoubat, J. J. (1996). Phytomass and carbon storage in the Stipa tenacissima steppes of the Baza basin, Andalusia, Spain. Journal of Arid Environments, 34(3), 277-286.

Gholizadeh, H.; Gamon, J.A.; Zygielbaum, A.I.; Wang, R.; Schweiger, A.K.; Cavender-Bares, J. (2018). Remote sensing of biodiversity: Soil correction and data dimension reduction methods improve assessment of α-diversity (species richness) in prairie ecosystems. Remote Sens. Environ. 2018, 206, 240–253.

Gillan, J. K., Karl, J. W., Elaksher, A., & Duniway, M. C. (2017). Fine-resolution repeat topographic surveying of dryland landscapes using UAS-based structure-from-motion photogrammetry: Assessing accuracy and precision against traditional ground-based erosion measurements. Remote Sensing, 9(5), 437.

Gillespie, T.W.; Foody, G.M.; Rocchini, D.; Giorgi, A.P.; Saatchi, S. (2008). Measuring and modelling biodiversity from space. Prog. Phys. Geogr. 2008, 32, 203–221.

Goulden T, Hopkinson C, Jamieson R, et al. (2016) Sensitivity of DEM, slope, aspect and watershed attributes to LiDAR measurement uncertainty. Remote Sensing of Environment 179: 23–35.

Goy, J.L.; Zazo, C. (1986). Synthesis of the quaternary in the almeria littoral neotectonic activity and its morphologic features, western betics, Spain. Tectonophysics 1986, 130, 259–270.

Gualtieri, J.A.; Cromp, R.F. (1998). Support vector machines for hyperspectral remote sensing classification. Proc. SPIE 1998, 3584, 221–232.

Guirado, E.; Alcaraz-Segura, D.; Rigol-Sánchez, J.P.; Gisbert, J.; Martínez-Moreno, F.J.; Galindo-Zaldívar, J.; González-Castillo, L.; Cabello, J. (2018). Remote-sensing-derived fractures and shrub patterns to identify groundwater dependence. Ecohydrology 2018, 11, 1933.

Guirado, E., Tabik, S., Alcaraz-Segura, D., Cabello, J., & Herrera, F. (2017). Deep-learning versus OBIA for scattered shrub detection with Google earth imagery: Ziziphus Lotus as case study. Remote Sensing, 9(12), 1220.

Hallberg, B.; Smith-Jonforsen, G.; Ulander, L.M. (2005). Measurements on individual trees using multiple VHF SAR images. IEEE Trans. Geosci. Remote Sens. 2005, 43, 2261–2269.

Haining, R. (1980). Spatial autocorrelation problems. vol. 3. pp. 1–44

Hamraz, H.; Contreras, M.A.; Zhang, J. (2017). Vertical stratification of forest canopy for segmentation of understory trees within small-footprint airborne LiDAR point clouds. ISPRS J. Photogramm. Remote Sens. 2017, 130, 385–392.

Hanley, J.A.; McNeil, B.J. (1982). The meaning and use of the area under a receiver operating characteristic (ROC) curve. Radiology 1982, 143, 29–36.

Hänsel P, Schindewolf M, Eltner A, et al. (2016). Feasibility of high-resolution soil erosion measurements by means of rainfall simulations and SfM photogrammetry. Hydrology 3(4): 38.

Haughton, N., Abramowitz, G., De Kauwe, M.G., Pitman, A.J. (2018). Does predictability of fluxes vary between FLUXNET sites? Biogeosciences 15, 4495–4513.

Hegarty, C. J., & Chatre, E. (2008). Evolution of the global navigation satellite system (gnss). Proceedings of the IEEE, 96(12), 1902-1917.

Hellesen, T.; Matikainen, L. (2013). An Object-Based Approach for Mapping Shrub and Tree Cover on Grassland Habitats by Use of LiDAR and CIR Orthoimages. Remote Sens. 2013, 5, 558–583.

Hofmann-Wellenhof, B., Lichtenegger, H., & Wasle, E. (2007). GNSS–global navigation satellite systems: GPS, GLONASS, Galileo, and more. Springer Science & Business Media.

Houérou, H.N.L. (2006). Agroforestry and sylvopastoralism: The role of trees and shrubs (Trubs) in range rehabilitation and development. Sci. Chang. Planétaires Sécher. 2006, 17, 343–348

Howard, J.; Merrifield, M. (2010). Mapping Groundwater Dependent Ecosystems in California. PLoS ONE 2010, 5, e11249.

Huang, Y. M., Liu, D., & An., S.S. (2015). Effects of slope aspect on soil nitrogen and microbial properties in the Chinese Loess region. Catena, 125, 135-145.

Huang, J., Yu, H., Guan, X., Wang, G., & Guo, R. (2016). Accelerated dryland expansion under climate change. Nature Climate Change, 6(2), 166–171.

Isard, S. A. (1986). Factors influencing soil moisture and plant community distribution on Niwot Ridge, Front Range, Colorado, USA. Arctic and Alpine Research, 18(1), 83-96.

IUSS Working Group WRB. (2006). World Reference Base for Soil Resources 2006. World Soil Resources Reports No. 103. Rome, Italy: FAO.

Jackson, R.B.; Canadell, J.; Ehleringer, J.R.; Mooney, H.A.; Sala, O.E.; Schulze, E.D. (1996). A global analysis of root distributions for terrestrial biomes. Oecologia 1996, 108, 389–411.

James, M. R., & Robson, S. (2014). Mitigating systematic error in topographic models derived from UAV and ground-based image networks. Earth Surface Processes and Landforms, 39(10), 1413-1420.

James, M.R. & Robson, S. (2012). Straightforward reconstruction of 3D surfaces and topography with a camera: Accuracy and geoscience application. Journal of Geophysical Research: Earth Surface 117(3): 1–17.

James, M.R. & Robson, S. (2014). Mitigating systematic error in topographic models derived from UAV and ground-based image networks. Earth Surface Processes and Landforms 39(10): 1413–1420.

James, M.R., Robson, S., D'Oleire-Oltmanns, S, et al. (2017a). Optimising UAV topographic surveys processed with structure-from-motion: Ground control quality, quantity and bundle adjustment. Geomorphology 280: 51–66.

James, M.R., Robson, S., & Smith, M.W. (2017b). 3-D uncertainty-based topographic change detection with structure-from-motion photogrammetry: Precision maps for ground control and directly georeferenced surveys. Earth Surface Processes and Landforms 42(12): 1769–1788.

Vandoninck, J., Jan Peters, Bernard De Baets, Eva M. De Clercq, Els Ducheyne, Niko E.C. Verhoest. (2011). The potential of multitemporal Aqua and Terra MODIS apparent thermal inertia as a soil moisture indicator. International Journal of Applied Earth Observation and Geoinformation 13.6 (2011): 934-941.

Jester W and Klik A (2005). Soil surface roughness measurement - methods, applicability, and surface representation. CATENA 64(2): 174–192. Kolzenburg S, Favalli M, Fornaciai A, et al. (2016) Rapid updating and improvement of airborne LIDAR DEMs through ground-based SfM 3-D modeling of volcanic features. IEEE Transactions on Geoscience and Remote Sensing 54(11): 6687–6699.

Jordan, G. (2003). Morphometric analysis and tectonic interpretation of digital terrain data: A case study. Earth Surf. Process. Landf. 2003, 28, 807–822.

Jung, P., Baumann, K., Lehnert, L. W., Samolov, E., Achilles, S., Schermer, M., Wraase, L.M., Eckhardt K-W., Bader, M.Y., Leinweber, P., Karsten, U., Bendix, Bendix, J. & Karsten, U. (2020). Desert breath—How fog promotes a novel type of soil biocenosis, forming the coastal Atacama Desert's living skin. Geobiology, 18(1), 113-124.

Kalkhan, M.A.; Stafford, E.J.; Stohlgren, T.J. (2007). Rapid plant diversity assessment using a pixel nested plot design: A case study in Beaver Meadows, Rocky Mountain National Park, Colorado, USA. Divers. Distrib. 2007, 13, 379–388.

Kallio, T. (1971). Protection of spruce stumps against Fomes annosus (Fr.) Cooke by some wood-inhabiting fungi. Acta For. Fenn. 1971, 117, 1–20.

Karnieli, A. (1997). Development and implementation of spectral crust index over dune sands. Int. J. Remote Sens. 1997, 18, 1207–1220.

Karnieli, A.; Sarafis, V. (1996). Reflectance spectrophotometry of cyanobacteria within soil crusts—A diagnostic tool. Int. J. Remote Sens. 1996, 17, 1609–1614.

Karnieli, A., & Tsoar, H. (1995). Spectral reflectance of biogenic crust developed on desert dune sand along the Israel-Egypt border. Remote Sensing, 16(2), 369-374.

Kaouthar, J., & Chaieb, M. (2009). The effect of Stipa tenacissima tussocks on some soil surface properties under arid bioclimate in the southern Tunisia. Acta botanica gallica, 156(2), 173-181

Kavzoglu, T.; Tonbul, H. (2017). A comparative study of segmentation quality for multi-resolution segmentation and watershed transform. In Proceedings of the 2017 8th International Conference on Recent Advances in Space Technologies (RAST), Istanbul, Turkey, 19–22 June 2017; pp. 113–117.

Kavzoglu, T.; Yildiz, M. (2014). Parameter-based performance analysis of object-based image analysis using aerial and Quikbird-2 images. ISPRS Ann. Photogramm. Remote Sens. Spat. Inf. Sci. 2014, 2, 31.

Kéfi, S.; Rietkerk, M.; Alados, C.L.; Pueyo, Y.; Papanastasis, V.P.; ElAich, A.; de Ruiter, P.C. (2007). Spatial vegetation patterns and imminent desertification in Mediterranean arid ecosystems. Nature 2007, 449, 213–217.

Keshava, N.; Mustard, J.F. (2002). Spectral unmixing. IEEE Signal Proc. 2002, 19, 44–57.

Kidron, G. J. (2019). The enigmatic absence of cyanobacterial biocrusts from the Namib fog belt: Do dew and fog hold the key?. Flora, 257, 151416.

Koutroulis, A. G. (2018). Dryland changes under different levels of global warming. Science of The Total Environment, 655, 482-511.

Kumar, S.; Simonson, S.; Stohlgren, T.J. (2009). Effects of spatial heterogeneity on butterfly species richness in Rocky Mountain National Park, CO, USA. Biodiv. Conserv. 2009, 18, 739–763.

Kutiel, P., Lavee, H., & Ackermann, O. (1998). Spatial distribution of soil surface coverage on north and south facing hillslopes along a Mediterranean to extreme arid climatic gradient. Geomorphology, 23(2-4), 245-256.

Ladrón de Guevara, M.; Gozalo, B.; Raggio, J.; Lafuente, A.; Prieto, M.; Maestre, F.T. (2018). Warming reduces the cover, richness and evenness of lichen-dominated biocrusts but promotes moss growth: Insights from an 8 yr experiment. New Phytol. 2018, 220, 811–823.

Laliberte, A.S.; Browning, D.M.; Rango, A. (2012). A comparison of three feature selection methods for object-based classification of sub-decimeter resolution UltraCam-L imagery. Int. J. Appl. Earth Obs. Geoinf. 2012, 15, 70–78.

Laliberte, A.S.; Rango, A. (2009). Texture and Scale in Object-Based Analysis of Subdecimeter Resolution Unmanned Aerial Vehicle (UAV) Imagery. IEEE Trans. Geosci. Remote Sens. 2009, 47, 761–770.

Laliberte, A.S.; Rango, A.; Havstad, K.M.; Paris, J.F.; Beck, R.F.; McNeely, R.; Gonzalez, A.L. (2004). Object-oriented image analysis for mapping shrub encroachment from 1937 to 2003 in southern New Mexico. Remote Sens. Environ. 2004, 93, 198–210.

Lange, O. L., Belnap, J., Reichenberger, H., & Meyer, A. (1997). Photosynthesis of green algal soil crust lichens from arid lands in southern Utah, USA: role of water content on light and temperature responses of CO2 exchange. Flora, 192(1), 1-15.

Lázaro R, Cantón Y, Solé-Benet A, Bevan J, Alexander R, Sancho LG, Puigdefábregas J (2008). The influence of competition between lichen colonization and erosion on the evolution of soil surfaces in the badlands (SE Spain) and its landscape effects. Geomorphology, 102, 252–266.

Leonard, J.A.; Yeary, R.A. (1990). Exposure of Workers Using Hand-Held Equipment During Urban Application of Pesticides to Trees and Ornamental Shrubs. Am. Ind. Hyg. Assoc. J. 1990, 51, 605–609.

Li, X. R., He, M. Z., Zerbe, S., Li, X. J., & Liu, L. C. (2010). Micro-geomorphology determines community structure of biological soil crusts at small scales. Earth Surface Processes and Landforms, 35(8), 932-940.

Liu, Y.; Bian, L.; Meng, Y.; Wang, H.; Zhang, S.; Yang, Y.; Shao, X.; Wang, B. (2012). Discrepancy measures for selecting optimal combination of parameter values in object-based image analysis. ISPRS J. Photogramm. Remote Sens. 2012, 68, 144–156.

Lomolino, M. V. (2001). Elevation gradients of species-density: historical and prospective views. Global Ecology and biogeography, 10(1), 3-13.

Lowe, D. G. (2004). Distinctive image features from scale-invariant keypoints. International journal of computer vision, 60(2), 91-110.

Lucieer A, de Jong SM and Turner D (2014). Mapping landslide displacements using Structure from Motion (SfM) and image correlation of multi-temporal UAV photography. Progress in Physical Geography 38(1): 97–116

Lucieer, A., Turner, D., King, D. H., & Robinson, S. A. (2014). Using an Unmanned Aerial Vehicle (UAV) to capture micro-topography of Antarctic moss beds. International journal of applied earth observation and geoinformation, 27, 53-62.

Ludwig, J.A.; Wilcox, B.P.; Breshears, D.D.; Tongway, D.J.; Imeson, A.C. (2005). Vegetation Patches and Runoff–Erosion as Interacting Ecohydrological Processes in Semiarid Landscapes. Ecology 2005, 86, 288–297.

Ludwig, J.A., Tongway, D.J., Freudenberger, D.O., Noble, J.C., Hodgkinson, K.C. (Eds.), 1997. Landscape Ecology, Function and Management: Principles from Australia's Rangelands. CSIRO Publishing, Melbourne, Australia.

Ma, C., Wang, W., Han, X., & Li, X. (2013). Soil moisture retrieval in the Heihe River Basin based on the real thermal inertia method. IEEE Journal of Selected Topics in Applied Earth Observations and Remote Sensing, 6(3), 1460-1467.

Maestre, F. T., Bautista, S., Cortina, J., & Bellot, J. (2001). Potential for using facilitation by grasses to establish shrubs on a semiarid degraded steppe. Ecological Applications, 11(6), 1641-1655.

Maestre, F. T., & Cortina, J. (2002). Spatial patterns of surface soil properties and vegetation in a Mediterranean semi-arid steppe. Plant and soil, 241(2), 279-291.

Maestre, F.T.; Escolar, C.; Bardgett, R.D.; Dungait, J.A.J.; Gozalo, B.; Ochoa, V. (2015). Warming reduces the cover and diversity of biocrust-forming mosses and lichens, and increases the physiological stress of soil microbial communities in a semi-arid Pinus halepensis plantation. Front. Microbiol. 2015, 6, 865.

Maestre FT, Escolar C, Ladrón de Guevara M, Quero JL, Lázaro R, Delgado- Baquerizo M, Ochoa V, Berdugo M, Gozalo B, Gallardo A. (2013). Changes in biocrust cover drive carbon cycle responses to climate change in drylands. Global Change Biology 19: 3835–3847

Maestre, F.T.; Escudero, A.; Martinez, I.; Guerrero, C.; Rubio, A. (2005). Does spatial pattern matter to ecosystem functioning? Insights from biological soil crusts. Funct. Ecol. 2005, 19, 566–573.

Maestre, F.T.; Escolar, C.; Ladrón de Guevara, M.; Quero, J.L.; Lázaro, R.; Delgado-Baquerizo, M.; Ochoa, V.; Berdugo, M.; Gozalo, B.; Gallardo, A. (2013). Changes in biocrust cover drive carbon cycle responses to climate change in drylands. Glob. Chang. Biol. 2013, 19, 3835–3847.

Maksymiuk, O.; Schmitt, M.; Auer, S.; Stilla, U. (2014). Single tree detection in millimeter wave SAR data by morphological attribute filters. Proc. Jahrestag. DGPF 2014, 34.

Mahlknecht, J.; Merchán, D.; Rosner, M.; Meixner, A.; Ledesma-Ruiz, R. (2017). Assessing seawater intrusion in an arid coastal aquifer under high anthropogenic influence using major constituents, Sr and B isotopes in groundwater. Sci. Total Environ. 2017, 587, 282–295.

Manzoni, S., Porporato, A., & D'Odorico, P. (2006). Modeling of carbon and nitrogen cycling in arid and semiarid ecosystems. In Dryland Ecohydrology (pp. 183-199). Springer, Dordrecht.

Måren, I.E., Karki, S., Prajapati, C., Yadav, R.K., Shrestha, B.B. (2015). Facing north or south: Does slope aspect impact forest stand characteristics and soil properties in a semiarid trans-Himalayan valley? J. Arid Environ. 121, 112–123.

Martín-Rosales, W.; Gisbert, J.; Pulido-Bosch, A.; Vallejos, A.; Fernández-Cortés, A. (2007). Estimating groundwater recharge induced by engineering systems in a semiarid area (southeastern Spain). Environ. Geol. 2007, 52, 985–995.

Martínez-Lage, A.V. (1997). Las extracciones de áridos en el litoral de almería para su utilización en la agricultura intensiva (1956-1997). In Proceedings of the Actas de Las Jornadas Sobre el Litoral de Almería: Caracterización, Ordenación y Gestión de un Espacio Geográfico Celebradas, Andalusia, Spain, 20–24 May 1997; Instituto de Estudios Almerienses: Andalusia, Spain, 1999; pp. 83–110.

Martínez-Sánchez, J. J., Casares-Porcel, M., Guerra, J., Gutiérrez-Carretero, L., Ros, R. M., Hernández-Bastida, J., & Cano, M. J. (1994). A special habitat for bryophytes and lichens in the arid zones of Spain. Lindbergia, 116-121.

Mathews AJ and Jensen JLR (2013). Visualizing and quantifying vineyard canopy LAI usinganunmanned aerial vehicle (UAV) collected high density structure from motion point cloud. Remote Sensing 5(5): 2164–2183.

Mendoza-Fernández, A.J.; Martínez-Hernández, F.; Pérez-García, F.J.; Garrido-Becerra, J.A.; Benito, B.M.; Salmerón-Sánchez, E.; Guirado, J.; Merlo, M.E.; Mota, J.F. (2015). Extreme habitat loss in a Mediterranean habitat: Maytenus senegalensis subsp. europaea. Plant Biosyst.-Int. J. Deal. Asp. Plant Biol. 2015, 149, 503–511.

Micheletti N, Chandler JH and Lane SN (2015). Structure from motion (SFM) photogrammetry. In: Clarke LE and Nield JM (eds.) Geomorphological Techniques (Online Edition). London: British Society for Geomorphology

Middleton, N.J. & Thomas, D.S.G. (1997). Middleton, N.J. & Thomas, D.S.G. Eds., World Atlas of Desertification (U.N. Environment Programme, Edward Arnold, New York, ed. 2, 1997).

Milling, C. R., Rachlow, J. L., Olsoy, P. J., Chappell, M. A., Johnson, T. R., Forbey, J. S., Shipley, L.A. & Thornton, D. H. (2018). Habitat structure modifies microclimate: An approach for mapping fine-scale thermal refuge. Methods in Ecology and Evolution, 9(6), 1648-1657.

Minacapilli, M., Iovino, M., & Blanda, F. (2009). High resolution remote estimation of soil surface water content by a thermal inertia approach. Journal of hydrology, 379(3-4), 229-238.

Minasny, B., Setiawan, B.I., Saptomo, S.K., McBratney, A.B. (2018). Open digital mapping as a cost-effective method for mapping peat thickness and assessing the carbon stock of tropical peatlands. Geoderma 2018, 313, 25–40.

Miralles, I., Lázaro, R., Sánchez-Marañón, M., Soriano, M., & Ortega, R. (2020). Biocrust cover and successional stages influence soil bacterial composition and diversity in semiarid ecosystems. Science of The Total Environment, 709, 134654

Mitra, D.S., & Majumdar, T.J. (2004). Thermal inertia mapping over the Brahmaputra basin, India using NOAA-AVHRR data and its possible geological applications. International Journal of Remote Sensing 25.16 (2004): 3245-3260.

Monteith, J.L., Szeicz, G. (1962). Radiative temperature in the heat balance of natural surfaces. Quarterly Journal of the Royal Meteorological Society 88: 496–507.

Murray, H.; Lucieer, A.; Williams, R. (2010). Texture-based classification of sub-Antarctic vegetation communities on Heard Island. Int. J. Appl. Earth Obs. Geoinf. 2010, 12, 138–149.

Nagendra, H. Using remote sensing to assess biodiversity. Int. J. Remote Sens. 2001, 22, 2377–2400.

Nègre, R. (1959). Recherches Phytogéographiques Sur L'étage de Végétation Méditerranéen Aride (Sous-Étage Chaud) au Maroc Occidental; Société des Sciences Naturelles et Physiques du Maroc: Rabat, Morocco, 1959.

Niethammer, U., James, M. R., Rothmund, S., Travelletti, J., & Joswig, M. (2012). UAV-based remote sensing of the Super-Sauze landslide: Evaluation and results. Engineering Geology, 128, 2-11.

Nouwakpo SK, Weltz MA and McGwire K (2016) Assessing the performance of structure-from-motion photogrammetry and terrestrial LiDAR for reconstructing soil surface microtopography of naturally vegetated plots. Earth Surface Processes and Landforms 41(3): 308–322. O'Callaghan JF and Mark DM (1989) The extraction of drainage networks from digital elevation data. Computer Vision, Graphics and Image Processing 28(1): 323–344.

Nussbaum, S.; Menz, G. (2088). SEaTH–A New Tool for Feature Analysis. In Object-Based Image Analysis and Treaty Verification: New Approaches in Remote Sensing–Applied to Nuclear Facilities in Iran; Nussbaum, S., Menz, G., Eds.; Springer: Dordrecht, The Netherlands, 2008; pp. 51–62.

O'Connor, J., Smith, M.J. & James, M.R. (2017). Cameras and settings for aerial surveys in the geosciences: Optimising image data. Progress in Physical Geography 41(3): 325–344.

O'Neill, A.L. (1994). Reflectance spectra of microphytic soil crusts in semiarid Australia. Int. J. Remote Sens. 1994, 15, 675–681.

Okin, G. S., Heras, M. M. Las., Saco, P. M., Throop, H. L., Vivoni, E. R., Parsons, A. J., … Peters, D. P. (2015). Connectivity in dryland landscapes: Shifting concepts of spatial interactions. Frontiers in Ecology and the Environment, 13, 20–27

Oksanen, J.; Blanchet, F.G.; Kindt, R.; Legendre, P.; O'Hara, R.B.; Simpson, G.L.; Solymos, P.; Stevens, M.H.H.; Wagner, H. (2017). Vegan: Community Ecology Package. R Package Version 2.4-5 (R Foundation for Statistical Computing, Vienna). 2017. Available online: https://CRAN.R-project.org/package=vegan (accessed on 15 June 2019).

Ota, T., Ogawa, M., Shimizu, K. et al. (2015). Above- ground biomass estimation using structure from motion approach with aerial photographs in a seasonal tropical forest. Forests 6(11): 3882–3898.

Oyonarte, C.; Rey, A.; Raimundo, J.; Miralles, I.; Escribano, P. (2012). The use of soil respiration as an ecological indicator in arid ecosystems of the SE of Spain: Spatial variability and controlling factors. Ecol. Indic. 2012, 14, 40–49.

Palmer, M.W., Earls, P., Hoagland, B.W., White, P.S. & Wohlgemuth, T. (2002). Quantitative tools for perfecting species lists. Environmetrics 2002, 13, 121–137.

Panigada, C., Tagliabue, G., Zaady, E., Rozenstein, O., Garzonio, R., Di Mauro, B., De Amicis, M., Colombo, R., Cogliati, S., Miglietta, F. & Rossini, M. (2019). A new approach for biocrust and vegetation monitoring in drylands using multi-temporal Sentinel-2 images. Progress in Physical Geography: Earth and Environment, 43(4), 496-520.

Partridge, T.R. (1992). Vegetation recovery following sand mining on coastal dunes at Kaitorete Spit, Canterbury, New Zealand. Biol. Conserv. 1992, 61, 59–71.

Pearson, E. S. (1926). Review of statistical methods for research workers (RA Fisher). Science Progress, 20, 733-734.

Plaza, A., Benediktsson, J.A., Boardman, J.W., Brazile, J., Bruzzone, L., Camps-Valls, G., Chanussot, J., Fauvel, M., Gamba, P. & Gualtieri, A. (2009). Recent advances in techniques for hyperspectral image processing. Remote Sens. Environ. 2009, 113, 110–122.

Pearson, E. S. (1926). Review of statistical methods for research workers (RA Fisher). Science Progress, 20, 733-734.

Peet, R.K. (1974). The measurement of species diversity. Ann. Rev. Ecol. Syst. 1974, 5, 285–307.

Pettorelli, N., Safi, K., Turner,W. & Pettorelli, N. (2014). Satellite remote sensing, biodiversity research and conservation of the future. Philos. Trans. R. Soc. B 2014, 369, 20130190.

Pharo, E. J., & Beattie, A. J. (1997). Bryophyte and lichen diversity: a comparative study. Australian Journal of Ecology, 22(2), 151-162.

Pielou, E.C. (1966). The measurement of diversity in different types of biological collections. J. Theor. Biol. 1966, 13, 131–144.

Pintado, A., Sancho, L. G., Green, T. G., Blanquer, J. M., & Lázaro, R. (2005). Functional ecology of the biological soil crust in semiarid SE Spain: sun and shade populations of Diploschistes diacapsis (Ach.) Lumbsch.

Plaza, A., Benediktsson, J. A., Boardman, J. W., Brazile, J., Bruzzone, L., Camps-Valls, G., Chanussot, J., Fauvel, M., Gamba, P., Gaultieri, A., Marconcini, M., Tilton, J.C. & Marconcini, M. (2009). Recent advances in techniques for hyperspectral image processing. Remote sensing of environment, 113, S110-S122.

Prăvălie, R. (2016). Drylands extent and environmental issues. A global approach. Earth-Science Reviews, 161, 259-278.

Ponce, V.M. (2014). Effect of groundwater pumping on the health of arid vegetative ecosystems. Online Report, December. 2014. Available online: http://ponce.sdsu.edu/effect_of_groundwater_pumping.html (accessed on 10 November 2019).

Price, J.C. (1985). On the analysis of thermal infrared imagery: The limited utility of apparent thermal inertia. Remote Sens. Environ. 18:59–73.

Pugnaire, F.I., Armas, C. & Maestre, F.T. (2011). Positive plant interactions in the Iberian Southeast: Mechanisms, environmental gradients, and ecosystem function. J. Arid Environ. 2011, 75, 1310–1320.

Puigdefábregas, J. (2005). The role of vegetation patterns in structuring runoff and sediment fluxes in drylands. Earth Surf. Process. Landf. 2005, 30, 133–147.

Puigdefábregas, J. & Sánchez, G. (1996) Geomorphological implications of vegetation patchiness on semi-arid slopes. Advances on Hillslope Processes (eds Anderson, M.G. & Brooks, S.M.), pp. 1027–1060. John Wiley and Sons, Chichester, UK

Puigdefábregas, J., Sole, A., Gutierrez, L., Del Barrio, G., & Boer, M. (1999). Scales and processes of water and sediment redistribution in drylands: results from the Rambla Honda field site in Southeast Spain. Earth-Science Reviews, 48(1-2), 39-70.

Qin, Z., Li, W., Burgheimer, J., & Karnieli, A. (2006). Quantitative estimation of land cover structure in an arid region across the Israel–Egypt border using remote sensing data. Journal of arid environments, 66(2), 336-352.

Raggio, J., Green, T. A., Pintado, A., Sancho, L. G., & Büdel, B. (2018). Environmental determinants of biocrust carbon fluxes across Europe: possibilities for a functional type approach. Plant and Soil, 429(1-2), 147-157.

Raggio, J., Pintado, A., Vivas, M., Sancho, L. G., Büdel, B., Colesie, C., Weber, B., Schroeter, B., Lázaro, R. & Green, T. G. A. (2014). Continuous chlorophyll fluorescence, gas exchange and microclimate monitoring in a natural soil crust habitat in Tabernas badlands, Almería, Spain: progressing towards a model to understand productivity. Biodiversity and Conservation, 23(7), 1809-1826.

Ravi, S., D'Odorico, P., Breshears, D.D., Field, J.P., Goudie, A.S., Huxman, T.E., Li, J., Okin, G.S., Swap, R.J., Thomas, A.D., Van Pelt. S., Whicker, J.J. & Zobeck, T.M. (2011). Aeolian processes and the biosphere. Rev Geophys 49:RG3001.

Read, C. F., Elith, J., & Vesk, P. A. (2016). Testing a model of biological soil crust succession. Journal of vegetation science, 27(1), 176-186.

Reed, S.C., Maestre, F.T., Ochoa-Hueso, R., Kuske, C.R., Darrouzet-Nardi, A., Oliver, M., Darby, B., Sancho, L.G., Sinsabaugh, R.L., Belnap, J. (2016). Biocrusts in the Context of Global Change. In Biological Soil Crust: An Organizing Principle in Drylands, 1st ed.; Weber, B., Büdel, B., Belnap, J., Eds.; Ecological Studies; Springer: Berlin, Germany, 2016; Volume 226, pp. 451–476.

Rees, W.G., Tutubalina, O.V. & Golubeva, E.I. (2004). Reflectance spectra of subarctic lichens between 400 and 2400 nm. Remote Sens. Environ. 2004, 90, 281–292.

Reid, I. (1973). The influence of slope orientation upon the soil moisture regime, and its hydrogeomorphological significance. Journal of Hydrology, 19(4), 309-321.

Renard KG, Foster GR, Weesies GA, McCool DK, Yoder DC. (1997). Predicting Soil Erosion by Water: A guide to conservation planning with the revised universal soil loss equation (RUSLE). U.S. Department of Agriculture, Agriculture Handbook No. 703.

Rey, P.J., Cancio, I., Manzaneda, A.J., González-Robles, A., Valera, F., Salido, T. & Alcántara, J.M. (2018). Regeneration of a keystone semiarid shrub over its range in Spain: Habitat degradation overrides the positive effects of plant–animal mutualisms. Plant Biol. 2018, 20, 1083–1092.

Reynolds, J. F., Smith, D. M. S., Lambin, E. F., Turner, B. L., Mortimore, M., Batterbury, S. P., Downing, T.E., Dowlatabadi, H., Fernández, R.J., Herrick, J.E., Huber-Sannwald, E., Jiang, H., Leemans, R., Lynam, T., Maestre, F.T., Ayarza, M. & Walker, B. (2007). Global desertification: building a science for dryland development. Science, 316(5826), 847-851.

Reynolds, J. F., Virginia, R. A., Kemp, P. R., De Soyza, A. G., & Tremmel, D. C. (1999). Impact of drought on desert shrubs: Effects of seasonality and de- gree of resource island development. Ecological Monographs, 69, 69–106Ricotta, C.; Avena, G.C.; Volpe, F. The influence of principal component analysis on the spatial structure of a multispectral dataset. Int. J. Remote Sens. 1999, 20, 3367–3376.

Ridolfi, L., Laio, F., & D'Odorico, P. (2008). Fertility island formation and evolution in dryland ecosystems. Ecology and Society, 13(1).

Rigol-Sanchez, J.P., Stuart, N., Pulido-Bosch, A. (2015). ArcGeomorphometry: A toolbox for geomorphometric characterisation of DEMs in the ArcGIS environment. Comput. Geosci. 2015, 85, 155–163.

Rivas Goday, S., Bellot, F. (1944). Las formaciones de Ziziphus lotus (L.) Lamk. en las dunas del Cabo de Gata. An. Inst. Esp. Edafol. Ecol. Fisiol. Veg. 1944, 3, 109–126.

Rocchini, D., Balkenhol, N., Carter, G.A., Foody, G.M., Gillespie, T.W., He, K.S., Kark, S., Levin, N., Lucas, K., Luoto, M. et al. (2010). Remotely sensed spectral heterogeneity as a proxy of species diversity: Recent advances and open challenges. Ecol. Inform. 2010, 5, 318–329

Rocchini, D., Boyd, D.S., Féret, J.B., Foody, G.M., He, K.S., Lausch, A., Nagendra, H., Wegmann, M. & Pettorelli, N. (2015). Satellite remote sensing to monitor species diversity: Potential and pitfalls. Remote Sens. Ecol. Conserv. 2015, 2, 25–36.

Rodríguez-Caballero, E., Aguilar, M. Á., Castilla, Y. C., Chamizo, S., & Aguilar, F. J. (2015). Swelling of biocrusts upon wetting induces changes in surface micro-topography. Soil Biology and Biochemistry, 82, 107-111.

Rodríguez-Caballero, E., Belnap, J., Büdel, B., Crutzen, P.J., Andreae, M.O., Pöschl, U. &Weber, B. (2018). Dryland photoautotrophic soil surface communities endangered by global change. Nat. Geosci. 2018, 11, 185–189.

Rodríguez-Caballero, E., Castro, A.J., Chamizo, S., Quintas-Soriano, C., Garcia-Llorente, M., Cantón, Y. & Weber, B. (2018). Ecosystem services provided by biocrusts: From ecosystem functions to social values. J. Arid Environ. 2018, 159, 45–53.

Rodríguez-Caballero, E., Cantón, Y., Chamizo, S., Lázaro, R., & Escudero, A. (2013). Soil loss and runoff in semiarid ecosystems: a complex interaction between biological soil crusts, micro-topography, and hydrological drivers. Ecosystems, 16(4), 529-546.

Rodríguez-Caballero, E., Escribano, P., & Cantón, Y. (2014). Advanced image processing methods as a tool to map and quantify different types of biological soil crust. ISPRS Journal of Photogrammetry and Remote Sensing, 90, 59-67.

Rodríguez-Caballero, E., Paul, M., Tamm, A., Caesar, J., Büdel, B., Escribano, P., Hill, J. & Weber, B. (2017). Biomass assessment of microbial surface communities by means of hyperspectral remote sensing data. Sci. Total Environ. 2017, 586, 1287–1297.

Rodríguez-Caballero, E., Román, J. R., Chamizo, S., Roncero Ramos, B., & Cantón, Y. (2019). Biocrust landscape-scale spatial distribution is strongly controlled by terrain attributes: Topographic thresholds for colonization in a semiarid badland system. Earth Surface Processes and Landforms, 44(14), 2771-2779.

Román, J.R., Rodríguez-Caballero, E., Rodríguez-Lozano, B., Roncero-Ramos, B., Chamizo, S., Águila-Carricondo, P. & Cantón, Y. (2019). Spectral Response Analysis: An Indirect and Non-Destructive Methodology for the Chlorophyll Quantification of Biocrusts. Remote Sens. 2019, 11, 1350.

Rose, R. A., Byler, D., Eastman, J. R., Fleishman, E., Geller, G., Goetz, S., et al. (2015). Ten ways remote sensing can contribute to conservation. Conservation Biology, 29(2), 350-359.

Rose, J.C., Paulus, S. & Kuhlmann, H. (2015). Accuracy analysis of a multi-view stereo approach for phenotyping of tomato plants at the organ level. Sensors (Switzerland) 15(5): 9651–9665

Rosenberg, M.S.; Anderson, C.D. (2011). PASSaGE: Pattern Analysis, Spatial Statistics and Geographic Exegesis. Version 2. Methods Ecol. Evol. 2011, 2, 229–232.

Roques, K.G.; O'connor, T.G.; Watkinson, A.R. (2001). Dynamics of shrub encroachment in an African savanna: Relative influences of fire, herbivory, rainfall and density dependence. J. Appl. Ecol. 2001, 38, 268–280.

Rozenstein, O. & Karnieli, A. (2015). Identification and characterization of Biological Soil Crusts in a sand dune desert environment across Israel–Egypt border using LWIR emittance spectroscopy. J. Arid Environ. 2015, 112, 75–86.

Sánchez, F.J.T. (2008). El uso del agua en Nijar: Implicaciones ambientales del modelo actual de gestión. Rev. Estud. Reg. 2008, 83, 145–176.

Sankey, T. T., McVay, J., Swetnam, T. L., McClaran, M. P., Heilman, P., & Nichols, M. (2018). UAV hyperspectral and lidar data and their fusion for arid and semi-arid land vegetation monitoring. Remote Sensing in Ecology and Conservation, 4(1), 20-33.

Savitzky, A.; Golay, M.J.E. (1964). Smoothing and differentiation of data by simplified least squares procedures. Anal. Chem. 1964, 36, 1627–1639.

Schäfer, E., Heiskanen, J., Heikinheimo, V., Pellikka, P. (2016). Mapping tree species diversity of a tropical montane forest by unsupervised clustering of airborne imaging spectroscopy data. Ecol. Indic. 2016, 64, 49–58.

Schiewe, J., Tufte, L. & Ehlers, M. (2016). Potential and problems of multi-scale segmentation methods in remote sensing. GeoBIT/GIS 2001, 6, 34–39.

Schumaker, N.H. (1996). Using Landscape Indices to Predict Habitat Connectivity. Ecology 1996, 77, 1210–1225.

Schweiger, A.K., Cavender-Bares, J., Townsend, P.A., Hobbie, S.E., Madritch, M.D.; Wang, R.; Tilman, D.; Gamon, J.A. (2018). Plant spectral diversity integrates functional and phylogenetic components of biodiversity and predicts ecosystem function. Nat. Ecol. Evol. 2018, 2, 976–982.

Schweiger, A. K., Cavender-Bares, J., Townsend, P. A., Hobbie, S. E., Madritch, M. D., Kothari, S., Grossman, J.J., Gholizadeh, H., Wang, R. & Gamon, J. A. (2020). Spectral niches reveal taxonomic identity and complementarity in plant communities. bioRxiv.

Schweiger, A. K., Schütz, M., Risch, A. C., Kneubühler, M., Haller, R., & Schaepman, M. E. (2017). How to predict plant functional types using imaging spectroscopy: linking vegetation community traits, plant functional types and spectral response. Methods in Ecology and Evolution, 8(1), 86–95.

Sedia, E. G., & Ehrenfeld, J. G. (2006). Differential effects of lichens and mosses on soil enzyme activity and litter decomposition. Biology and Fertility of Soils, 43(2), 177-189.

Sevgi, E., Yilmaz, O. Y., & Sevgi, O. (2020). Small-scale spatial patterns of two terricolous lichens in a conifer plantation. Applied ecology and environmental research. 18(2), 3557-3576.

Shahbazi M, Sohn G, The´au J, et al. (2015). UAV-based point cloud generation for open-pit mine modelling. International Archives of the Photogrammetry, Remote Sensing and Spatial Information Sciences – ISPRS Archives 40(1W4): 313–320.

Shannon, C.E. (1948). A mathematical theory of communication. Bell Syst. Tech. J. 1948, 27, 379–423.

Short, N. M., & Stuart, L. M. (1982). The heat capacity mapping mission (HCMM) anthology (Vol. 465). Scientific and Technical Information Branch, National Aeronautics and Space Administration.

Signorell, A.; Aho, K.; Alfons, A.; Anderegg, N.; Aragon, T.; Arppe, A.; Baddeley, A.; Barton, K.; Bolker, B.; Borchers, H.W.; et al. DescTools: Descriptive Tools Analysis. R Package Version 3.6.1 (R Foundation for Statistical Computing, Vienna). Available online: https://cran.r-project.org/web/packages/DescTools/index. html (accessed on 16 May 2019).

Silver, M., Tiwari, A., & Karnieli, A. (2019). Identifying Vegetation in Arid Regions Using Object-Based Image Analysis with RGB-Only Aerial Imagery. Remote Sensing, 11(19), 2308. https://doi.org/10.3390/rs11192308

Simpson, E.H. (1949). Measurement of diversity. Nature 1949, 163, 688.

Smith MW, Carrivick JL & Quincey DJ (2015). Structure from motion photogrammetry in physical geography. Progress in Physical Geography 40(2): 247–275.

Smith, W. K., Dannenberg, M. P., Yan, D., Herrmann, S., Barnes, M. L., Barron-Gafford, G. A., et al. (2019). Remote sensing of dryland ecosystem structure and function: Progress, challenges, and opportunities. Remote Sensing of Environment, 233, 111401.

Smith, G. M., & Milton, E. J. (1999). The use of the empirical line method to calibrate remotely sensed data to reflectance. International Journal of remote sensing, 20(13), 2653-2662.

Sola, F.; Daniele, L.; Sánchez Martos, F.; Vallejos, A.; Urízar, R.; Pulido Bosch, A. (2007). Influencia de la desaladora de Rambla Morales (Almería) sobre las características hidrogeológicas del acuífero del que se abastece. Los Acuíferos Costeros Retos Soluc. 2007, 1, 997–1004.

Somers, B.; Asner, G.P.; Tits, L.; Coppin, P. (2011). Endmember variability in Spectral Mixture Analysis: A review. Remote Sens. Environ. 2011, 115, 1603–1616.

Sörensen, R., Zinko, U., & Seibert, J. (2006). On the calculation of the topographic wetness index: evaluation of different methods based on field observations.

Stickler, C.M.; Southworth, J. (2008). Application of a multi-scale spatial and spectral analysis to predict primate occurrence and habitat associations in Kibale National Park, Uganda. Remote Sens. Environ. 2008, 112, 2170–2186.

Stieglitz M, Shaman J, McNamara J, et al. (2003). An approach to understanding hydrologic connectivity on the hillslope and the implications for nutrient transport. Global Biogeochemical Cycles 17(4): 1–15.

Stohlgren, T.J.; Chong, G.W.; Kalkhan, M.A.; Schell, L.D. (1997). Multiscale sampling of plant diversity: Effects of minimum mapping unit size. Ecol. Appl. 1997, 7, 1064–1074.

Story, M., & Congalton, R. G. (1986). Accuracy assessment: a user's perspective. Photogrammetric Engineering and remote sensing, 52(3), 397-399.

Sturm, M.; Racine, C.; Tape, K. (2001). Increasing shrub abundance in the Arctic. Nature 2001, 411, 546–547.

Suggitt AJ, Wilson RJ, Isaac NJB, Beale CM, Auffret AG, August T, Bennie JJ, Crick HQP, Duffield S, Fox R, Hopkins JJ, Macgregor NA, Morecroft MD, Walker KJ, Maclean IMD. (2018). Extinction risk from climate change is reduced by microclimatic buffering. Nature Climate Change 8: 713–717.

Tarboton, D. G. (1997). A new method for the determination of flow directions and upslope areas in grid digital elevation models. Water resources research, 33(2), 309-319.

Tengberg, A.; Chen, D. (1998). A comparative analysis of nebkhas in central Tunisia and northern Burkina Faso. Geomorphology 1998, 22, 181–192.

Tesfa, T. K., Tarboton, D. G., Watson, D. W., Schreuders, K. A., Baker, M. E., & Wallace, R. M. (2011). Extraction of hydrological proximity measures from DEMs using parallel processing. Environmental Modelling & Software, 26(12), 1696-1709.

Thompson, S.E.; Harman, C.J.; Troch, P.A.; Brooks, P.D.; Sivapalan, M. (2011). Spatial scale dependence of ecohydrologically mediated water balance partitioning: A synthesis framework for catchment ecohydrology. Water Resour. Res. 2011, 47.

Thompson, D. B., Walker, L. R., Landau, F. H., & Stark, L. R. (2005). The influence of elevation, shrub species, and biological soil crust on fertile islands in the Mojave Desert, USA. Journal of Arid Environments, 61(4), 609-629.

Tian, J.; Chen, D.-M. (2007). Optimization in multi-scale segmentation of high-resolution satellite images for artificial feature recognition. Int. J. Remote Sens. 2007, 28, 4625–4644.

Tilman, D.; Kareiva, P. (2018). Spatial Ecology: The Role of Space in Population Dynamics and Interspecific Interactions (MPB-30); Princeton University Press: Princeton, NJ, USA, 2018.

Tirado, R. (2009). 5220 Matorrales arborescentes con Ziziphus. VV AA Bases Ecológicas Prelim; Para Conserv. Los Tipos Hábitat Interés Comunitario En España; Dir. Gral. de Medio Natural; Ministerio de Medio Ambiente, y Medio Rural y Marino: Madrid, Spain, 2009.

Tirado, R.; Bråthen, K.A. & Pugnaire, F.I. (2015). Mutual positive effects between shrubs in an arid ecosystem. Sci. Rep. 2015, 5, 14710.

Tirado, R.; Pugnaire, F.I. (2003). Shrub spatial aggregation and consequences for reproductive success. Oecologia 2003, 136, 296–301.

Tongway, D.J.; Hindley, N. (2004). Landscape Function Analysis: Procedures for Monitoring and Assessing Landscapes; CSIRO Publishing: Brisbane, Australia, 2004; p. 82.

Tonkin TN & Midgley NG. (2016). Ground-control networks for image based surface reconstruction: An investigation of optimum survey designs using UAV derived imagery and structure-from-motion photogrammetry. Remote Sensing 8(9): 16–19.

Toth, C., & Jóźków, G. (2016). Remote sensing platforms and sensors: A survey. ISPRS Journal of Photogrammetry and Remote Sensing, 115, 22-36.

Tramutoli, V., Claps, P., Marella, M., Pergola, N., Sileo, C., (2000). Feasibility of hydrological application of thermal inertia from remote sensing. In: Proc. of 2nd Plinius Conference on Mediterranean Storms, Siena, Italy, 16–18 October 2000

Tsai, Y.; Stow, D.; Chen, H.; Lewison, R.; An, L.; Shi, L. (2018). Mapping vegetation and land use types in fanjingshan national nature reserve using Google Earth Engine. Remote Sens. 2018, 10, 927.

Tsygankov, A. A. (2007). Nitrogen-fixing cyanobacteria: a review. Applied biochemistry and microbiology, 43(3), 250-259.

Tucker, C. L., Ferrenberg, S., & Reed, S. C. (2019). Climatic sensitivity of dryland soil CO_2 fluxes differs dramatically with biological soil crust successional state. Ecosystems, 22(1), 15-32.

Turner D, Lucieer A and Wallace L (2014). Direct georeferencing of ultrahigh-resolution UAV imagery. IEEE Transactions on Geoscience and Remote Sensing 52(5): 2738–2745

Turner, W.; Spector, S.; Gardiner, N.; Fladeland, M.; Sterling, E.; Steininger, M. (2003). Remote sensing for biodiversity science and conservation. Trends Ecol. Evol. 2003, 18, 306–314.

Ullman, S. (1983). The interpretation of structure from motion. Proceedings of the Royal Society of London. B, 203, 405-426.

Ustin, S.L.; Valko, P.G.; Kefauver, S.C.; Santos, M.J.; Zimpfer, J.F.; Smith, S.D. (2009). Remote sensing of biological soil crust under simulated climate change manipulations in the Mojave Desert. Remote Sens. Environ. 2009, 113, 317–328.

Vallet, J., Panissod, F., Strecha, C., Tracol, M. (2012). Photogrammetric performance of an ultra light weight swinglet 'UAV'. In: ISPRS – International Archives of the Photogrammetry, Remote Sensing and Spatial Information Sciences, XXXVIII- 1/C22, UAV-g 2011 Conference on Unmanned Aerial Vehicle in Geomatics, Zurich, Switzerland, pp. 253–258.

Van Cleemput, E., Roberts, D. A., Honnay, O., & Somers, B. (2019). A novel procedure for measuring functional traits of herbaceous species through field spectroscopy. Methods in Ecology and Evolution, 2019(May), 1332–1338.

Van Doninck, J., Peters, J., De Baets, B., De Clercq, E. M., Ducheyne, E., & Verhoest, N. E. C. (2011). The potential of multitemporal Aqua and Terra MODIS apparent thermal inertia as a soil moisture indicator. International Journal of Applied Earth Observation and Geoinformation, 13(6), 934–941.

Vapnik, B.V. (2005). Universal Learning Technology: Support Vector Machines. J. Adv. Technol. 2005, 2, 137–144. 49.

Verhoef, Anne. (2004). Remote estimation of thermal inertia and soil heat flux for bare soil. Agricultural and forest meteorology 123.3-4 (2004): 221-236.

Verhoeven, G. (2011). Taking computer vision aloft–archaeological three-dimensional reconstructions from aerial photographs with photoscan. Archaeological prospection, 18(1), 67-73.

Verstraeten, W. W., Veroustraete, F., van der Sande, C. J., Grootaers, I., & Feyen, J. (2006). Soil moisture retrieval using thermal inertia, determined with visible and thermal spaceborne data, validated for European forests. Remote Sensing of Environment, 101(3), 299-314.

Wallace L, Lucieer A, Malenovsky´ Z, et al. (2016) Assessment of forest structure using two UAV techniques: A comparison of airborne laser scanning and structure from motion (SfM) point clouds. Forests 7(3): 1–16.

Wang, R.; Gamon, J.A.; Cavender-Bares, J.; Townsend, P.A.; Zygielbaum, A.I. (2018). The spatial sensitivity of the spectral diversity-biodiversity relationship: An experimental test in a prairie grassland. Ecol. Appl. 2018a, 28, 541–556.

Wang, R.; Gamon, J.A.; Emmerton, C.A.; Li, H.; Nestola, E.; Pastorello, G.Z.; Menzer, O. (2016). Integrated analysis of productivity and biodiversity in a southern Alberta prairie. Remote Sens. 2016, 8, 214.

Wang, R.; Gamon, J.A.; Schweiger, A.K.; Cavender-Bares, J.; Townsend, P.A.; Zygielbaum, A.I.; Kothari, S. (2018). Influence of species richness, evenness, and composition on optical diversity: A simulation study. Remote Sens. Environ. 2018b, 211, 218–228

Wang, X.; Yang, F.; Yang, D.; Chen, X. (2013). Relationship between the growth of Tamarix ramosissima and morphology of nebkhas in oasis-desert ecotones. In Global Climate Change and Its Impact on Food & Energy Security in the Drylands, Proceedings of the Eleventh International Dryland Development Conference, Beijing, China, 18–21 March 2013; International Dryland Development Commission (IDDC): Beijing, China, 2014; pp. 616–628.

Wang, X.Z.; Ashfaq, R.A.R.; Fu, A.M. (2015). Fuzziness based sample categorization for classifier performance improvement. J. Intell. Fuzzy Syst. 2015, 29, 1185–1196.

Wang, L., Zhang, G., Zhu, L., & Wang, H. (2017). Biocrust wetting induced change in soil surface roughness as influenced by biocrust type, coverage and wetting patterns. Geoderma, 306, 1-9.

Waser, L.T.; Kuechler, M.; Schwarz, M.; Ivits, E.; Stofer, S.; Scheidegger, C. (2007). Prediction of lichen diversity in an UNESCO biosphere reserve—Correlation of high resolution remote sensing data with field samples. Environ. Model. Assess. 2007, 12, 315–328.

Watanachaturaporn, P.; Arora, M.K.; Varshney, P.K. (2005). Hyperspectral image classification using support vector machines: A comparison with decision tree and neural network classifiers. In Proceedings of the American Society for Photogrammetry & Remote Sensing (ASPRS) 2005 Annual Conference, Reno, NV, USA, 7–11 March 2005.

Weber, B., Büdel, B. & Belnap, J. (2016). Biological Soil Crusts: An Organizing Principle in Drylands, 1st ed.; Weber, B., Büdel, B., Belnap, J., Eds.; Ecological Studies; Springer: Berlin, Germany, 2016; Volume 226.

Weber, B.; Hill, J. (2016). Remote Sensing of Biological Soil Crusts at Different Scales. In Biological Soil Crust: An Organizing Principle in Drylands, 1st ed.; Weber, B., Büdel, B., Belnap, J., Eds.; Ecological Studies; Springer: Berlin, Germany, 2016; Volume 226, pp. 215–234.

Weber, B.; Olehowski, C.; Knerr, T.; Hill, J.; Deutschewitz, K.; Wessels, D.C.J.; Eitel, B.; Büdel, B. (2008). A new approach for mapping of Biological Soil Crusts in semidesert areas with hyperspectral imagery. Remote Sens. Environ. 2008, 112, 2187–2201.

Weber, B., Wu, D., Tamm, A., Ruckteschler, N., Rodriguez-Caballero, E., Steinkamp, J., Meusel, H., Elbert, W., Behrendt, T., Sörgel, M., Cheng, Y., Crutzen, P.J., Su, H. & Pöschl, U. (2015). Biological soil crusts accelerate the nitrogen cycle through large NO and HONO emissions in drylands. Proceedings of the National Academy of Sciences, 112(50), 15384-15389.

Weksler, S.; Rozenstein, O.; Ben-Dor, E. (2018). Mapping Surface Quartz Content in Sand Dunes Covered by Biological Soil Crusts Using Airborne Hyperspectral Images in the Longwave Infrared Region. Minerals 2018, 8, 318.

Westoby MJ, Brasington J, Glasser NF, et al. (2012) .'Structure-from-Motion' photogrammetry: A low-cost, effective tool for geoscience applications. Geomorphology 179: 300–314

Whitford, W., & Wade, E. L. (2002). Ecology of desert systems. Amsterdam, the Netherlands: Elsevier

Williams AJ, Buck BJ, Soukup DA, Merkler DJ. (2013). Geomorphic controls on biological soil crust distribution: a conceptual model from the Mojave Desert (USA). Geomorphology 195:99–109

Yu, Q.; Gong, P.; Clinton, N.; Biging, G.; Kelly, M.; Schirokauer, D. (2006). Object-based Detailed Vegetation Classification with Airborne High Spatial Resolution Remote Sensing Imagery. Photogramm. Eng. Remote Sens. 2006, 7, 799–811.

Xue, R., Yang, Q., Miao, F., Wang, X., & Shen, Y. (2018). Slope aspect influences plant biomass, soil properties and microbial composition in alpine meadow on the Qinghai-Tibetan plateau. Journal of soil science and plant nutrition, 18(1), 1-12.

Zevenbergen, L. W., & Thorne, C. R. (1987). Quantitative analysis of land surface topography. Earth surface processes and landforms, 12(1), 47-56.

Zhan, Q.; Molenaar, M.; Tempfli, K.; Shi, W. (2005). Quality assessment for geo-spatial objects derived from remotely sensed data. Int. J. Remote Sens. 2005, 26, 2953–2974.

Zhang, Y., Aradottir, A. L., Serpe, M., & Boeken, B. (2016). Interactions of biological soil crusts with vascular plants. In Biological soil crusts: an organizing principle in drylands (pp. 385-406). Springer, Cham.

Zhang, X.; Friedl, M.A.; Schaaf, C.B.; Strahler, A.H.; Hodges, J.C.; Gao, F.; Reed, B.C.; Huete, A. (2003). Monitoring vegetation phenology using MODIS. Remote Sens. Environ. 2003, 84, 471–475.

Zheng, X.; Wu, B.; Weston, M.; Zhang, J.; Gan, M.; Zhu, J.; Deng, J.; Wang, K.; Teng, L. (2017). Rural settlement subdivision by using landscape metrics as spatial contextual information. Remote Sens. 2017, 9, 486.

Zhou, X., Ke, T., Li, S., Deng, S., An, X., Ma, X., de Philippis, R. & Chen, L. (2020). Induced biological soil crusts and soil properties varied between slope aspect, slope gradient and plant canopy in the Hobq desert of China. Catena, 190(March), 104559.

Zink, M., Moreira, A., Bachmann, M., Rizzoli, P., Fritz, T., Hajnsek I., Krieger, G & Wessel, B. (2017) The global TanDEM-X DEM, a unique data set. In: IGARSS 2017, Fort Worth, TX, pp. 906–909. USA: IEEE.